NAVAL POSTGRADUATE SCHOOL

MONTEREY, CALIFORNIA

THESIS

USING MULTI-ANGLE WORLDVIEW-2 IMAGERY TO DETERMINE OCEAN DEPTH NEAR OAHU, HAWAII

by

Krista R. Lee

September 2012

Thesis Advisor:	Richard C. Olsen
Second Reader:	Fred A. Kruse

Approved for public release; distribution is unlimited

THIS PAGE INTENTIONALLY LEFT BLANK

REPORT DOCUMENTATION PAGE			Form Approved OMB No. 0704-0188
Public reporting burden for this collection of information is estimated to average 1 hour per response, including the time for reviewing instruction, searching existing data sources, gathering and maintaining the data needed, and completing and reviewing the collection of information. Send comments regarding this burden estimate or any other aspect of this collection of information, including suggestions for reducing this burden, to Washington headquarters Services, Directorate for Information Operations and Reports, 1215 Jefferson Davis Highway, Suite 1204, Arlington, VA 22202-4302, and to the Office of Management and Budget, Paperwork Reduction Project (0704-0188) Washington DC 20503.			
1. AGENCY USE ONLY ***(Leave blank)***	**2. REPORT DATE** September 2012	**3. REPORT TYPE AND DATES COVERED** Master's Thesis	
4. TITLE AND SUBTITLE Using Multi-Angle WorldView-2 Imagery to Determine Ocean Depth Near Oahu, Hawaii		**5. FUNDING NUMBERS**	
6. AUTHOR(S) Krista R. Lee			
7. PERFORMING ORGANIZATION NAME(S) AND ADDRESS(ES) Naval Postgraduate School Monterey, CA 93943-5000		**8. PERFORMING ORGANIZATION REPORT NUMBER**	
9. SPONSORING /MONITORING AGENCY NAME(S) AND ADDRESS(ES) N/A		**10. SPONSORING/MONITORING AGENCY REPORT NUMBER**	
11. SUPPLEMENTARY NOTES The views expressed in this thesis are those of the author and do not reflect the official policy or position of the Department of Defense or the U.S. Government. IRB Protocol number _____N/A_____.			
12a. DISTRIBUTION / AVAILABILITY STATEMENT Approved for public release; distribution is unlimited		**12b. DISTRIBUTION CODE** A	

13. ABSTRACT (maximum 200 words)

Multispectral imaging (MSI) data collected at multiple angles over shallow water provide analysts with a unique perspective of bathymetry in coastal areas. Observations taken by DigitalGlobe's WorldView-2 (WV-2) sensor acquired at 39 different view angles on 30 July 2011 were used to determine the effect of acquisition angle on derived depth. The site used for this study was on the island of Oahu, focused on Kailua Bay (on the windward side of the island). Satellite azimuth and elevation for these data ranged from 18.8 to 185.8 degrees and 24.9 (forward-looking) to 24.5 (backward-looking) degrees (respectively) with 90 degrees representing a nadir view. Bathymetry were derived directly from the WV-2 radiance data using a band ratio approach. Comparison of results to LiDAR-derived bathymetry showed that varying view angle impact the quality of the inferred bathymetry. Derived and reference bathymetry have a higher correlation as images are acquired closer to nadir. The band combination utilized for depth derivation also has an effect on derived bathymetry. Four band combinations were compared, and the Blue & Green combination provided the best results.

14. SUBJECT TERMS WorldView-2, Multispectral Imagery, Shallow Water Bathymetry, Depth Determination, Multi-Angle Remote Sensing			**15. NUMBER OF PAGES** 117
			16. PRICE CODE
17. SECURITY CLASSIFICATION OF REPORT Unclassified	**18. SECURITY CLASSIFICATION OF THIS PAGE** Unclassified	**19. SECURITY CLASSIFICATION OF ABSTRACT** Unclassified	**20. LIMITATION OF ABSTRACT** UU

NSN 7540-01-280-5500 Standard Form 298 (Rev. 2-89)
Prescribed by ANSI Std. 239-18

THIS PAGE INTENTIONALLY LEFT BLANK

Approved for public release; distribution is unlimited

USING MULTI-ANGLE WORLDVIEW-2 IMAGERY TO DETERMINE OCEAN DEPTH NEAR OAHU, HAWAII

Krista R. Lee
Civilian, United States Navy
B.A., University of California, Santa Barbara, 2008

Submitted in partial fulfillment of the
requirements for the degree of

MASTER OF SCIENCE IN REMOTE SENSING INTELLIGENCE

from the

NAVAL POSTGRADUATE SCHOOL
September 2012

Author: Krista R. Lee

Approved by: Dr. Richard C. Olsen
Thesis Advisor

Dr. Fred A. Kruse
Second Reader

Dr. Dan C. Boger
Chair, Department of Information Sciences

THIS PAGE INTENTIONALLY LEFT BLANK

ABSTRACT

Multispectral imaging (MSI) data collected at multiple angles over shallow water provide analysts with a unique perspective of bathymetry in coastal areas. Observations taken by DigitalGlobe's WorldView-2 (WV-2) sensor acquired at 39 different view angles on 30 July 2011 were used to determine the effect of acquisition angle on derived depth. The site used for this study was on the island of Oahu, focused on Kailua Bay (on the windward side of the island). Satellite azimuth and elevation for these data ranged from 18.8 to 185.8 degrees and 24.9 (forward-looking) to 24.5 (backward-looking) degrees (respectively) with 90 degrees representing a nadir view. Bathymetry were derived directly from the WV-2 radiance data using a band ratio approach. Comparison of results to LiDAR-derived bathymetry showed that varying view angle impact the quality of the inferred bathymetry. Derived and reference bathymetry have a higher correlation as images are acquired closer to nadir. The band combination utilized for depth derivation also has an effect on derived bathymetry. Four band combinations were compared, and the Blue & Green combination provided the best results.

THIS PAGE INTENTIONALLY LEFT BLANK

TABLE OF CONTENTS

I. INTRODUCTION....1
A. PURPOSE OF RESEARCH....1
B. SPECIFIC OBJECTIVES....2

II. BACKGROUND....3
A. PRINCIPLES OF RADIATIVE TRANSFER....3
1. Electromagnetic Spectrum....3
2. Spectral Signatures....4
3. The Four Fundamental Energy Interactions with Matter....6
a. Transmission....6
b. Reflection....7
c. Scattering....8
d. Absorption....9
B. INTERACTIONS OF LIGHT WITH THE ATMOSPHERE....10
1. Atmospheric Absorption....10
2. Atmospheric Scattering....11
3. Atmospheric Compensation for Spectral Imagery....12
C. INTERACTIONS OF LIGHT AND WATER....13
1. Inherent Optical Properties (IOPs)....13
2. Apparent Optical Properties (AOPs)....14
3. Sun Glint Correction for Spectral Imagery....14
D. MULTI-ANGLE RESEARCH....17
E. PREVIOUS WORK AT THE NAVAL POSTGRADUATE SCHOOL....19
1. Work in Satellite Derived Bathymetry....19
a. Depth Analysis of Midway Atoll Using QuickBird Multi-Spectral Imaging over Variable Substrates (Camacho, 2006)....19
b. Depth Derivation from the WorldView-2 Satellite Using Hyperspectral Imagery (Loomis, 2009)....19
c. Contributions to Remote Sensing of Shallow Water Depth with the WorldView-2 Yellow Band (Madden, 2011)....20
2. Work in Multi-Observation Imagery....20
a. Coastal Bathymetry Using 8-Color Multispectral Satellite Observation of Wave Motion (McCarthy, 2010)....20
b. Coastal Bathymetry Using Satellite Observation in Support of Intelligence Preparations of the Environment (Myrick, 2011)....20
c. Automating Nearshore Bathymetry Extraction from Wave Motion in Satellite Optical Imagery (Mancini, 2012)....21
d. High Spatial Resolution Bidirectional Reflectance Retrieval Using Satellite Data (McConnon, 2010)....21

III. DATA AND METHODS....23

A. DATA 23
1. Satellite Sensor, Study Site, and Imagery Dataset 23
a. WorldView-2 (WV-2) 23
b. Kailua Bay, Oahu, Hawaii 26
c. Imagery Dataset 28
2. Bathymetry Data 28
3. Software 29
a. Environment for Visualizing Images + Interactive Data Language 4.8 (ENVI 4.8 + IDL) 29
B. METHODS 29
1. Bathymetry Derivation 30
a. Assess Data Coverage, Angles, and Quality 30
b. Mosaic Data 33
c. Convert Map Projection 33
d. Radiance Calibration 34
e. Subset Data 35
f. Registration of Off-Nadir Images to the Most Nadir Image 35
g. Land, Glint, Cloud, and Whitecap Masks 36
h. Glint Removal 38
i. Band Ratio to Determine Relative Bathymetry 40
j. Comparison of Water Depths to LiDAR Bathymetry 41
k. Derived Bathymetry 41
2. Analyze Effects of Collection Geometry on Water Depth Derivation 41

IV. RESULTS 43
A. BATHYMETRY FROM ENTIRE IMAGE 43
B. VARIATION IN ACQUISITION ANGLES 47

V. CONCLUSIONS 57
A. SUMMARY OF OBSERVATIONS AND ANALYSIS 57
B. RECOMMENDATIONS AND FUTURE WORK 57

LIST OF REFERENCES 59

APPENDIX: CHARTS AND GRAPHS 63
A. EXAMPLE WORLDVIEW-2 METADATA FILE (FOR IMAGE 1010) 63
B. INFORMATION ABOUT THE 39 WORLDVIEW-2 IMAGES – IMAGE ID, ACQUISITION TIME, SENSOR ELEVATION, SENSOR AZIMUTH, OFF NADIR VIEW ANGLE, AZIMUTH, AND ZENITH 68
C. IDL CODE FOR MOST HIGHLY CORRELATED BAND COMBINATION (BLUE & GREEN) 73
D. DERIVED DEPTH VS. TRUE DEPTH PLOTS AND LINES OF BEST FIT 85

E. TABLES OF EXAMPLE CHI-SQUARED AND CORRELATION VALUES FOR EACH BAND COMBINATION 89
1. Coastal & Blue (with best fits highlighted) 89
2. Coastal & Green (with best fits highlighted) 90
3. Blue & Green (with best fits highlighted) 91
4. Green & Yellow (with best fits highlighted) 92

INITIAL DISTRIBUTION LIST 95

THIS PAGE INTENTIONALLY LEFT BLANK

LIST OF FIGURES

Figure 1. The Electromagnetic Spectrum (From *Jensen* [2007]) 4

Figure 2. Hyperspectral Imagery (HSI) provides more complete spectral signatures than MSI because there are a much larger number of bands. Albedo values for different forms of algae and coral are shown (From *Maritorena et al.* [1994]; *Camacho* [2006]) 5

Figure 3. MSI has spectral signatures that look less complete compared to HSI because there are fewer bands (spectra are taken from a scene used in this research and are in nanometers) 6

Figure 4. Transmission (After *Avery and Berlin* [1992]) 7

Figure 5. Reflection (After *Avery and Berlin* [1992]) 8

Figure 6. Scattering (After *Avery and Berlin* [1992]) 8

Figure 7. Reflection geometry used in the definition of BRDF (From *McConnon* [2010]) 9

Figure 8. Absorption (After *Avery and Berlin* [1992]) 10

Figure 9. The first four graphs show the absorption characteristics of N_2O, O_2 and O_3, CO_2, and H_2O, while the bottom graphic depicts the cumulative result of all these constituents being in the atmosphere at one time (From *Jensen* [2007]) 11

Figure 10. Diagram showing routes by which light can reach a remote sensing detector (From *Kay et al.* [2009]) 12

Figure 11. An example of sun glint on the ocean's surface (image captured by the Geostationary Operational Environmental Satellite (GOES) on 2 December 2009) (From http://rsd.gsfc.nasa.gov/goes/text/hotstuff.html) 15

Figure 12. Another example demonstrating the effect of sun glint on the imager (image captured by the GOES satellite on 22 June 2000) (From http://rsd.gsfc.nasa.gov/goes/text/hotstuff.html) 15

Figure 13. Ground observed azimuth and elevation of the WV-2 satellite (black markers) for each image observation as well as the azimuth and elevation of the sun (yellow circle) during the 2009 Atlanta, GA multi-angle sequence acquisition. Azimuth is plotted angularly clockwise (North: 0 degrees, East: 90 degrees, South: 180 degrees, West: 270 degrees), and elevation is plotted radially from the center (ground nadir: 90 degrees, ground horizon: 0 degrees) (From *Longbotham, Chaapel et al.* [2011]) 18

Figure 14. WV-2's relative spectral radiance response (From *Updike and Comp* [2010]) 25

Figure 15. The Hawaiian Islands (left), focusing on Kailua Bay, Oahu (right) (From Google Earth) 27

Figure 16. Oblique aerial imagery acquired over Kailua Bay on 10 November 2003 on a Nikon Coolpix 5700 digital camera (settings and focus all automated) from a Cessna plane flying at about 2,000 feet (From http://www.soest.hawaii.edu/coasts/erosion/oahu/oblique.php) 27

Figure 17. Five examples out of the 39 WV-2 image acquisitions (labels are actual Image IDs) 28
Figure 18. The most forward-looking, nadir, and backward-looking images after data coverage assessment and mosaicking 33
Figure 19. Map projection conversion from Geographic Latitude/Longitude (left) to UTM, WGS-84, Zone 4N (right) 34
Figure 20. The full scene (left) was chipped to focus on Kailua Bay (right) 35
Figure 21. After registration, each image (top) was chipped to the 995 x 999 pixel scene shown (bottom) 36
Figure 22. The original image (left) has a corresponding scatter plot (middle); specific sections of the plot are highlighted to show how they correspond to the image (right)—red is mostly land, green is mostly whitecaps and sun glint, and blue is water 36
Figure 23. 2D scatter plot of the Blue vs. NIR-1 bands; the user-defined outline region includes pixels containing water, and everything else can generally be classified as land, clouds, glint, whitecaps, etc. (e.g., not water) 37
Figure 24. Land, glint, clouds, and whitecaps have been masked in this image 38
Figure 25. Graphical interpretation of the *Hedley et al.* [2005] de-glinting method (From *Hedley et al.* [2005]) 39
Figure 26. "True" bathymetry data; depth is represented by the Rainbow scale (shallow water is red and deep water is black) 44
Figure 27. Derived depths for each band combination for Image 1010 (most forward-looking) 45
Figure 28. Derived depths for each band combination for Image 2010 45
Figure 29. Derived depths for each band combination for Image 2100 (most nadir) 45
Figure 30. Derived depths for each band combination for Image 3100 46
Figure 31. Derived depths for each band combination for Image 4100 (most backward-looking) 46
Figure 32. Coastal & Blue: Derived depth vs. "true" depth for Image 2100 (most nadir) 47
Figure 33. Coastal & Green: Derived depth vs. "true" depth for Image 2100 (most nadir) 48
Figure 34. Blue & Green: Derived depth vs. "true" depth for Image 2100 (most nadir) 49
Figure 35. Green & Yellow: Derived depth vs. "true" depth for Image 2100 (most nadir) 50
Figure 36. Coastal & Blue: Chi-squared (top) and correlation (bottom) values (y-axis) plotted against the mean satellite elevation angle (x-axis) for all 39 WV-2 images 51
Figure 37. Coastal & Green: Chi-squared (top) and correlation (bottom) values (y-axis) plotted against the mean satellite elevation angle (x-axis) for all 39 WV-2 images 52
Figure 38. Blue & Green: Chi-squared (top) and correlation (bottom) values (y-axis) plotted against the mean satellite elevation angle (x-axis) for all 39 WV-2 images 53

Figure 39. Green & Yellow: Chi-squared (top) and correlation (bottom) values (y-axis) plotted against the mean satellite elevation angle (x-axis) for all 39 WV-2 images 54

THIS PAGE INTENTIONALLY LEFT BLANK

LIST OF TABLES

Table 1. WV-2 Design and Specifications (After information available at http://www.digitalglobe.com/about-us/content-collection#satellites&worldview-2) 24
Table 2. WV-2 Sensor Bands (After information available at http://www.digitalglobe.com/about-us/content-collection#satellites&worldview-2) 25
Table 3. List of WorldView-2 Images 31

THIS PAGE INTENTIONALLY LEFT BLANK

LIST OF ACRONYMS AND ABBREVIATIONS

AOPs: Apparent Optical Properties

AVIRIS: Airborne Visible/InfraRed Imaging Spectrometer

BRDF: Bidirectional Reflectance Distribution Function

DHMs: Digital Height Maps

DNs: Digital Numbers

EM: Electromagnetic

ENVI: Environment for Visualizing Images

GOES: Geostationary Operational Environmental Satellite

HSI: Hyperspectral Imagery

IDL: Interactive Data Language

IOPs: Inherent Optical Properties

IR: Infrared

LiDAR: Light Detection And Ranging

MS: Multispectral

MSI: Multispectral Imagery/Imaging

NIR: Near Infrared

RMS: Root Mean Square

ROIs: Regions of Interest

SHOALS: Scanning Hydrographic Operational Airborne Lidar Survey

SONAR: SOund Detection And Ranging

SWIR: Shortwave Infrared

USGS: United States Geological Survey

UTM: Universal Transverse Mercator

UV: Ultraviolet

VIS: Visible

WGS-84: World Geodetic System 1984

WKB: Wave Kinematics Bathymetry

WV-2: WorldView-2

ACKNOWLEDGMENTS

Many thanks to the staff and faculty of the Remote Sensing Center at the Naval Postgraduate School. Every member played a part in the completion of my thesis to include both intellectual and moral support.

Thank you to Dr. Giovanni Marchisio, Dr. Fabio Pacifici, and Dr. Nathan Longbotham of DigitalGlobe, Inc. for their help with all of my questions related to the capabilities of the sensor used in this research.

I would like to thank three people in particular, all of whom made the thesis writing process easier and more enjoyable. Thank you to Angie Kim, for her help with the coding (these results would not be possible without her programming expertise). Thank you to Dr. Fred Kruse, who encouraged me to question my results and see if I couldn't push my work just a little further in order to obtain something better or more interesting. Finally, thank you to Professor Chris Olsen. He was not only a wonderful thesis advisor, but also an amazing employer who pushed me beyond my researching comfort zone, of which I am so thankful!

And, of course, I absolutely have to thank my family, fiancé, and friends for all of their love and support throughout this process.

THIS PAGE INTENTIONALLY LEFT BLANK

I. INTRODUCTION

A. PURPOSE OF RESEARCH

Imagery data acquired from satellites are widely useful in the field of oceanography. These data contribute to a better understanding of the dynamics of ocean circulation, are useful for monitoring climate change, can be used for navigation and fisheries management, and are also helpful for improving models of ocean circulation, air-sea interaction, weather forecasting, and climate [*Sanford et al.*, 2011].

Information about shallow water bathymetry is beneficial to scientists or groups that require knowledge of ocean depths in a particular coastal location. The use of multispectral imagery (MSI) data has been shown to adequately determine depths of remote coastal areas, as SOund Navigation And Ranging (SONAR) or Light Detection And Ranging (LiDAR) soundings or other bathymetric data may not be available prior to arrival.

There are many benefits to using remote sensing data acquired from satellites. Spaceborne sensors can collect spectral data over extremely large areas which can be advantageous to regions not accessible on foot, or for areas denied by hostile forces. These data can also be acquired much more rapidly due to the number of space platforms collecting on a regular basis. Finally, improvements in collection capabilities steadily grow as space platform production increases and sensor technologies evolve. This capability is extremely valuable to the Navy and Marine Corps, who routinely conduct and plan worldwide amphibious operations. Coastlines are highly dynamic environments and mission success is dependent upon knowing the underwater terrain. Being able to acquire bathymetry in a contested or denied region greatly improves the probability of success for these amphibious operations.

The purpose of this research was to integrate the use of multiple satellite image acquisition angles over one location, and determine what role these varying angles play in bathymetric depth determination. Analyses of 39 WorldView-2 (WV-2) images acquired

over Kailua Bay on the windward side of Oahu, Hawaii were used to reach a conclusion about the accuracy of bathymetric derivation from MSI.

B. SPECIFIC OBJECTIVES

The objective of this study was to test the potential of bathymetric derivation using WV-2 imagery acquired at multiple angles, and then report upon the role that image acquisition angle plays in depth determination.

The motivation for this work originated from the need to determine bathymetry from only a single spectral image of the coastal region in question. There is no guarantee that this image will have been acquired at optimal viewing geometry, e.g., nadir. Without sufficient time to task a satellite and acquire data at a particular viewing angle before a site visit, results from this research strive to provide a better understanding of how to manipulate image data in order to obtain a better understanding of bathymetry. Analysis of multi-angle MSI data was used to quantify the effects of varying satellite acquisition angle on accurate determination of bathymetry.

II. BACKGROUND

This research focused on the use of passive, optical remote sensing systems for image acquisition. Passive sensors are those that rely on incoming solar radiation to illuminate the targets on land and in the water [*Camacho*, 2006]. Optical sensors are those that focus on the visible (VIS), near infrared (NIR), and shortwave infrared (SWIR) portions of the electromagnetic (EM) spectrum to observe radiation from targets [*Camacho*, 2006]. The following sections will explain these principles in more detail, as well as further discuss some issues that affect remote sensing of ocean environments, as well as imagery acquired at multiple angles.

A. PRINCIPLES OF RADIATIVE TRANSFER

A remote sensing instrument or sensor receives energy that is reflected from the surface of the Earth. This energy is affected by interactions of light with the atmosphere and water, as well as any particulate matter in the water column [*Camacho*, 2006]. It is imperative to understand the basics about the EM spectrum, radiation, the variety of possible interactions, and line spectra.

1. Electromagnetic Spectrum

The EM spectrum is a conglomeration of a number of classifiable spectral regions. These include: gamma rays, X-rays, ultraviolet (UV) light, VIS light, IR light, microwaves, and radio waves (Figure 1) [*Olsen*, 2007].

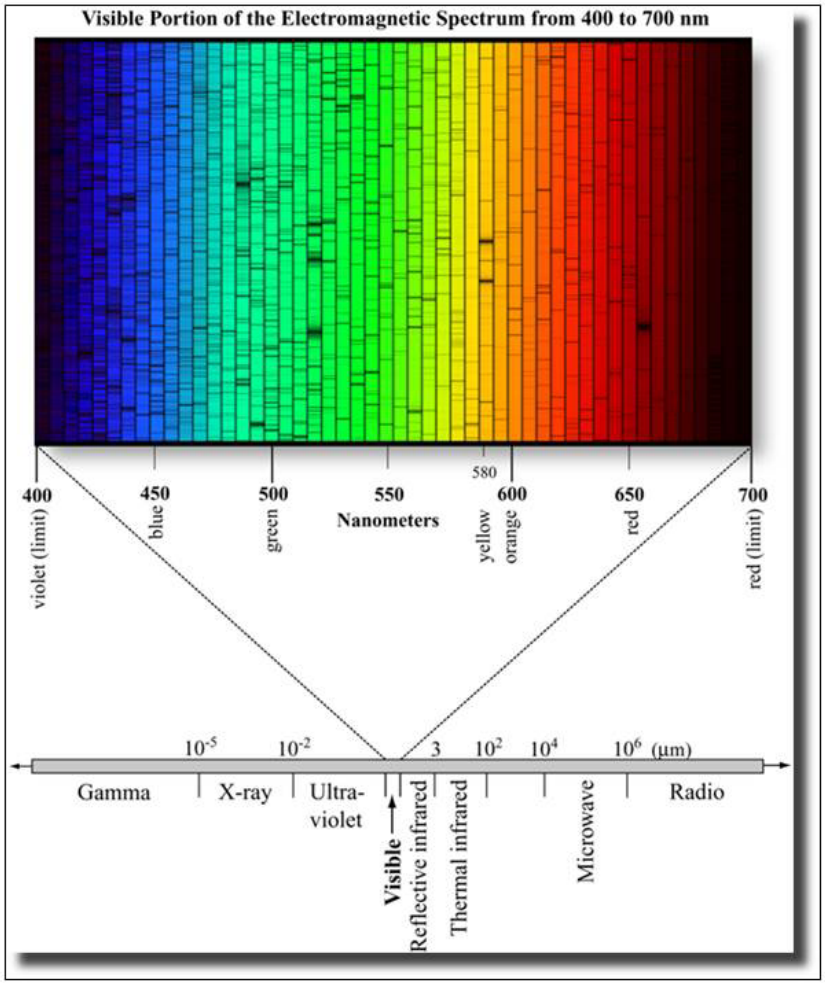

Figure 1. The Electromagnetic Spectrum (From *Jensen* [2007])

This research focuses on the VIS and NIR portions of the spectrum, extending from approximately 400 nm to 750 nm, and 750 nm to 1000 nm (respectively).

2. Spectral Signatures

Single atoms or molecules emit light in the form of line spectra, and an atom that is well isolated will radiate a discrete set of frequencies called a line spectrum. The wavelengths radiated and absorbed are specific to that atom or molecule, and are presented as spectral signatures. These signatures are used to determine the composition of radiating or absorbing gases and other materials [*Olsen*, 2007].

Spectral features, such as those shown in Figures 2 and 3, enable analysts to better differentiate between materials on the ground. Based on specific values, peaks, and troughs within the graph, one can determine the basic makeup of a material within the image.

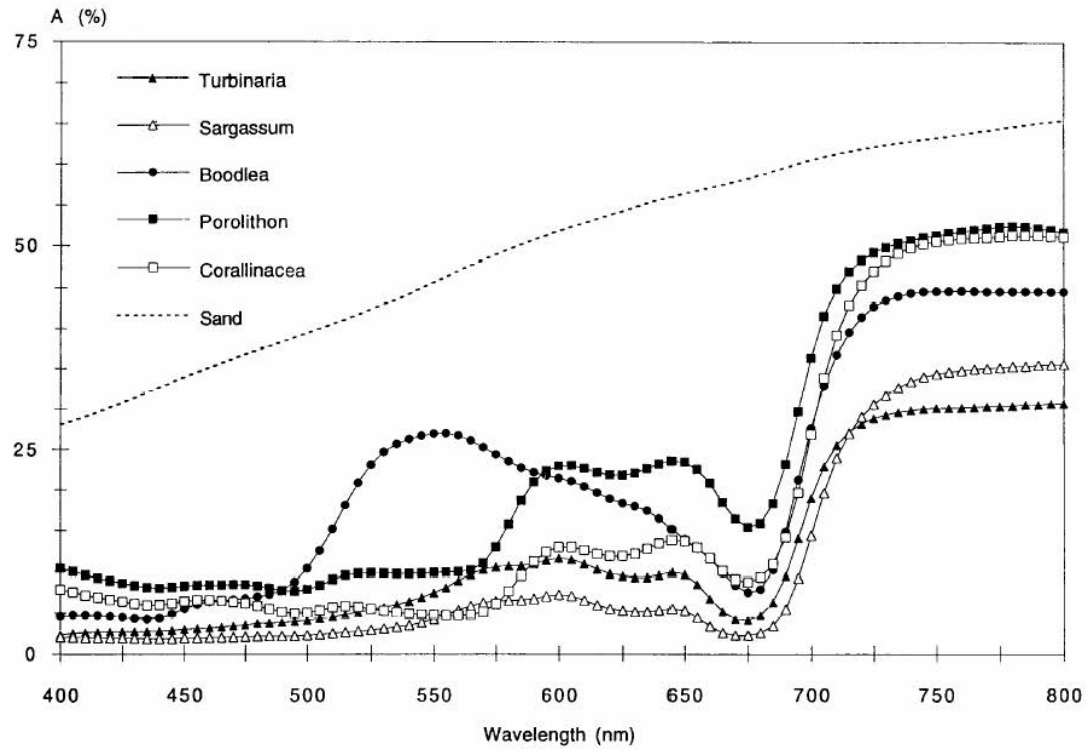

Figure 2. Hyperspectral Imagery (HSI) provides more complete spectral signatures than MSI because there are a much larger number of bands. Albedo values for different forms of algae and coral are shown (From *Maritorena et al.* [1994]; *Camacho* [2006])

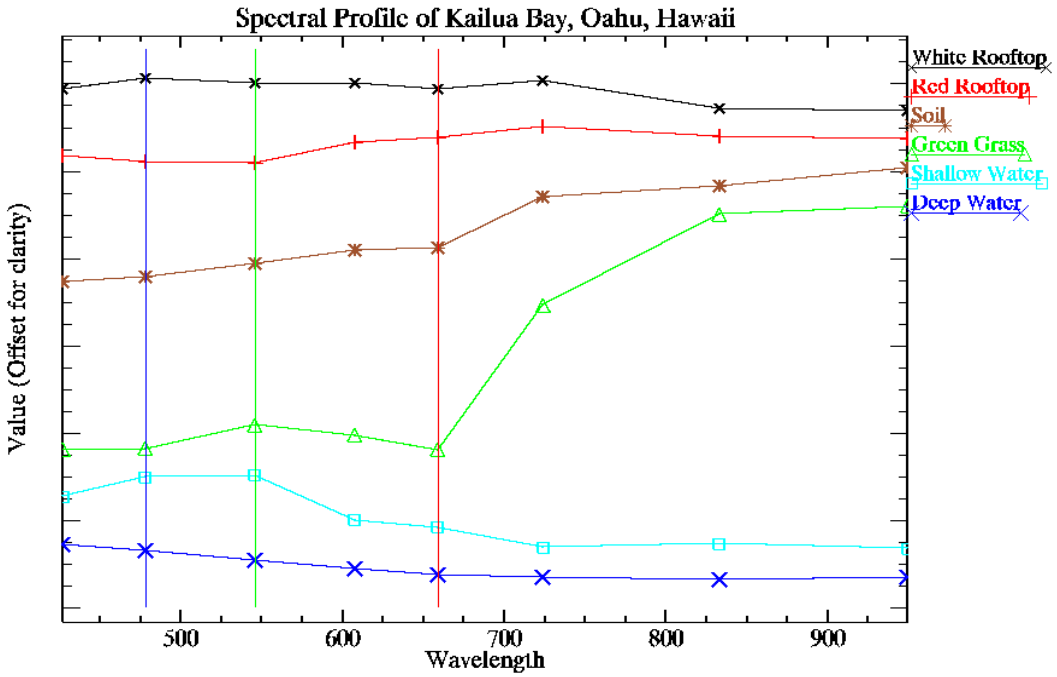

Figure 3. MSI has spectral signatures that look less complete compared to HSI because there are fewer bands (spectra are taken from a scene used in this research and are in nanometers)

3. The Four Fundamental Energy Interactions with Matter

Electromagnetic radiation may be transmitted, reflected, scattered, or absorbed. The proportions to which these interactions occur depend on the compositional and physical properties of the medium, the wavelength or frequency of the incident radiation, and the angle at which the incident radiation strikes a surface [*Avery and Berlin*, 1992; *Olsen*, 2007].

a. Transmission

With transmission, shown in Figure 4, incident radiation passes through matter without measurable attenuation. Different densities of the material, however, can cause radiation to be refracted or deflected from a straight-line path, and will also alter the velocity and wavelength. The change in EM radiation velocity can be further

explained by the index of refraction, which is the ratio between the velocity of the EM radiation in a vacuum (a perfectly transparent medium) and its velocity in a material medium.

The index of refraction for a vacuum is equal to 1, and can never be less than 1 for any substance [*Avery and Berlin*, 1992].

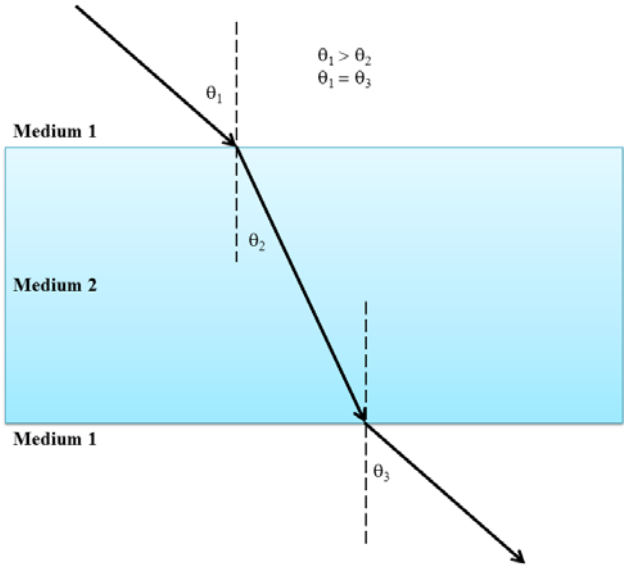

Figure 4. Transmission (After *Avery and Berlin* [1992])

b. Reflection

Reflection, or specular reflection, occurs when surfaces are smooth relative to the wavelengths of incident radiation (Figure 5). Specular reflection, the process by which incident radiation bounces off the surface of a substance in a single and predictable direction, causes no change to either the EM radiation velocity or wavelength [*Avery and Berlin*, 1992].

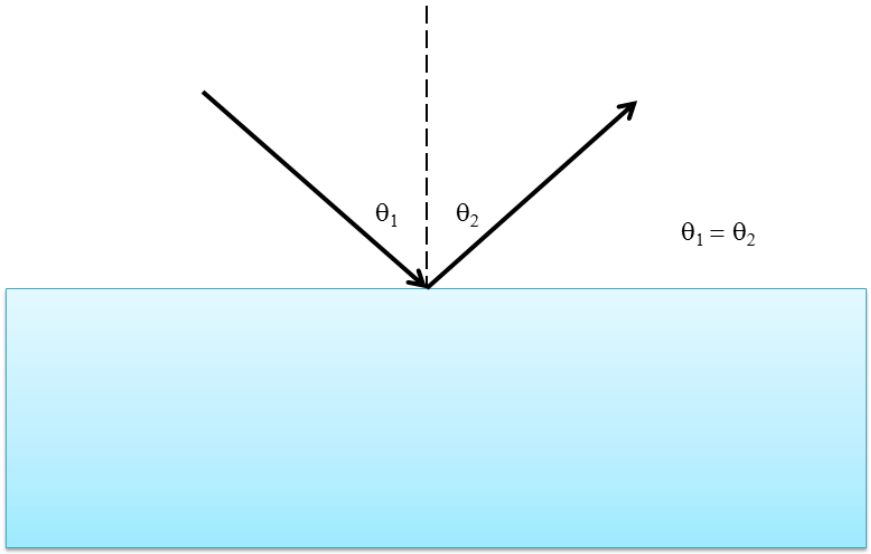

Figure 5. Reflection (After *Avery and Berlin* [1992])

c. Scattering

Scattering, or diffuse reflection, takes place when incident radiation is dispersed in unpredictable directions. Scattering occurs when surfaces are rougher relative to the wavelengths of incident radiation, as shown in Figure 6. The velocity and wavelength of EM waves, however, are not affected by scattering [*Avery and Berlin*, 1992].

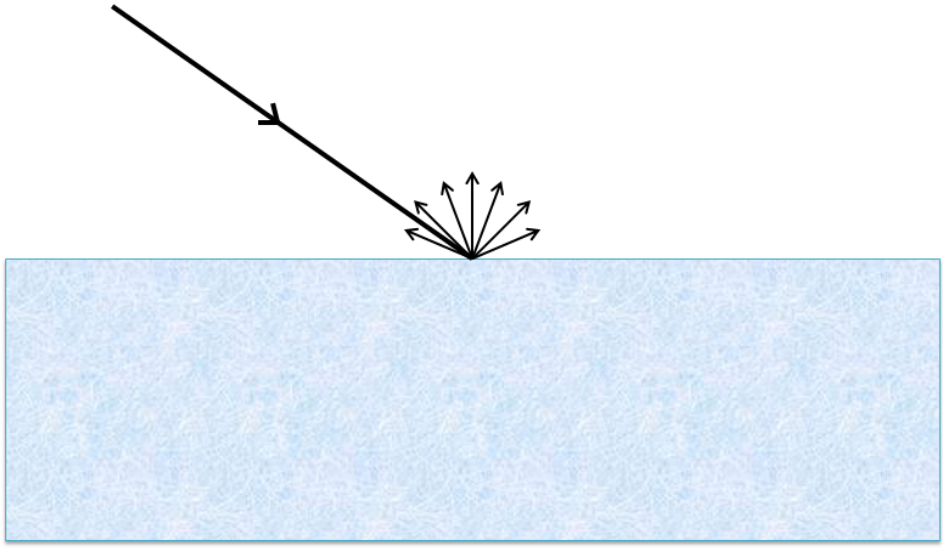

Figure 6. Scattering (After *Avery and Berlin* [1992])

(1) Bidirectional Reflectance Distribution Function (BRDF). The Bidirectional Reflectance Distribution Function (BRDF) describes the scattering characteristics of a material by describing how light from a source, incident on a target, is reflected in a given direction. In order to calculate BRDF, one looks at the ratio of the energy scattered by the target in a particular direction, dependent on wavelength, over the energy that was incident on the target from a particular direction. All combinations of inbound and outbound energy directions are then integrated. BRDF is dependent on both the angle of incidence and on the angle of reflectance. Angles are defined in a Cartesian coordinate system by a polar angle, θ, measured from the surface normal, as well as an azimuthal angle, φ, measured from the x-axis (Figure 7) [*McConnon*, 2010].

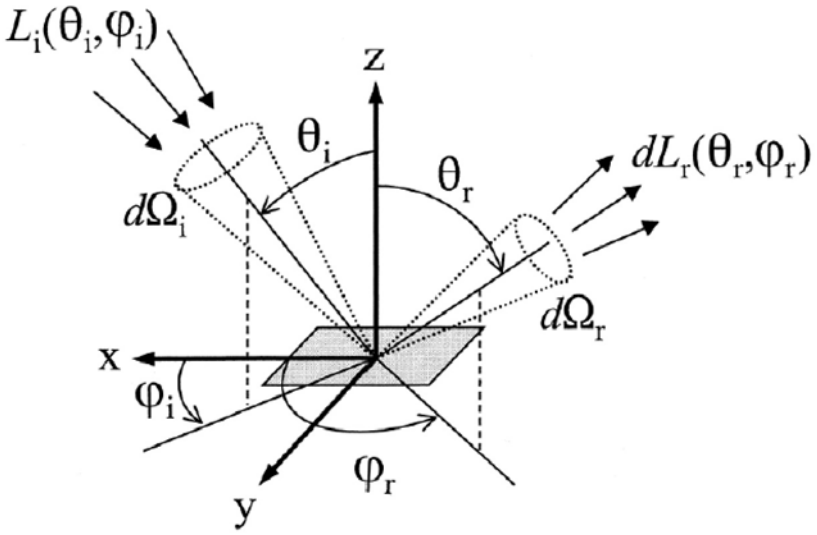

Figure 7. Reflection geometry used in the definition of BRDF (From *McConnon* [2010])

d. Absorption

Absorption is the process by which incident radiation is taken in by a medium. This occurs when a substance is opaque to the incident radiation, a portion of which is converted to internal heat energy, then emitted or reradiated at longer thermal infrared wavelengths (Figure 8) [*Avery and Berlin*, 1992].

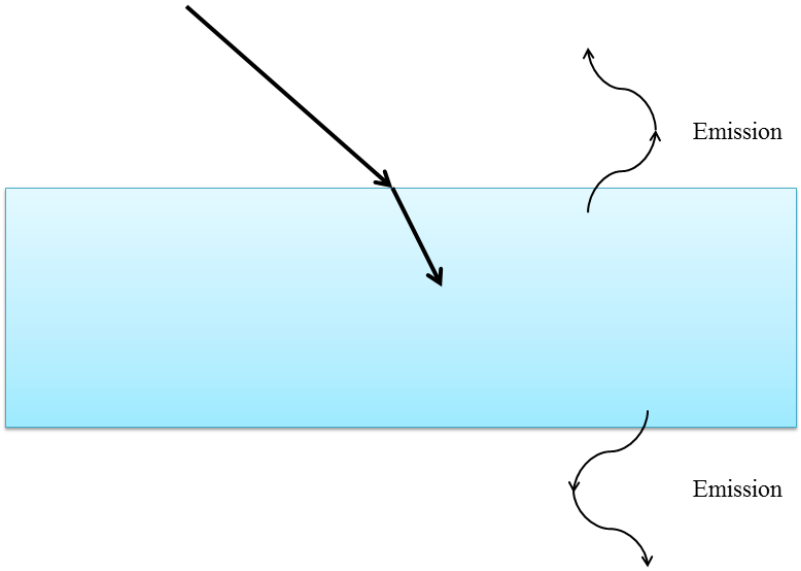

Figure 8. Absorption (After *Avery and Berlin* [1992])

B. INTERACTIONS OF LIGHT WITH THE ATMOSPHERE

There are three limiting factors that the atmosphere introduces into the field of remote sensing. These include atmospheric absorption, scattering, and turbulence [*Olsen*, 2007]. Atmospheric turbulence, however, will not be discussed here because its impact is greater for telescopes looking up from the earth through the atmosphere than for sensors looking down. Also, it is important to keep in mind that, overall, the atmosphere is more transparent in the long-wave IR (1100 to 1200 nm) than in the VIS spectrum (400 to 750 nm) [*Olsen*, 2007].

1. Atmospheric Absorption

Atmospheric absorption is mainly dependent on wavelength, and is most affected by water (between 500 and 700 nm), carbon dioxide, and ozone (near 1000 nm) [*Olsen*, 2007]. Even after sensor calibration has occurred, the shape of the measured spectra relative to the underlying reflectance spectra are altered because of atmospheric absorption lines [*Eismann*, 2012]. Common absorption spectra can be seen in Figure 9.

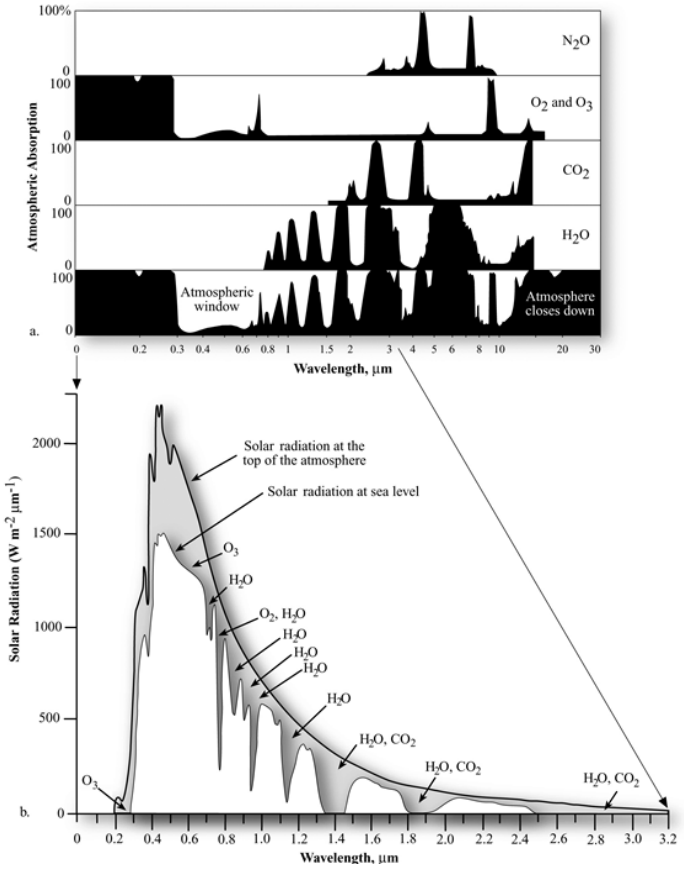

Figure 9. The first four graphs show the absorption characteristics of N_2O, O_2 and O_3, CO_2, and H_2O, while the bottom graphic depicts the cumulative result of all these constituents being in the atmosphere at one time (From *Jensen* [2007])

2. Atmospheric Scattering

Atmospheric scattering is primarily caused by collisions between aerosols and particulates like dust, fog, and smoke in the atmosphere [*Olsen*, 2007]. There are two main consequences of atmospheric scattering: reduction of radiant energy and unwanted gain in the sensor [*Martin*, 2004; *Camacho*, 2006]. Scattering can also be divided into two types: Rayleigh and Mie scattering. Rayleigh, or molecular, scattering is primarily caused by oxygen and nitrogen molecules, i.e., particles whose effective diameters are less than the wavelengths of interest. As the size of the particle increases, the scattering processes move towards Mie scattering. This type of scattering occurs when the diameter of particles is similar to the wavelengths of the energy being radiated [*Camacho*, 2006; *Olsen*, 2007].

3. Atmospheric Compensation for Spectral Imagery

The effects the atmosphere has on incoming radiation reaching a remote sensing sensor results from a variety of processes. Five possibilities are shown in Figure 10 *[Kay et al.*, 2009].

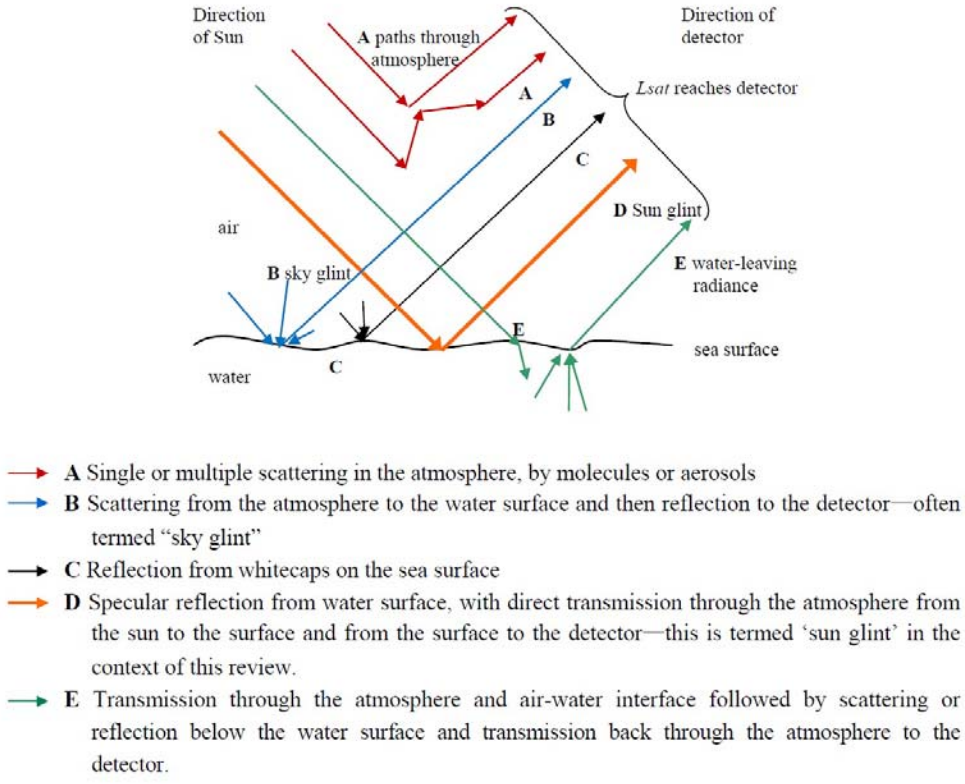

Figure 10. Diagram showing routes by which light can reach a remote sensing detector (From *Kay et al.* [2009])

Kay et al. [2009] assumes that if these five processes are predominantly responsible for the sensor-received signal, then:

$$L_{\text{sensor}} = L_{\text{atm}} + TL_{\text{sky}} + TL_{\text{whitecap}} + TL_{\text{glint}} + TL_{\text{water}} \quad (1)$$

where T is the transmittance of the atmosphere along the sensor view direction. The path L_{atm} is the radiance that arrives at the sensor via atmospheric paths (single or multiple scattering in the atmosphere, by molecules or aerosols). Other terms L_{sky}, L_{whitecap}, L_{glint}, and L_{water} are the radiances just above the water surface for light traveling by sky glint, whitecap, sun glint, and water-leaving routes. These terms depend on the wavelength,

along with other factors. The term L_{water} contains the information about water column and benthic features, and needs to be separated from the other terms if this information is going to be retrieved [*Kay et al.*, 2009].

C. INTERACTIONS OF LIGHT AND WATER

Optical oceanography is vital for addressing problems such as photosynthesis, ecosystem dynamics, ocean health, seawater clarity, underwater imaging, biogeochemical cycling, carbon budgets, upper-ocean thermodynamics, and climate change *[Dickey et al.*, 2011].

The simplest optical interactions occur at the boundary of the atmosphere and ocean, and are governed by Snell's law and the Fresnel equations. In order to accurately model the very complex interactions between water molecules and other constituents, radiative-transfer methods and precise measurements are required [*Dickey et al.*, 2011].

Optical remote sensing is an important tool utilized for monitoring marine environments. Since light is readily absorbed by water, remote sensing is most successful in places with very shallow, clear water, usually up to depths of 30 or possibly 40 meters. Sea water contains dissolved and particulate matter, with varying concentrations (both spatially and temporally) throughout the water column [*Mobley*, 1994; *Camacho*, 2006]. Optical properties of the water column can be divided into two classes—inherent optical properties (IOPs) and apparent optical properties (AOPs) [*Smith and Baker*, 1981; *Camacho*, 2006]. These classes are further discussed in sections to follow.

1. Inherent Optical Properties (IOPs)

An optical property is inherent if it depends only upon the medium and is independent of the ambient light field within that medium [*Mobley*, 1994; *Camacho*, 2006]. As light enters the water column, it interacts with particles and sediment, which cause the incident light to be altered by scattering or absorption [*Thomas and Stamnes*, 1999; *Camacho*, 2006]. It is these scattering and absorption characteristics that define IOPs of water [*Camacho*, 2006].

2. Apparent Optical Properties (AOPs)

An optical property is apparent if it is dependent on the medium, as well as the directional structure of the ambient light field. Similar to IOPs, AOPs are also dependent on the dissolved particles and sediment in the water column. Unlike IOPs, however, these properties cannot be measured *in situ* because they depend on the ambient radiance [*Mobley*, 1994; *Camacho*, 2006].

3. Sun Glint Correction for Spectral Imagery

Sun glint is the specular reflection of light directly transmitted from the upper side of the air-water interface [*Kay et al.*, 2009]. It typically forms bands of white along wave edges on the windward side of nearshore environments [*Hedley et al.*, 2005]. As it is a serious confounding factor for remote sensing of water column properties and benthos, researchers have spent a good deal of time creating and testing techniques to estimate and remove the glint radiance component from imagery. Sun glint, which is a function of sea surface state, sun position, and viewing angle, occurs in imagery when the water surface orientation is such that the sun is directly reflected toward the sensor. The component of sensor-received radiance can be so high that it becomes impossible to retrieve any information about the ocean environment [*Kay et al.*, 2009]. Examples of sun glint appearing in imagery are shown in Figures 11 and 12.

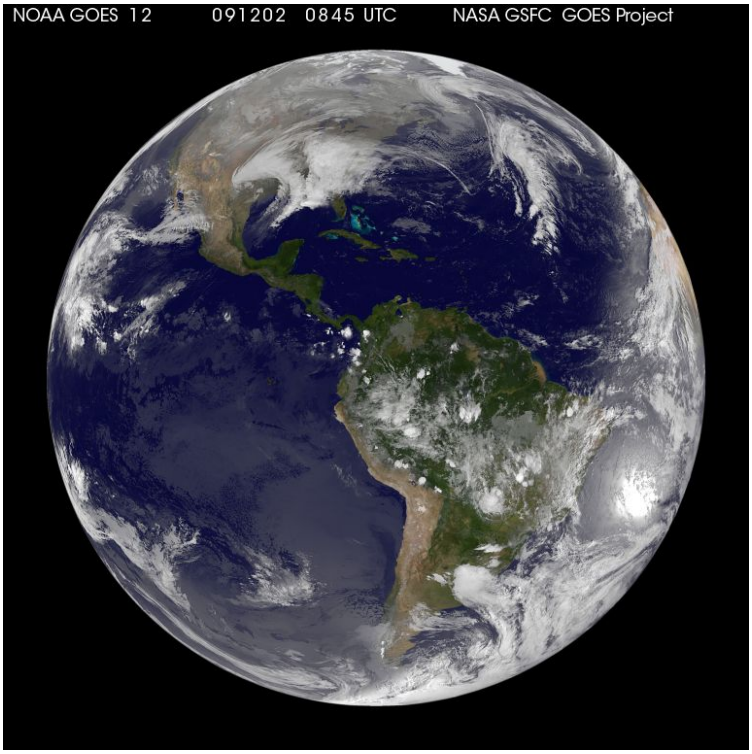

Figure 11. An example of sun glint on the ocean's surface (image captured by the Geostationary Operational Environmental Satellite (GOES) on 2 December 2009) (Image from http://rsd.gsfc.nasa.gov/goes/text/hotstuff.html)

Figure 12. Another example demonstrating the effect of sun glint on the imager (image captured by the GOES satellite on 22 June 2000) (Image from http://rsd.gsfc.nasa.gov/goes/text/hotstuff.html)

Sun glint causes problems within the imagery domain. A case study performed by *Goodman et al.* [2008] reported that uncorrected glint in high resolution imagery led to errors as large as 30% when measuring ocean depth. For airborne surveys, optimal flight paths and directions can be chosen based on the time of day, but this is more difficult in the case of satellite imagery [*Goodman et al.*, 2008].

Glint correction methods have been developed to improve image accuracy for two main categories of water types: open ocean imaging, and higher resolution coastal and aerial applications. The aim for both cases is the same—to estimate the glint contribution to the radiance reaching the sensor, and then subtract it from the received signal *[Kay et al.*, 2009].

The set of methods utilized for coastal images is meant to be used with pixel sizes of less than approximately 10 meters. Data from the NIR band are used as an indication of the amount of glint in the received signal. The spectrum from a section of the image containing deep water is then used to establish the relationship between the NIR and glint radiances [*Hochberg et al.*, 2003; *Hedley et al.*, 2005; *Lyzenga et al.*, 2006; *Goodman et al.*, 2008; *Kay et al.*, 2009]. The assumption of a linear relationship between NIR brightness and the amount of sun glint in the VIS bands holds because the real index of refraction is approximately equal for NIR and VIS wavelengths *[Mobley, 1994; Hedley et al.*, 2005].

When no sun glint is present, the radiance received by a satellite-borne sensor is dominated by atmospheric scattering. Light from paths through the air constitute over 80% of received radiance, water-leaving paths make up approximately 15%, and reflected light only 1 to 2% [*Sturm*, 1981; *Kay et al.*, 2009]. Sun glint can increase the reflected radiance by a factor of 2 or more, and the worst case glint can saturate the sensor, making it impossible to retrieve the water-leaving radiance for those pixels *[Kay et al.*, 2009].

D. MULTI-ANGLE RESEARCH

Multi-angle remote sensing capabilities offer a number of advantages with respect to a single shot dataset. Multi-angular data fusion has been shown to allow:

- The exploitation/investigation of BRDF,
- The extraction of digital height maps (DHMs),
- Atmospheric parameter retrieval,
- Classification improvement, etc. [*Pacifici et al.*, 2011]

The implications of adding height data and multi-angle MS reflectance, both derived from the multi-angle sequence, to the textural, morphological, and spectral information of a single MS image has been investigated by *Longbotham et al.* [2011]. It was determined that multi-angle collections significantly increase the dimensionality of the data available for a single target, as well as allow for differentiation of classes not typically well identified by a single image [*Longbotham, Chaapel et al.*, 2011].

For the particular *Longbotham et al.* [2011] study referred to here, the analyzed data sequence was collected over urban areas of Atlanta, GA in December 2009. The full dataset contained 27 images, with satellite elevation (the angle between the horizon and satellite as viewed from the image target) as low as 25 degrees, but the study only utilized those images with a moderate (relative to the satellite's capability) off-nadir observation angle of less than 30 degrees. This left the group with 13 images between 57 degrees (forward-looking) to 81.5 degrees (most nadir) to 59 degrees (backward-looking). Results showed a 27% improvement in classification accuracy for spatial experiments, and also a 14% improvement in classification accuracy for spectral experiments. Figure 13 shows the ground observed azimuth and elevation of the WV-2 satellite for each image observation, as well as the azimuth and elevation of the sun during the multi-angle sequence used for the research [*Longbotham, Chaapel et al.*, 2011]. Further sections will discuss why WV-2 is capable of acquiring multi-angle imagery.

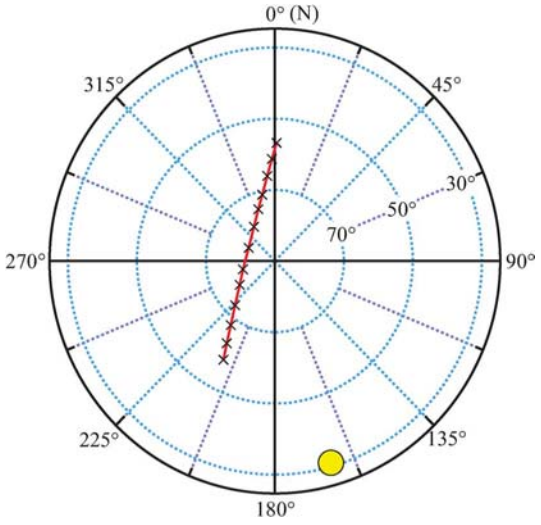

Figure 13. Ground observed azimuth and elevation of the WV-2 satellite (black markers) for each image observation as well as the azimuth and elevation of the sun (yellow circle) during the 2009 Atlanta, GA multi-angle sequence acquisition. Azimuth is plotted angularly clockwise (North: 0 degrees, East: 90 degrees, South: 180 degrees, West: 270 degrees), and elevation is plotted radially from the center (ground nadir: 90 degrees, ground horizon: 0 degrees) (From *Longbotham, Chaapel et al.* [2011])

There is significant improvement shown over the baseline classification when using a multi-angle WV-2 sequence. In terms of spatial classification, *Longbotham et al.* [2011] successfully demonstrated the ability to differentiate between classes like bridges and man-made structures, which are generally difficult to classify because they are spectrally similar to ground-level classes of the same material [*Longbotham et al.*, 2011]. Improvements were also made in terms of spectral classification—the group was able to distinguish between classes that may prove to be valuable in land-use classification, such as moving versus parked vehicles. The ability to differentiate between spectrally similar classes such as paved parking lots and paved highways were also made possible using the multi-angle sequence [*Longbotham, Bleiler et al.*, 2011].

E. PREVIOUS WORK AT THE NAVAL POSTGRADUATE SCHOOL

1. Work in Satellite Derived Bathymetry

a. Depth Analysis of Midway Atoll Using QuickBird Multi-Spectral Imaging over Variable Substrates (Camacho, 2006)

Camacho [2006] used QuickBird MSI over Midway Atoll, Northwestern Hawaiian Islands in an attempt to analyze depth and identify variable bottom-types in shallow water. The objective of this study was to use an MS image to categorize benthic substrates based on spectral characteristics and ground truth data collected *in situ*. With this image, a ratio of reflectances (the "ratio method") was used to extract depth separately over variable substrates. The motivation for this work originated from a limitation pointed out by another Naval Postgraduate School thesis student, *Clark* [2005], whose results demonstrated that the ratio method proved to be sensitive to bottom type. The method produced shallower depths over bottom types with low albedo and deeper depths over bottom types with high albedo. *Clark* [2005] also noted that sun glint had an effect on the overall results. The maximum depth that could be obtained using the ratio method was 15 meters [*Clark*, 2005].

Camacho [2006] utilized methods by *Lyzenga* [1978] and *Stumpf et al.* [2003] to extract water depth and bottom type information, and also used the ratio method to retrieve accurate depths over variable bottom types and low-albedo environments (respectively) [*Lyzenga*, 1978; *Stumpf et al.*, 2003; *Camacho*, 2006].

b. Depth Derivation from the WorldView-2 Satellite Using Hyperspectral Imagery (Loomis, 2009)

Loomis [2009] created a simulation before WV-2's launch to determine the usefulness of the Yellow band for depth derivation. *Loomis* [2009] utilized data from the Airborne Visible/InfraRed Imaging Spectrometer (AVIRIS) sensor over Kaneohe Bay, Hawaii, and then processed the imagery using the *Stumpf et al.* [2003] ratio method to determine bathymetry. The Green & Blue, Yellow & Green, and Yellow & Blue band combinations were compared to ground truth bathymetry derived from a digital nautical

chart. Results indicated that use of the Yellow band improved the accuracy of derived depths, especially in shallow water [*Loomis*, 2009].

c. Contributions to Remote Sensing of Shallow Water Depth with the WorldView-2 Yellow Band (Madden, 2011)

Following *Loomis'* [2009] work, *Madden* [2011] analyzed bathymetry in Tampa Bay, Florida's shallow water using WV-2 imagery. The Yellow band was combined separately with the Blue, Green, and Red bands, and then compared to the more traditional Blue & Green and Green & Red combinations. *Madden's* [2011] results showed that the addition of the Yellow band provided more information about bathymetry, but less sensitivity to bottom type in two of three transect lines used [*Madden*, 2011].

2. Work in Multi-Observation Imagery

a. Coastal Bathymetry Using 8-Color Multispectral Satellite Observation of Wave Motion (McCarthy, 2010)

McCarthy [2010] measured coastal bathymetry near Camp Pendleton in California by using wave motion as observed by WV-2. After principal component transforms were performed, successive change detection images contained both spatial and temporal information. Wave celerity could be determined and depth inversion was performed. *McCarthy* [2010] measured the wavelength of a wave above a known depth, and then used the wave period method to determine depth for other waves in the propagation direction of that particular wave. *McCarthy* [2010] determined that the spatial resolution for this method was higher and possibly more accurate than the reference bathymetry used, especially in the surf zone [*McCarthy*, 2010].

b. Coastal Bathymetry Using Satellite Observation in Support of Intelligence Preparations of the Environment (Myrick, 2011)

Myrick [2011] followed *McCarthy's* [2010] work, and calculated water depths using linear dispersion relationships for surface gravity waves. *Myrick* [2011] was able to establish depth profiles out to 1 kilometer offshore, as well as derive depths up to

15 meters. Comparisons with United States Geological Survey (USGS) bathymetric acquisitions from 2009 show agreement within 5% in the surf zone and 1% outside of the surf zone [*Myrick*, 2011].

c. Automating Nearshore Bathymetry Extraction from Wave Motion in Satellite Optical Imagery (Mancini, 2012)

Mancini [2012] extracted nearshore depths for Waimanalo Beach, Hawaii from WV-2 optical imagery by means of automated wave kinematics bathymetry (WKB). Two sets of three sequential images, acquired at approximately 10 second intervals, were used. Depths from close to shore out to about 20 meters deep were generated. Comparisons to the Scanning Hydrographic Operational Airborne Lidar Survey (SHOALS) LiDAR bathymetry values showed WKB depths were accurate to about 0.5 meters, with R^2 values of 90%, and were frequently in the range of 10% to 20% relative error for depths ranging from 2 to 16 meters [*Mancini*, 2012].

d. High Spatial Resolution Bidirectional Reflectance Retrieval Using Satellite Data (McConnon, 2010)

McConnon [2010] analyzed 15 WV-2 images acquired over Duck, North Carolina and 10 images of Pendleton, California to extract BRDF. Separation angles between the inbound, solar zenith angle, and the outbound reflectance angle were calculated. BRDF shifts across wavelengths and regions of interest (ROIs) were plotted against the previously mentioned values and then examined [*McConnon*, 2010].

THIS PAGE INTENTIONALLY LEFT BLANK

III. DATA AND METHODS

A. DATA

1. Satellite Sensor, Study Site, and Imagery Dataset

a. WorldView-2 (WV-2)

WorldView-2, launched on 8 October 2009 from Vandenberg Air Force Base, is DigitalGlobe's third operational satellite after QuickBird and WorldView-1. The sensor is in a nearly circular, sun-synchronous orbit, and flies at an altitude of approximately 770 kilometers (Table 1). At nadir, the best possible spatial resolution is 0.46 meters (panchromatic) and 1.84 meters (MS). What differentiates WV-2 from DigitalGlobe's previous sensors is its 9 spectral bands—one panchromatic (PAN), ranging from approximately 450 to 800 nm (centered at 632 nm), and 8 MS, ranging from approximately 400 to 1050 nm (Figure 14, Table 2). These MS bands include: Coastal (centered at 427 nm), Blue (centered at 478 nm), Green (centered at 546 nm), Yellow (centered at 608 nm), Red (centered at 659 nm), Red Edge (centered at 724 nm), NIR-1 (centered at 831 nm), and NIR-2 (centered at 908 nm) (available at http://www.digitalglobe.com/about-us/content-collection#satellites&worldview-2).

Table 1. WV-2 Design and Specifications (After information available at http://www.digitalglobe.com/about-us/content-collection#satellites&worldview-2)

Launch Information	**Date: October 8, 2009** **Launch Site: Vandenberg AFB, CA, USA**
Orbit	Altitude: 770 km Type: Sun synchronous Period: 100 minutes
Sensor Resolution	Panchromatic: 0.46 m GSD at nadir, 0.52 m GSD at 20 degrees off-nadir Multispectral: 1.85 m GSD at nadir, 2.07 m GSD at 20 degrees off-nadir
Swath Width	16.4 km at nadir
Attitude Determination and Control	3-axis stabilized Actuators: Control Moment Gyros (CMGs) Sensors: Star trackers, solid state IRU, GPS
Pointing Accuracy and Knowledge	Accuracy: <500 m at image start and stop Knowledge: Supports geolocation accuracy below
Retargeting Agility	Time to Slew 200 km: 10 seconds
Revisit Frequency (at 40 degrees N Latitude)	1.1 days at 1 m GSD or less 3.7 days at 20 degrees off-nadir or less (0.52 m GSD)
Geolocation Accuracy	Demonstrated <3.5 m CE90 without ground control
Capacity	1 million sq km per day

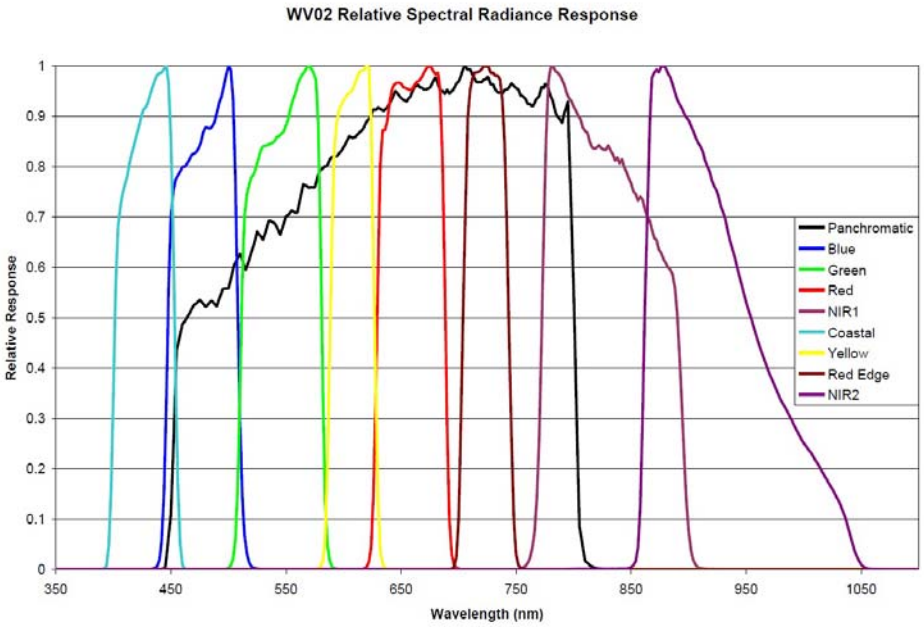

Figure 14. WV-2's relative spectral radiance response (From *Updike and Comp* [2010])

Table 2. WV-2 Sensor Bands (After information available at http://www.digitalglobe.com/about-us/content-collection#satellites&worldview-2)

Band	Band Width (nm)	Center Wavelength (nm)
Panchromatic	450 – 800	632
Coastal	400 – 450	427
Blue	450 – 510	478
Green	510 – 580	546
Yellow	585 – 625	608
Red	630 – 690	659
Red Edge	705 – 745	724
NIR-1	770 – 895	831
NIR-2	860 - 1040	908

The WV-2 system's 8 MS bands are arranged in two arrays of 4 MS bands each (MS1 and MS2). MS1 includes Blue, Green, Red, and NIR-1. MS2 is comprised of Coastal, Yellow, Red Edge, and NIR-2. Imaging options are: PAN only, PAN + MS1, and PAN + 8 MS (MS1 and MS2). There is a 0.3 second delay between MS1 and MS2 acquisitions, according to G. Miecznik (unpublished data, 2012).

When combined, these bands are designed to improve the segmentation and classification of land and aquatic features beyond any other multispectral satellite imager. After WV-2's launch, it was speculated that the increased agility and addition of the Coastal band would improve remote bathymetric measurements (mainly due to the Coastal band's wavelength value, making it least absorptive by water). Analysts expected to be able to calculate depths up to 20 meters, and possibly even 30 meters using the Coastal, Blue, and Green bands. Once scientists were able to utilize WV-2 imagery, the Coastal band has proven to be useful for the retrieval of water depth, true-color correction for human vision representation, chlorophyll absorption, and atmospheric scattering correction [*Pacifici and Navular*, 2011; *Marchisio et al.*, 2011]. Also, with an average revisit time of 1.1 days and the ability to utilize off-nadir pointing, WV-2 was expected to better monitor ocean environments, which are highly dynamic and constantly changing (information available at http://www.satimagingcorp.com/media/pdf/Bathymetry_Datasheet.pdf).

Bi-directional scanning is supported by WV-2. The onboard camera has a standard maximum look angle of approximately 40 degrees off-nadir and can slew across 300 kilometers of the Earth's surface in 9 seconds. This unique agility enables WV-2 to collect dense image sequences of a single target from several observation angles as it overflies an area [*Longbotham et al.*, 2011].

b. Kailua Bay, Oahu, Hawaii

This study focused on one location on the windward side of the Oahu coastline of Hawaii – Kailua Bay (Figure 15). The bay's approximate latitude/longitude is: 21 degrees 24' 29" N, 157 degrees 44' 09" W. This particular beach was chosen because it was the least cloudy out of the 39 WV-2 images in the acquired dataset.

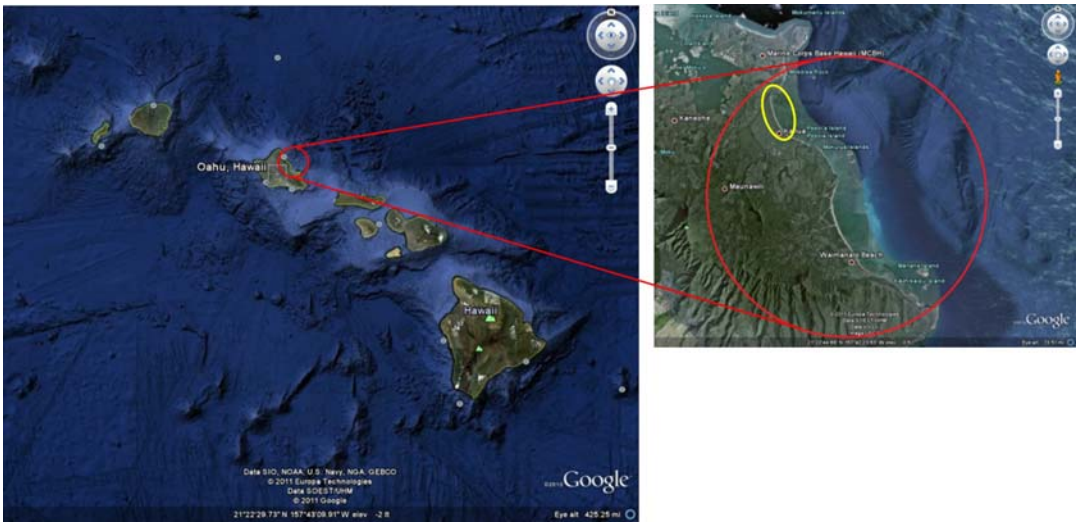

Figure 15. The Hawaiian Islands (left), focusing on Kailua Bay, Oahu (right) (From Google Earth)

Kailua Bay is a carbonate reef-dominated embayment. There are two categories of benthic substrate found here: areas of carbonate sand and fossil reef hardgrounds, and reef habitats of coral and algae species. There is a sand-floored channel at the center of the bay, which cuts across the reef and connects the seaward and nearshore sand fields. Algae and corals grow on the plains [*Isoun et al.*, 2003].

Areas with sand and fossil reef appear light-colored and are highly reflective in the WV-2 imagery. The coral and algae communities look dark and have low reflectance [*Isoun et al.*, 2003]. Aerial images are shown in Figure 16.

Figure 16. Oblique aerial imagery acquired over Kailua Bay on 10 November 2003 on a Nikon Coolpix 5700 digital camera (settings and focus all automated) from a Cessna plane flying at about 2,000 feet (From http://www.soest.hawaii.edu/coasts/erosion/oahu/oblique.php)

c. Imagery Dataset

A collection of 39 multispectral images of the windward side of Oahu, Hawaii was acquired by the WorldView-2 satellite on 30 July 2011 between 21:22:49Z and 21:28:54Z. Images were acquired at approximately 10 second intervals, covering just over 6 minutes (Figure 17). Section A of the Appendix contains a sample WV-2 metadata file.

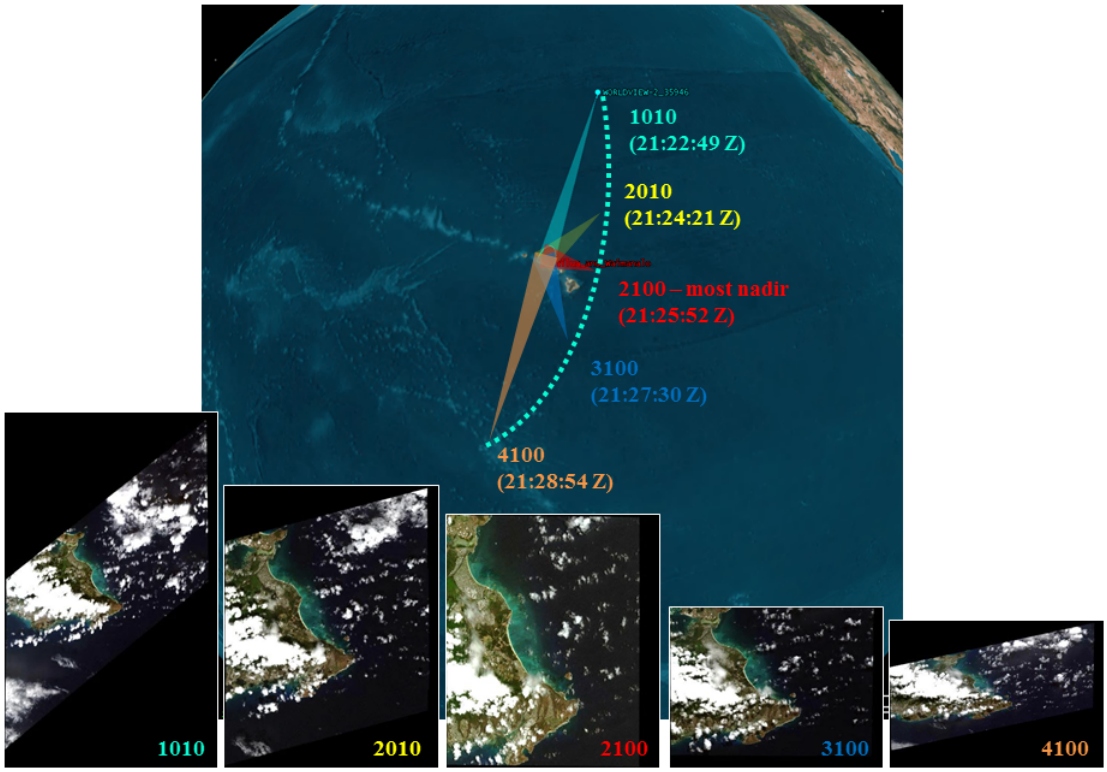

Figure 17. Five examples out of the 39 WV-2 image acquisitions (labels are actual Image IDs)

2. Bathymetry Data

Bathymetry data of Kailua Bay were acquired from the University of Hawaii at Manoa, School of Ocean & Earth Science & Technology, Department of Geology and Geophysics (data are available at http://www.soest.hawaii.edu/coasts/data/oahu/shoals.html and information about this dataset is available at http://www.soest.hawaii.edu/coasts/data/readme.html#shoals). According to the University of Hawaii website, these bathymetry data were collected from the SHOALS

website, as part of a survey conducted in 2000 (information is available at http://shoals.sam.usace.army.mil/hawaii/pages/Oahu.htm). After investigating the origins of the dataset, however, and determining that these data were not collected by SHOALS in 2000, it is now believed that the data were collected by USGS circa 2002 to 2005. This information was provided by C. Fletcher (unpublished data, 2012). Prior to the completion of this particular project, there was no resolution concerning the actual details about the dataset.

3. Software

a. Environment for Visualizing Images + Interactive Data Language 4.8 (ENVI 4.8 + IDL)

Environment for Visualizing Images (ENVI) 4.8 was the main software program used for data analysis and manipulation. ENVI is an image processing software system designed for multi- and hyperspectral data analysis and information extraction. This software is written in the Interactive Data Language (IDL), a programming language that provides integrated image processing and display capabilities [Research Systems, 2004; *Camacho*, 2006].

ENVI was used to process the WV-2 imagery. All image mosaicking, spatial subsetting and chipping, radiance calibration, and registration was performed in ENVI. A number of IDL programs were written for each combination of two WV-2 bands tested, and each incorporated a section to create masks for land, clouds, whitecaps, and glint, as well as apply a band ratio method for depth determination (see Section C of the Appendix).

B. METHODS

A number of pre-processing steps were performed before bathymetric derivation could occur. First, images were mosaicked and analyzed for overall quality and cloud cover. The next steps included map coordinate conversion, radiance calibration, land/cloud mask creation, sun glint removal, and the application of a ratio method for bathymetry derivation.

1. Bathymetry Derivation

a. Assess Data Coverage, Angles, and Quality

Before any data preparation steps occurred, images were assessed. It was important to ensure that imagery were collected over the correct site, and that datasets did not include any bad data. Scenes were ordered by mean satellite elevation angle (from most forward-looking, to most nadir, to most backward-looking). Table 3 and Section B of the Appendix list all 39 images acquired over Oahu.

Table 3. List of WorldView-2 Images

Image ID	firstLineTime (Z)	meanSatEl	meanSatAz	meanOffNadirViewAngle	Azimuth	Zenith
1010	21:22:49	24.9	18.8	54.1	-161.2	125.9
1020	21:22:58	26.5	19.2	53.1	-160.8	126.9
1030	21:23:07	28.1	19.6	52.0	-160.4	128.0
1040	21:23:16	29.8	20.1	50.8	-159.9	129.2
1050	21:23:25	31.7	20.6	49.5	-159.4	130.5
1060	21:23:34	33.7	21.2	48.0	-158.8	132.0
1080	21:23:53	38.2	22.6	44.6	-157.4	135.4
1090	21:24:02	40.8	23.5	42.6	-156.5	137.4
1100	21:24:12	43.7	24.6	40.3	-155.4	139.7
2010	21:24:21	46.7	26.0	37.8	-154	142.2
2020	21:24:31	50.1	27.6	35.1	-152.4	144.9
2030	21:24:41	53.6	29.7	32.1	-150.3	147.9
2040	21:24:51	57.6	32.4	28.7	-147.6	151.3
2050	21:25:01	61.6	36.1	25.2	-143.9	154.8
2060	21:25:12	66.0	41.5	21.4	-138.5	158.6
2070	21:25:22	70.2	49.2	17.4	-130.8	162.3
2080	21:25:32	74.0	61.2	14.3	-118.8	165.7
2090	21:25:42	76.9	80.1	11.7	-99.9	168.3
2100	21:25:52	77.8	105.5	10.9	-74.5	169.1
3010	21:26:02	76.3	129.8	12.1	-50.2	167.9
3020	21:26:12	73.1	146.9	15.0	-33.1	165.0
3030	21:26:23	69.0	157.9	18.6	-22.1	161.4
3040	21:26:33	64.8	164.7	22.2	-15.3	157.8

Image ID	firstLineTime (Z)	meanSatEl	meanSatAz	meanOffNadirViewAngle	Azimuth	Zenith
3050	21:26:43	60.6	169.4	25.9	-10.6	154.1
3060	21:26:53	56.6	172.8	29.2	-7.2	150.8
3070	21:27:02	52.9	175.3	32.4	-4.7	147.6
3080	21:27:12	49.6	177.2	35.2	-2.8	144.8
3090	21:27:21	46.5	178.7	37.8	-1.3	142.2
3100	21:27:30	43.7	179.9	40.0	-0.1	140.0
4010	21:27:39	41.1	180.9	42.2	0.9	137.8
4020	21:27:47	38.7	181.7	44.0	1.7	136.0
4030	21:27:56	36.5	182.5	45.7	2.5	134.3
4040	21:28:04	34.4	183.1	47.3	3.1	132.7
4050	21:28:13	32.5	183.7	48.7	3.7	131.3
4060	21:28:21	30.7	184.2	50.0	4.2	130.0
4070	21:28:29	29.0	184.6	51.2	4.6	128.8
4080	21:28:38	27.4	185.0	52.3	5.0	127.7
4090	21:28:46	25.9	185.4	53.3	5.4	126.7
4100	21:28:54	24.5	185.7	54.2	5.7	125.8

b. Mosaic Data

Data files were delivered in such a way that scenes needed to be mosaicked. This step was performed to be able to better view the entire coastline. Spatial subsetting could then occur without worrying about areas that may not have full coverage because the rest of the scene was in a different file. Figure 18 shows example images after mosaicking.

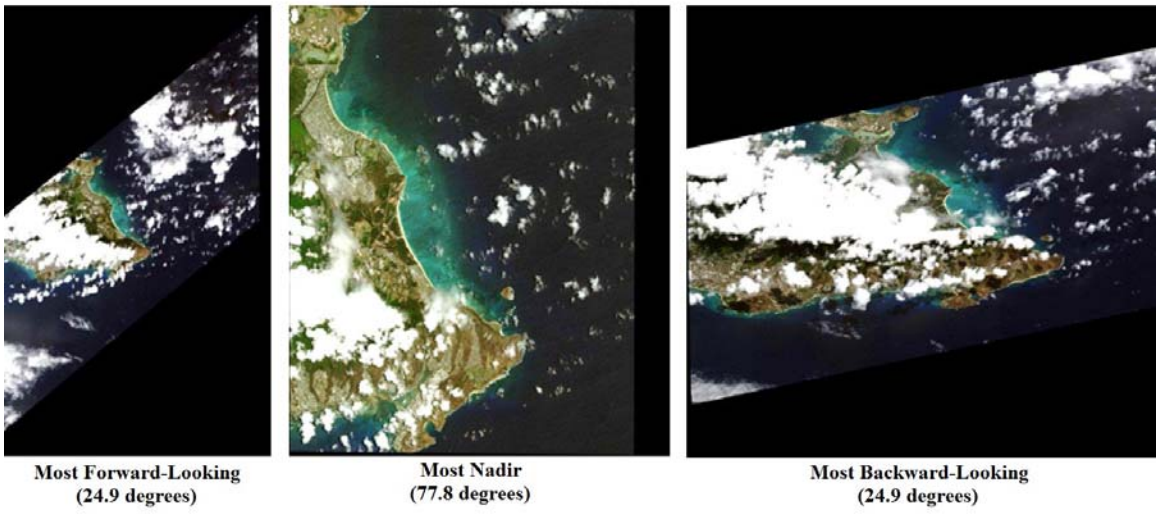

Figure 18. The most forward-looking, nadir, and backward-looking images after data coverage assessment and mosaicking

c. Convert Map Projection

Level 1B (Basic) images were used, meaning that data were not projected to a plane using a map projection or datum and needed to be converted to Universal Transverse Mercator (UTM), World Geodetic System 1984 (WGS-84), Zone 4N (information is available at http://www.digitalglobe.com/downloads/ DigitalGlobe_Core_Imagery_Products_Guide.pdf). Pixels were also made square. Figure 19 shows how the map projection conversion affected the look of the imagery.

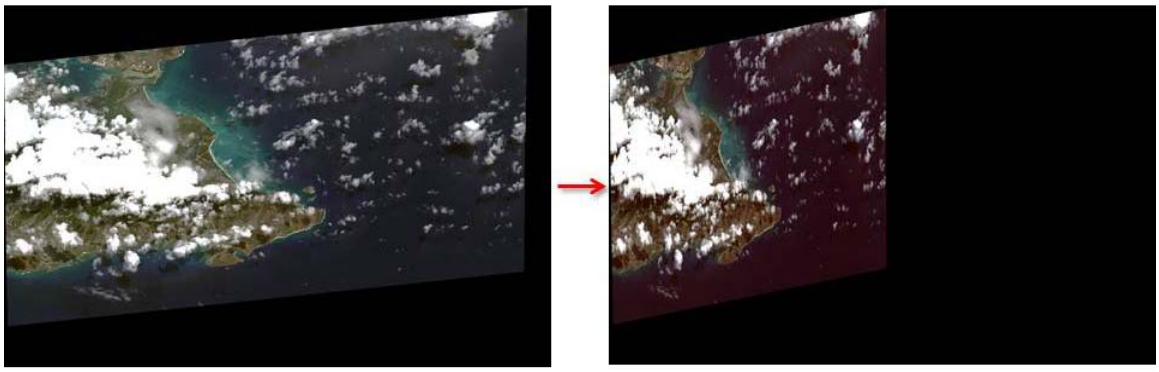

Figure 19. Map projection conversion from Geographic Latitude/Longitude (left) to UTM, WGS-84, Zone 4N (right)

d. Radiance Calibration

The WV-2 spectral radiance response is defined as the ratio of the number of photo-electrons measured by the system, to the spectral radiance [$W\text{-}m^{-2}\text{-}sr^{-1}\text{-}\mu m^{-1}$] at a certain wavelength present at the entrance to the telescope aperture. The spectral radiance response for each band is normalized by dividing by the maximum response value for that band to arrive at a relative spectral radiance response [*Updike and Comp*, 2010].

Relative radiometric calibration and correction are necessary. This is because a uniform scene does not create a uniform image when it comes to raw digital numbers (DNs). This type of correction minimizes image artifacts, such as vertical streaks or bands due to differences in gain or offset, and is performed on raw data from all detectors in all bands during the early stages of WV-2 product generation. The products are linearly scaled to absolute spectral radiance [*Updike and Comp*, 2010].

In the case of large mosaics, radiometric balancing will help match the brightness of the other scenes used in the mosaic [*Updike and Comp*, 2010]. As glint removal is performed on images after the radiance calibration step, all images were left in radiance for this research.

e. Subset Data

Images were subset to focus on Kailua Bay (Figure 20). This was done to reduce file size, emphasize a spot with interesting and variable bathymetry, as well as to better concentrate on a specific location that had less cloud cover.

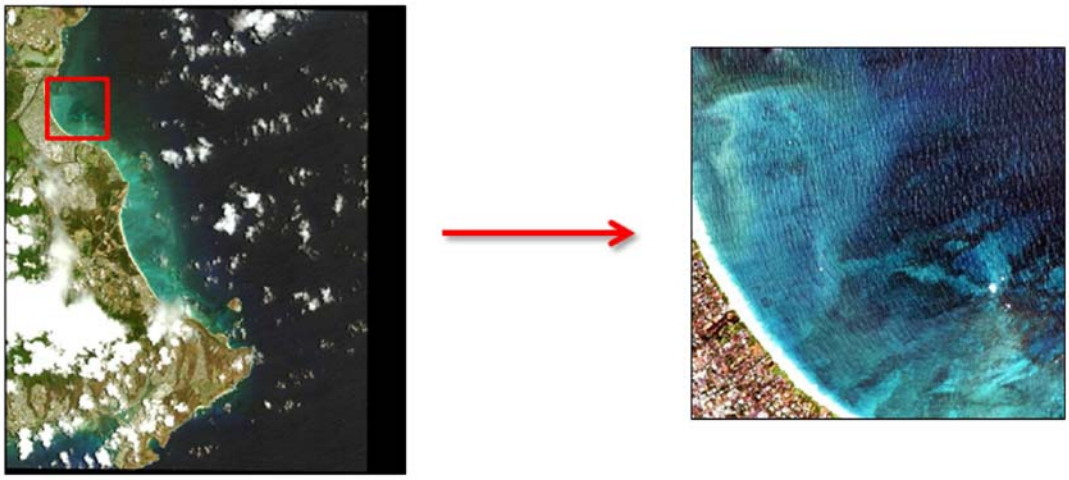

Figure 20. The full scene (left) was chipped to focus on Kailua Bay (right)

f. Registration of Off-Nadir Images to the Most Nadir Image

All non-nadir images were registered to the most nadir image. Twenty tie points were interactively selected for the same locations in all of the non-nadir images. The data were then warped using a first order polynomial. Maximum pixel error for the registrations was 1.521 pixels with an average root mean square (RMS) error of about 0.895 pixels for the entire dataset. Images were then re-chipped so that every scene covered the same geographic coordinates. All chips were reduced to 995 samples and 999 lines. An example is shown in Figure 21.

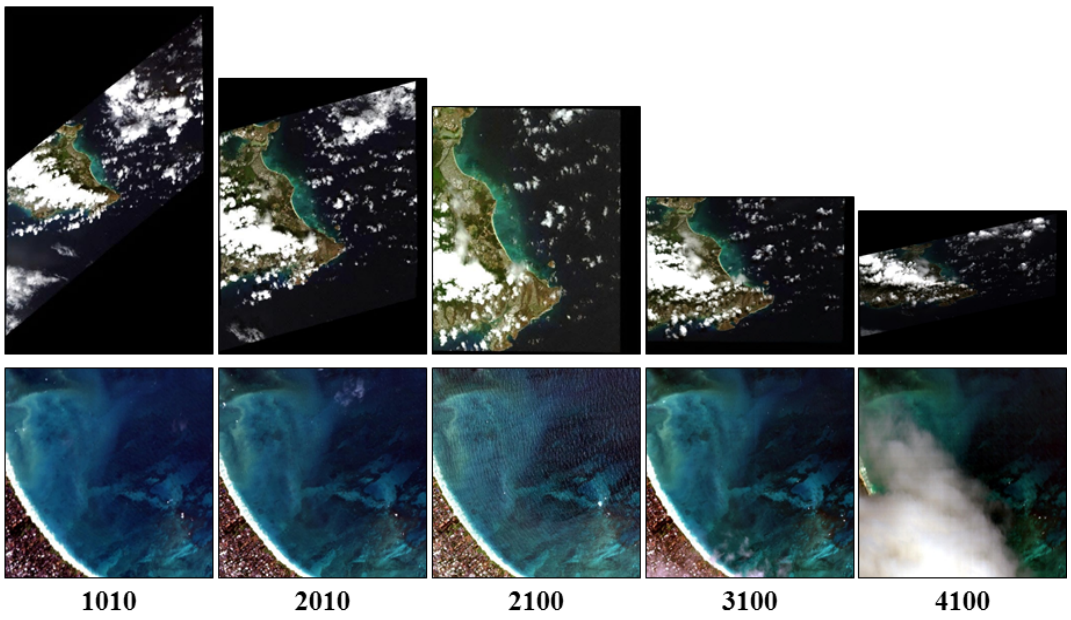

Figure 21. After registration, each image (top) was chipped to the 995 x 999 pixel scene shown (bottom)

g. Land, Glint, Cloud, and Whitecap Masks

Application of spatial masks for land, glint, cloud, and whitecap areas allows analysis to be limited to only the areas and materials of interest. Masks were determined by comparing scatter plots using the Blue and NIR-1 bands. Water regions are those in the lower left portion of the scatter plot, as can be seen in Figure 22.

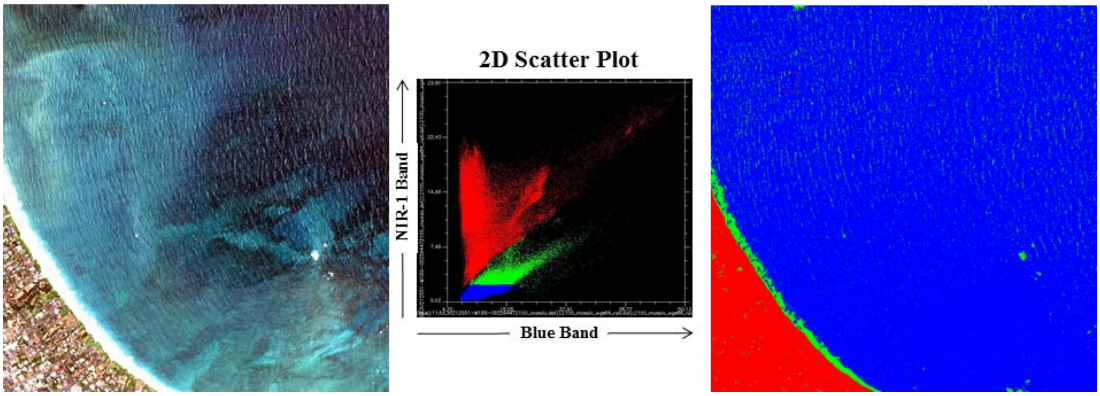

Figure 22. The original image (left) has a corresponding scatter plot (middle); specific sections of the plot are highlighted to show how they correspond to the image (right)—red is mostly land, green is mostly whitecaps and sun glint, and blue is water

The scatter plot classified land, glint, clouds, and whitecaps as any pixels with values greater than the user-defined points chosen within the plot. Every other pixel would, therefore, be considered not land, glint, clouds, or whitecaps and would not be masked (Figure 23). Figure 24 illustrates how Figure 23's user-defined region affects the imagery.

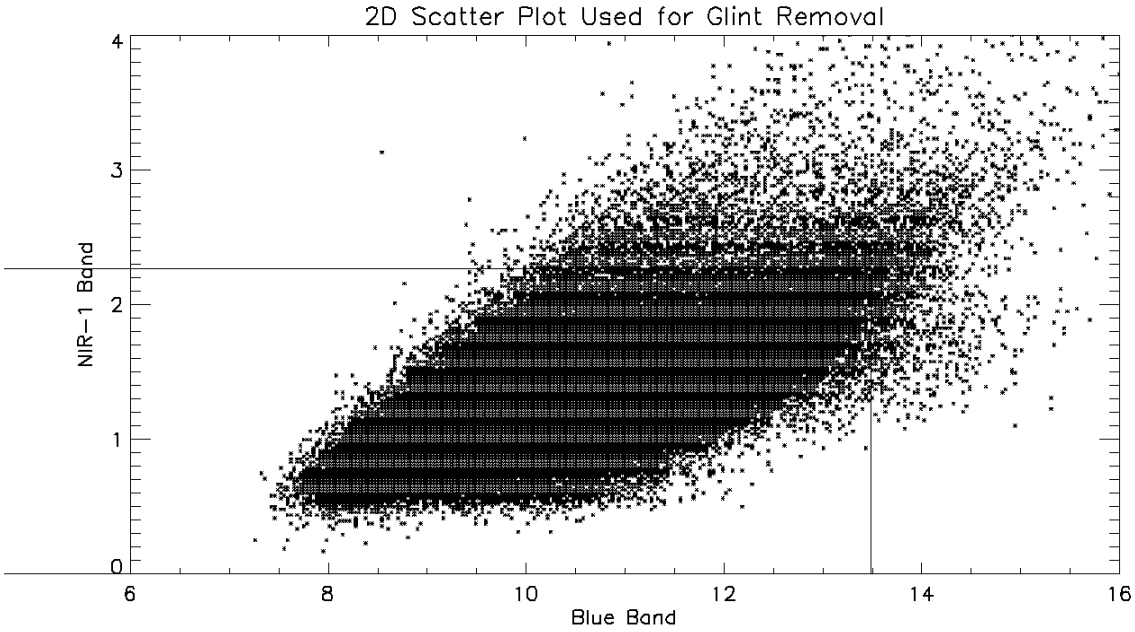

Figure 23. 2D scatter plot of the Blue vs. NIR-1 bands; the user-defined outline region includes pixels containing water, and everything else can generally be classified as land, clouds, glint, whitecaps, etc. (e.g., not water)

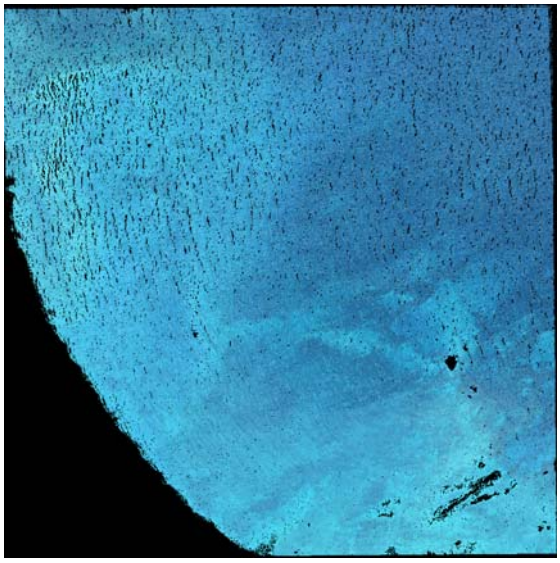

Figure 24. Land, glint, clouds, and whitecaps have been masked in this image

h. Glint Removal

As discussed previously, if the ocean surface is perfectly flat, the reflection of the sun appears as a bright, small portion of the sea surface. If the ocean surface is not flat due to stronger winds, however, parts of the water surface further from the center of the sun glint pattern will be at the required orientation to reflect sun light to the viewer. Therefore, the sun's reflection will cover a larger part of the ocean surface, and will be made up of many tiny highlights that each reflect from a particular point on the surface from the sun. The brightness of each pixel equals the total brightness of all highlights in that pixel and is, therefore, proportional to the fraction of the sea surface at the right slope [*Kay et al.*, 2009].

If the sun and sensor are treated as a point source and detector for a given viewing geometry, there is only one facet slope and orientation that is consistent with specular reflection. The sun, in reality, has an angular diameter of 0.53 degrees, so there is a range of possible slopes that can reflect light from some part of the sun's disc into the sensor [*Kay et al.*, 2009].

Steps to remove glint were applied to the two WV-2 bands that were the focus of each version of code (Section C of the Appendix). The method used was based

on the method revised by *Hedley et al.* [2005] after *Hochberg et al.* [2003]. Work by *Hedley et al.* [2005] establishes the linear relationship between NIR and VIS bands using a linear regression based on a sample of the image pixels. Over areas with underlying spectral brightness, such as deep water, one or more regions with a range of sun glint are selected. For each VIS band, all selected pixels are included in a linear regression of NIR brightness (x-axis) against the VIS band brightness (y-axis). If the slope of this line for band i is b_i, then all the pixels in the image can be deglinted in band i by applying the following equation:

$$R'_i = R_i - b_i(R_{NIR} - \mathrm{Min}_{NIR}), \tag{2}$$

which means: reduce the pixel value in band i (R_i) by the product of regression slope (b_i) and the difference between the pixel NIR value (R_{NIR}) and the ambient NIR level (Min_{NIR}). R'_i is the sun glint corrected pixel brightness in band i. Min_{NIR} represents the NIR brightness of a pixel with zero sun glint, and can be estimated by the minimum NIR found in the regression sample or as the minimum NIR value found in the entire image [*Hedley et al.*, 2005]. Refer to Figure 25 for a graphical interpretation of the *Hedley et al.* [2005] method.

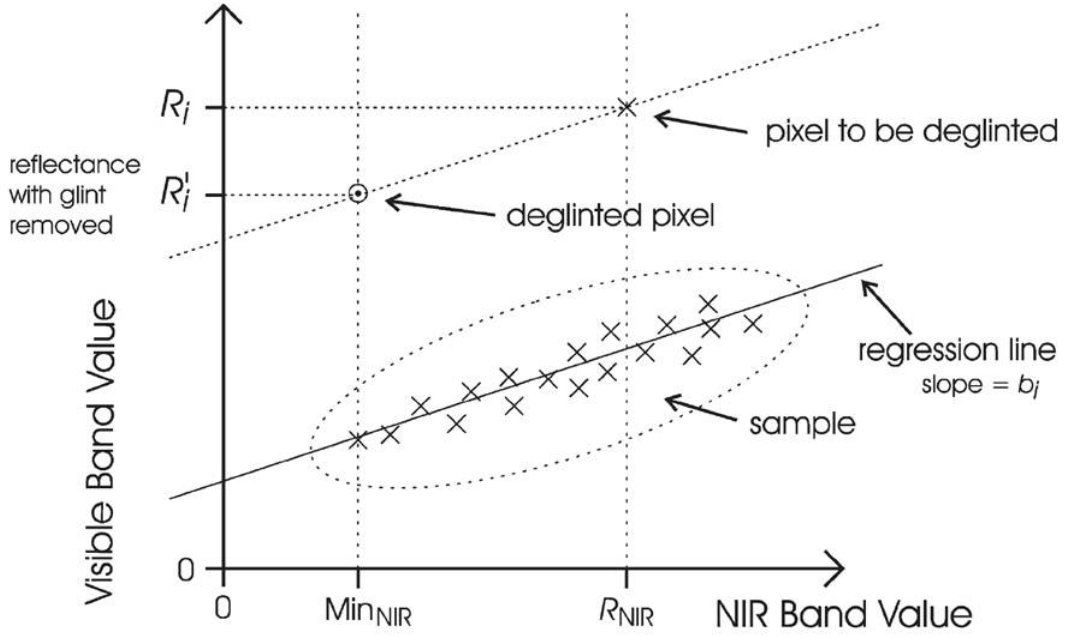

Figure 25. Graphical interpretation of the *Hedley et al.* [2005] de-glinting method (From *Hedley et al.* [2005])

The analysis incorporates the slope of the regression line. A simplified example of the modified equation used in the code (Section C of the Appendix) is as follows:

Green = Green - Slope of Green Regression Line * (NIR-1 – MinNIR-1) (3)

Yellow = Yellow - Slope of Yellow Regression Line * (NIR-2 – MinNIR-2) (4)

There are, however, a number of differences between the *Hedley et al.* [2005] method and the one used for this research. This code utilized only two of the six possible WV-2 VIS bands at a time. It also focused on the entire, global scene, rather than a small, local portion (only deep water, for example). It also incorporated masking, which was not used in the *Hedley et al.* [2005] research [*Hedley et al.*, 2005] (refer to Section C of the Appendix).

i. Band Ratio to Determine Relative Bathymetry

A two-step process was used to derive bathymetry. Relative bathymetry was determined by performing a band ratio method, and then derived bathymetry values were obtained by regressing relative bathymetry values against verified depth data (to be further discussed in the upcoming sections). *Camacho* [2006] calculated relative bathymetry using the natural log transformed reflectance values of the deglinted reflectance image [*Camacho*, 2006]:

$$\ln(1000*b1)/\ln(1000*b2) \quad (5)$$

The relative bathymetric values in this research were extracted using the following expression, with a slight adjustment to the constant value used by *Camacho* [2006]:

$$\ln(100*b1)/\ln(100*b2) \quad (6)$$

where b1 is the first band used, and b2 is the second. This is a modification of the equation used by *Stumpf et al.* [2003] [*Stumpf et al.*, 2003].

j. Comparison of Water Depths to LiDAR Bathymetry

The bathymetry data of Kailua Bay were acquired in shapefile format. They were then converted to a raster in the proper map projection, geographically linked to the image chip, and then clipped to the 995 by 999 pixels-size. These data were then used as the "true" data.

k. Derived Bathymetry

Derived depth values were calculated by regressing the relative depth values with the actual depth values collected by the "true" bathymetry. The chi-squared and correlation values were additional IDL code outputs that helped determine the "goodness of fit." A lower chi-squared value is indicative of a better fit. Correlation values are interpreted as percentages, so the highest value represents the best fit.

2. Analyze Effects of Collection Geometry on Water Depth Derivation

The effects of collection geometry on water depth derivation were analyzed by running all 39 images through the processing and analysis approach described above. Chi-squared and correlation values were recorded, and images of derived depth versus actual "true" depth plots were compared. Results will be discussed further in the following section.

THIS PAGE INTENTIONALLY LEFT BLANK

IV. RESULTS

A total of 39 bathymetric maps were generated from the WV-2 data using the previously described band ratio method. The accuracies of these maps were then evaluated using "true" bathymetry data from the University of Hawaii at Manoa. The final WV-2 derived bathymetry was produced by regressing the relative bathymetry values against the actual "true" bathymetric measurement. The chi-squared and correlation values were then compared to analyze effects of multi-angle acquisition on depth derivation.

A. BATHYMETRY FROM ENTIRE IMAGE

A total of 39 bathymetric maps from a WV-2 multi-angle sequence over Kailua Bay, Oahu, Hawaii were generated. The following band combinations were analyzed:

- Coastal & Blue,
- Coastal & Green,
- Blue & Green, and
- Green & Yellow.

Each band combination was analyzed using the band ratio method to obtain relative bathymetry. These values were then regressed against the "true" bathymetry data shown in Figure 26.

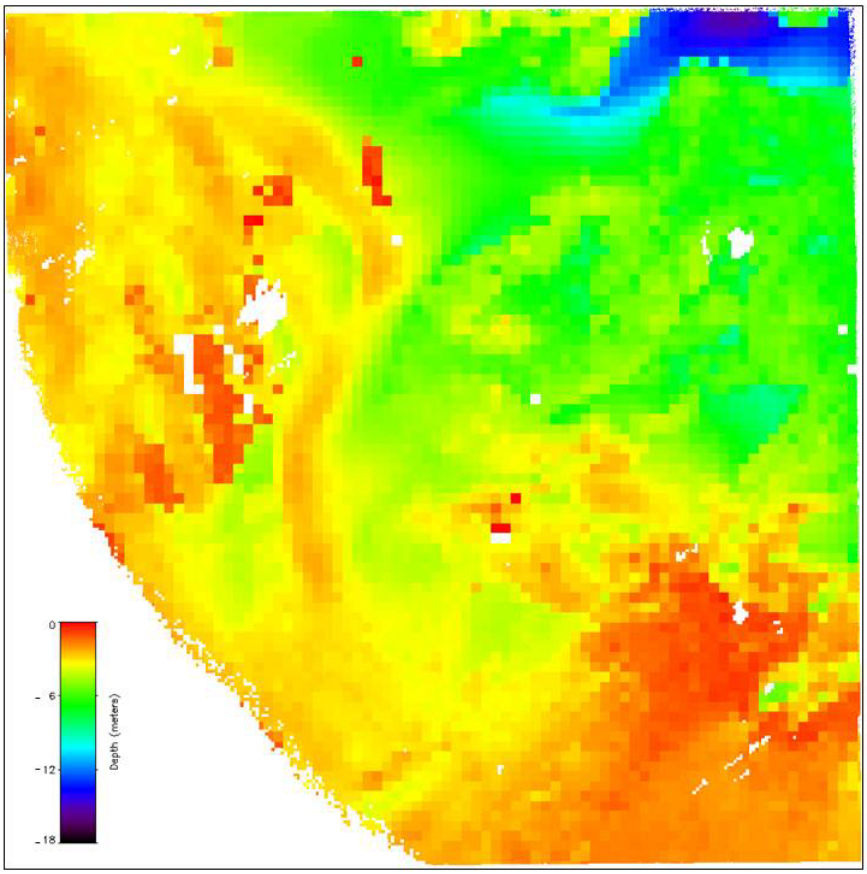

Figure 26. "True" bathymetry data; depth is represented by the Rainbow scale (shallow water is red and deep water is black)

The results of the regression were the derived depth values. These were scaled to meters and plotted. Derived depth plots from Image IDs 1010 (most forward-looking), 2010, 2100 (most nadir), 3100, and 4100 (most backward-looking) are shown in Figures 27 through 31 for each band combination. All images have the same scale, a range of depths from 0 (red) to -18 (black) meters.

1010

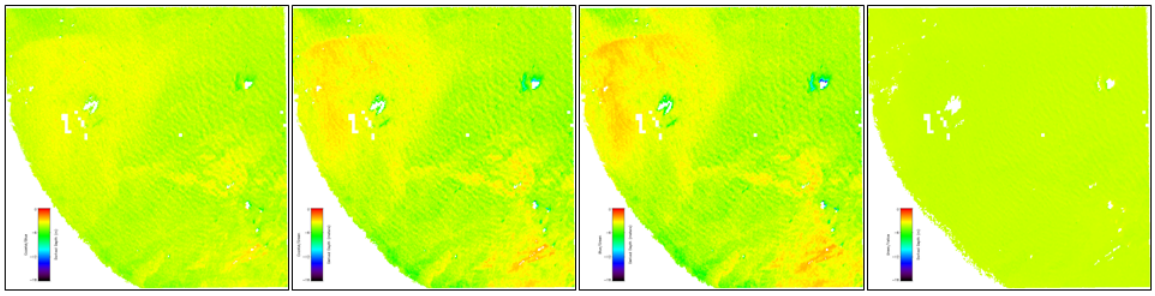

Coastal & Blue | Coastal & Green | Blue & Green | Green & Yellow

Figure 27. Derived depths for each band combination for Image 1010 (most forward-looking)

2010

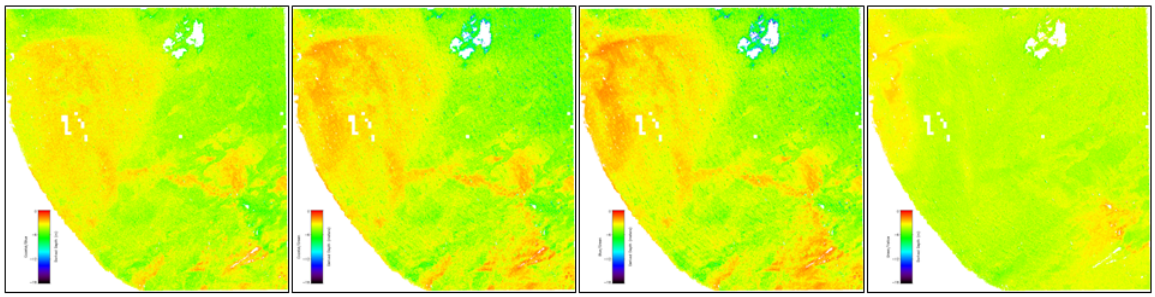

Coastal & Blue | Coastal & Green | Blue & Green | Green & Yellow

Figure 28. Derived depths for each band combination for Image 2010

2100

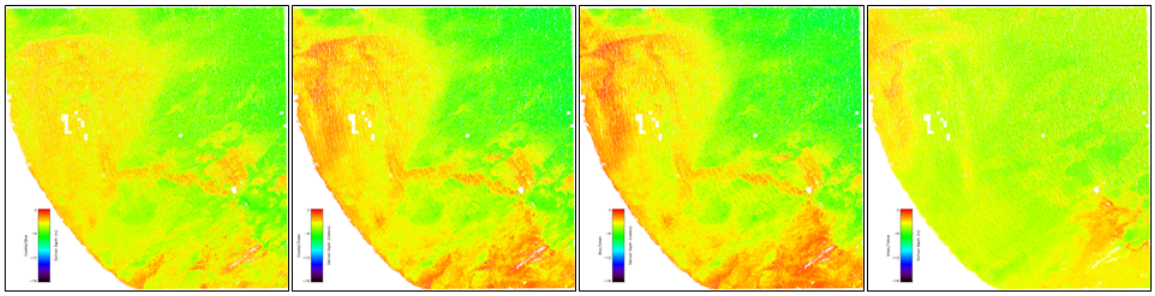

Coastal & Blue | Coastal & Green | Blue & Green | Green & Yellow

Figure 29. Derived depths for each band combination for Image 2100 (most nadir)

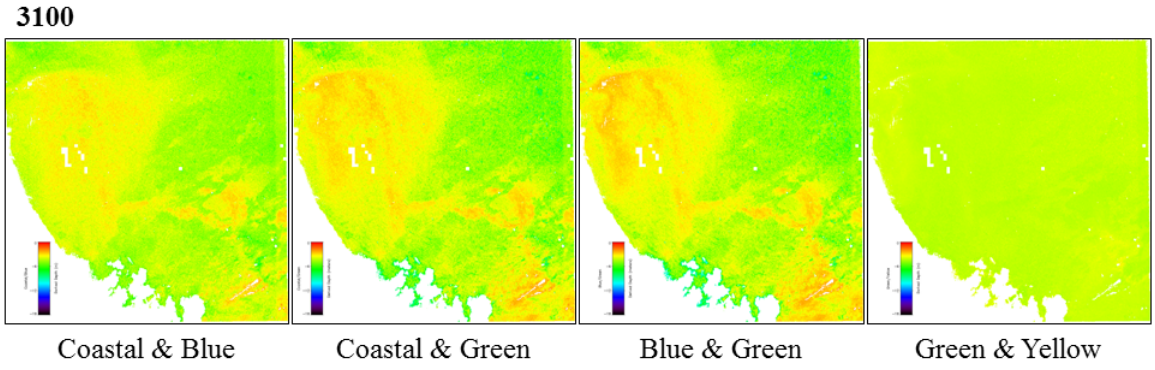

Figure 30. Derived depths for each band combination for Image 3100

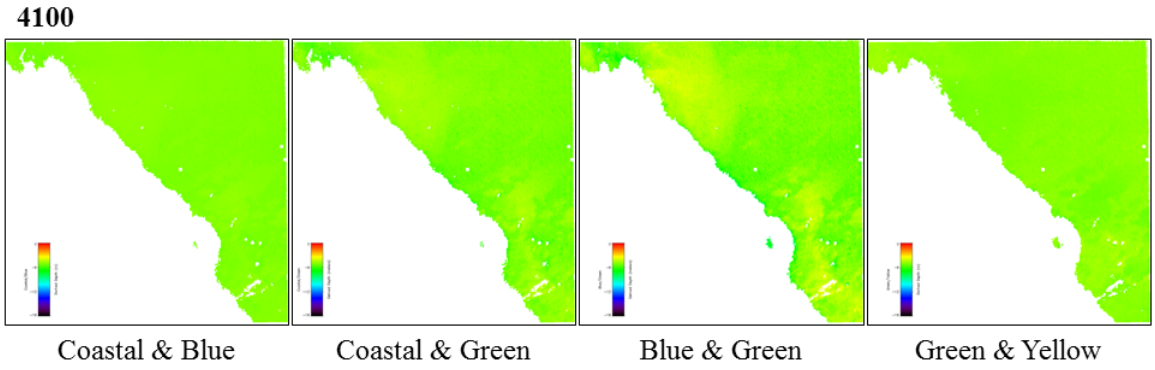

Figure 31. Derived depths for each band combination for Image 4100 (most backward-looking)

It can be seen that none of these derived depth maps come close to a perfect correlation to the "true" bathymetry data. This most likely has to do with a number of factors, including high off-nadir acquisition angle and also cloud cover (seen as white, masked data in Figures 30 and 31). Due to the fact that wave patterns can be seen in the derived depth images, it is also speculated that a better glint removal method may be required in order to derive more accurate depths.

Examination of these images shows that the Coastal & Green and Blue & Green WV-2 band combinations tend to perform better. Also, derived depth more closely matches the "true" depth as the sensor is acquiring images closer to nadir.

B. VARIATION IN ACQUISITION ANGLES

In order to better understand the effect of acquisition angle on depth determination, plots of derived depth versus "true" depth for Image IDs 1010 (most forward-looking), 2010, 2100 (most nadir), 3100, and 4100 (most backward-looking) were created and compared. The chi-squared and correlation values of each were determined and are displayed for Image ID 2100 (most nadir) in Figures 32 through 35 (the rest can be located in Section D of the Appendix).

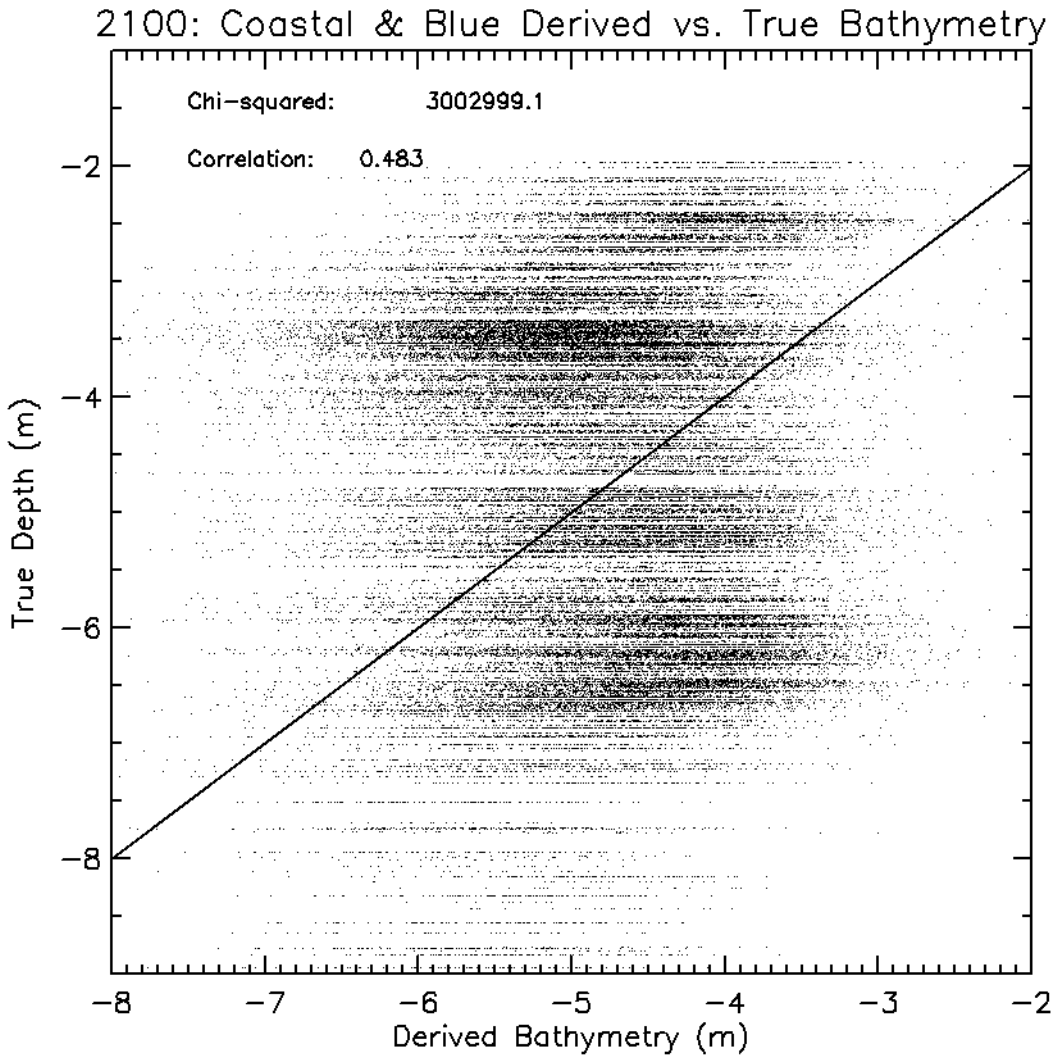

Figure 32. Coastal & Blue: Derived depth vs. "true" depth for Image 2100 (most nadir)

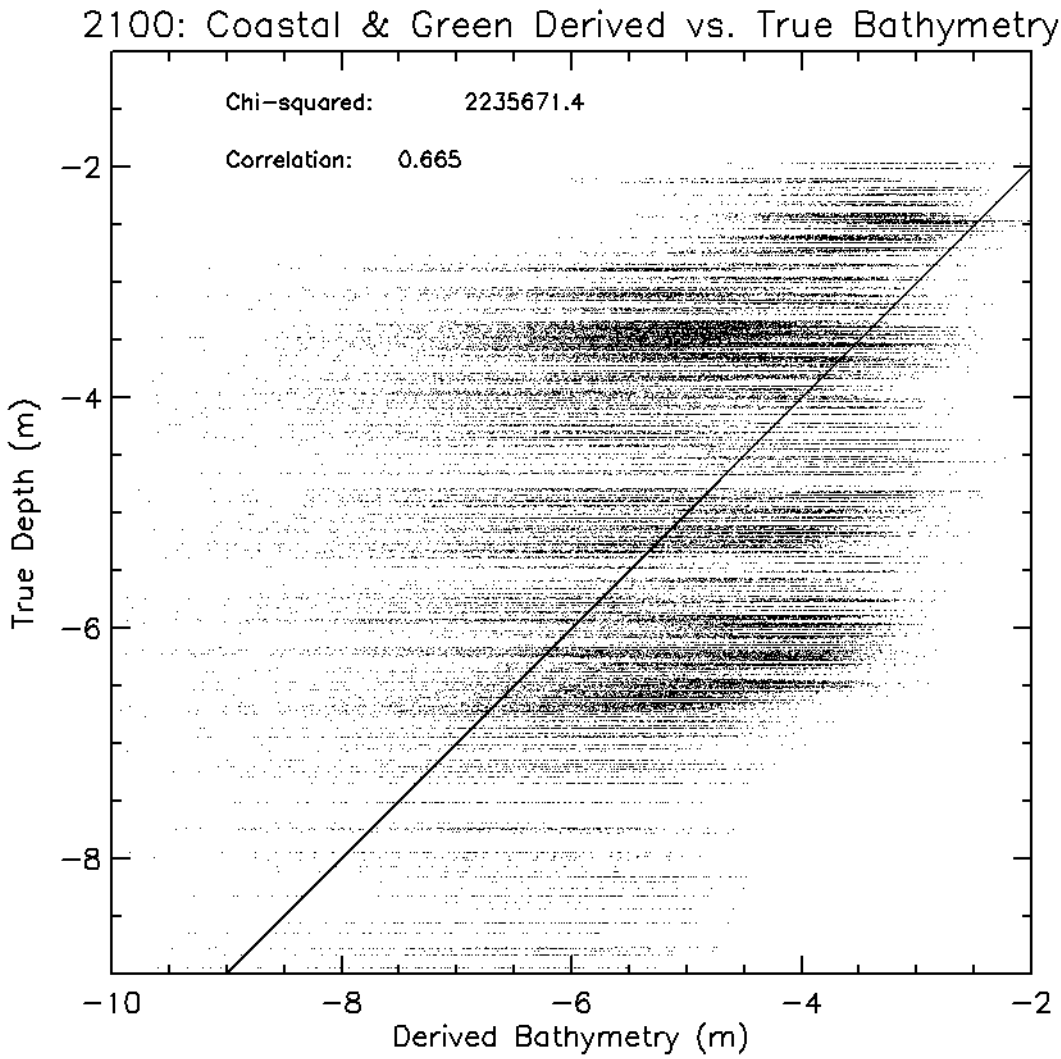

Figure 33. Coastal & Green: Derived depth vs. "true" depth for Image 2100 (most nadir)

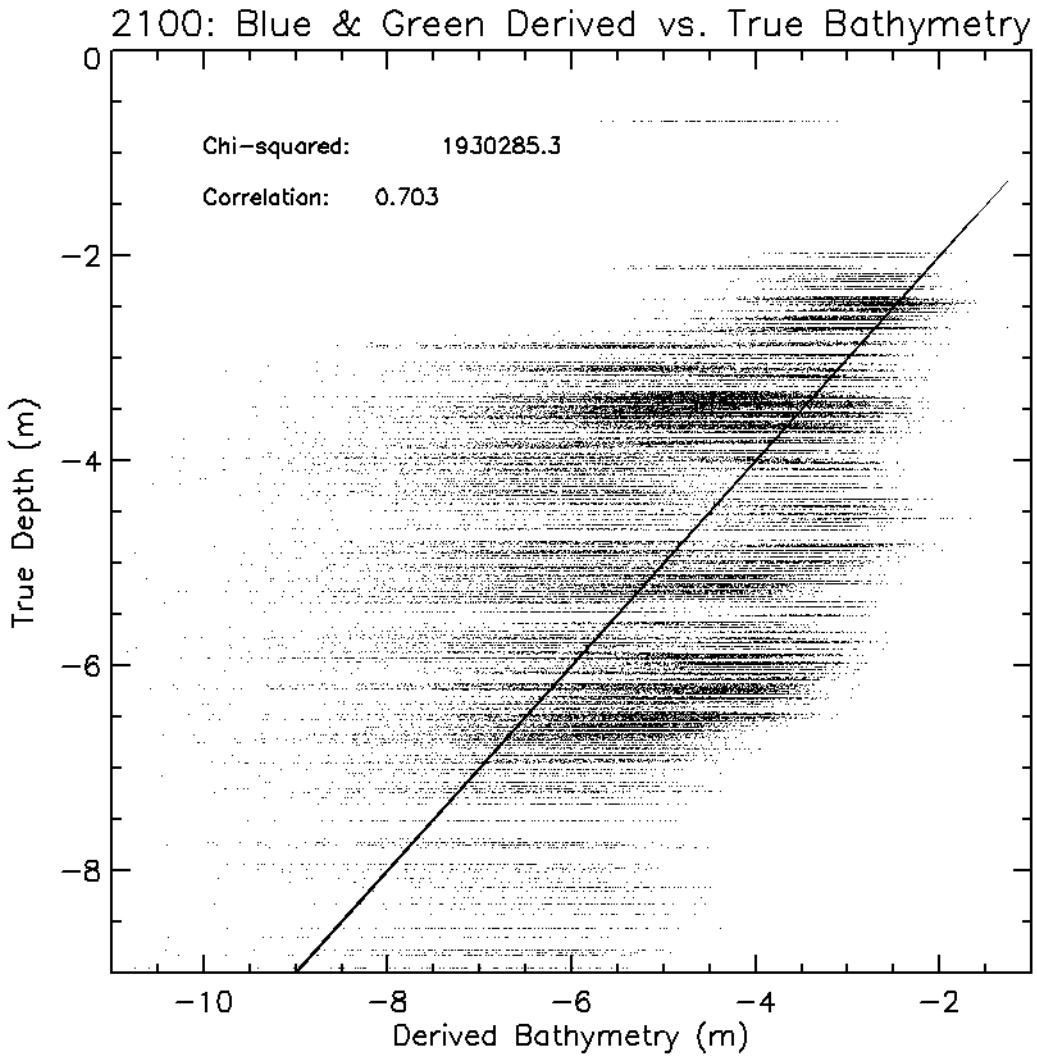

Figure 34. Blue & Green: Derived depth vs. "true" depth for Image 2100 (most nadir)

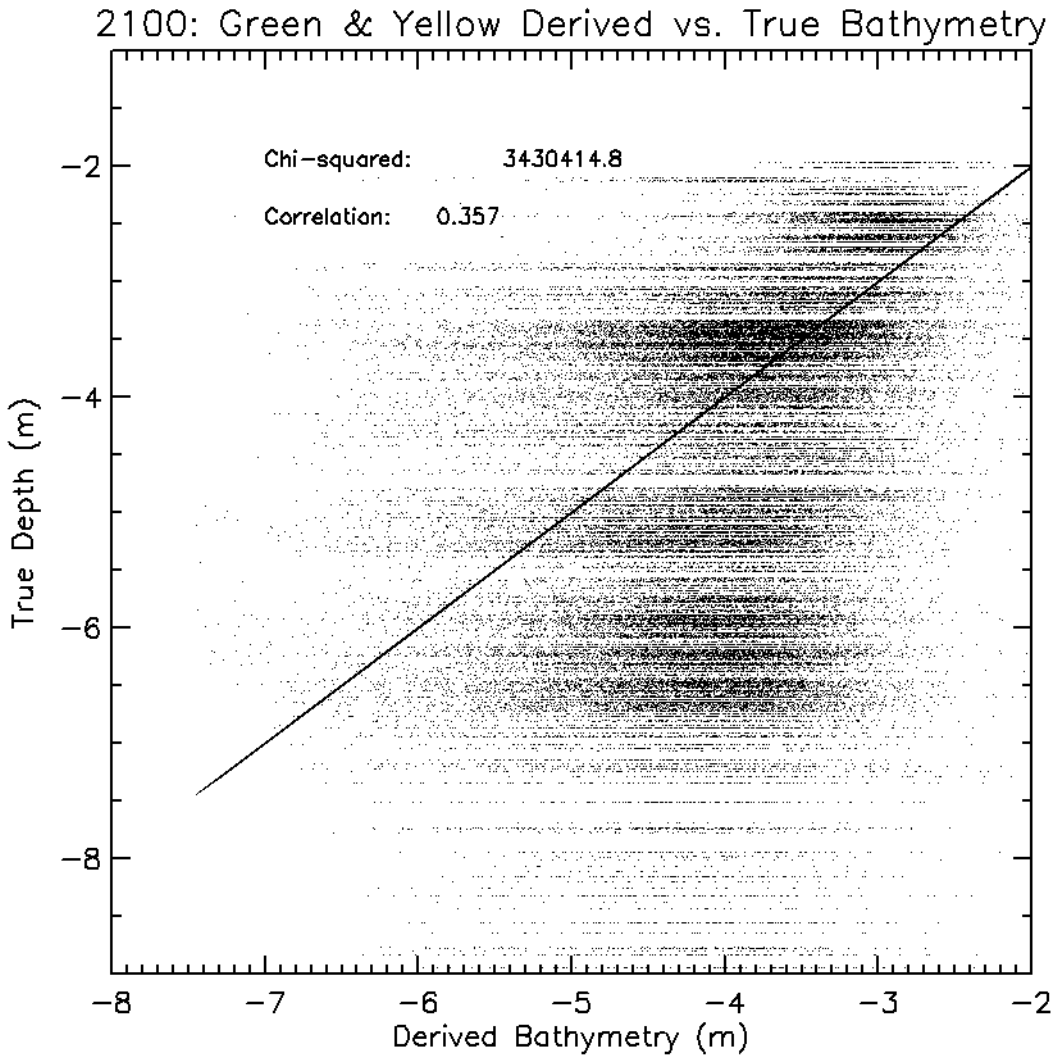

Figure 35. Green & Yellow: Derived depth vs. "true" depth for Image 2100 (most nadir)

Chi-squared and correlation values were calculated and plotted for each Image ID (view angle) for all four band combinations. These values represent the correlation of the depth derived from the band combination ratios versus the "true" depth (example values are shown in Section E of the Appendix). Results are depicted in Figures 36 through 39.

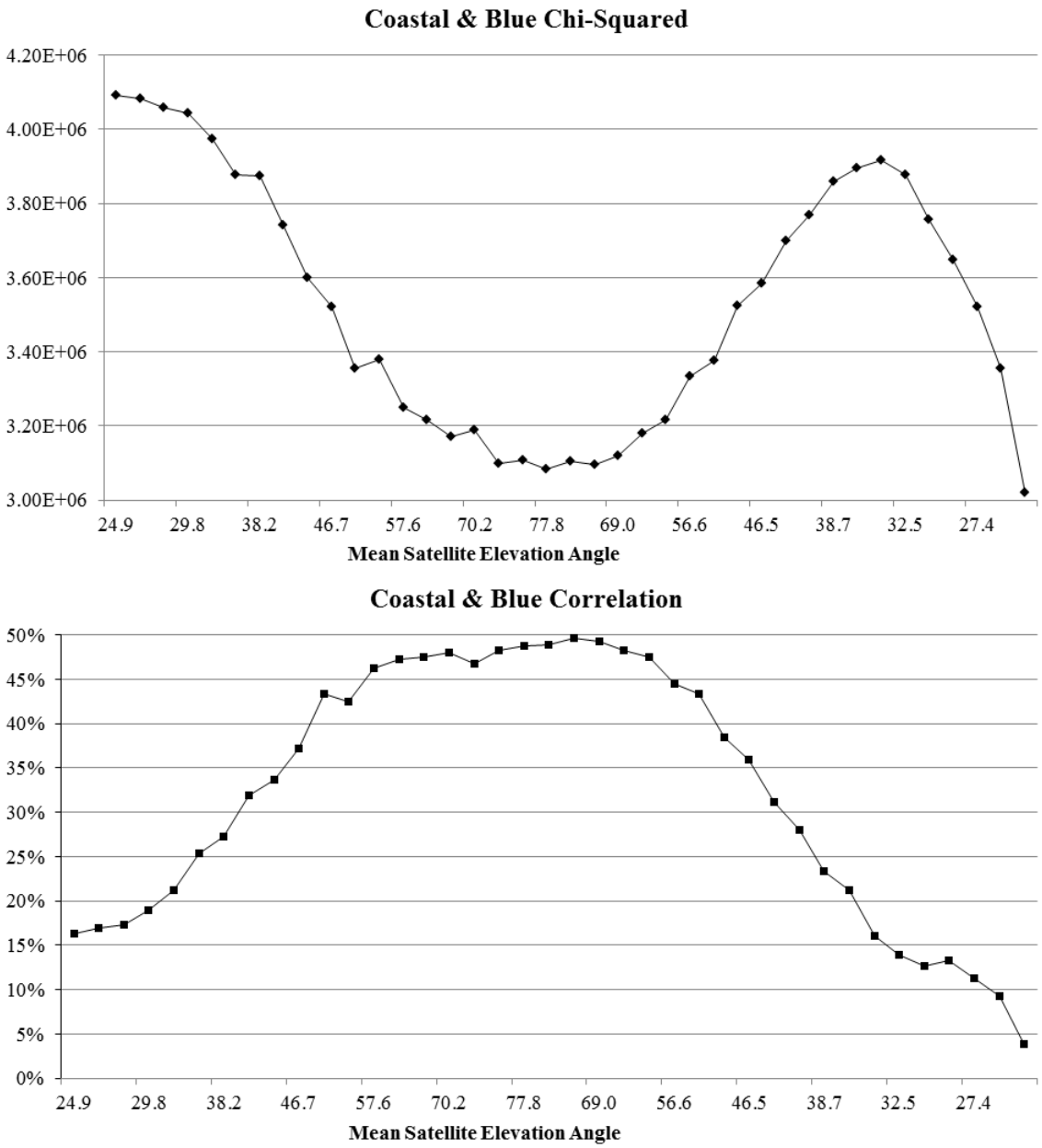

Figure 36. Coastal & Blue: Chi-squared (top) and correlation (bottom) values (y-axis) plotted against the mean satellite elevation angle (x-axis) for all 39 WV-2 images

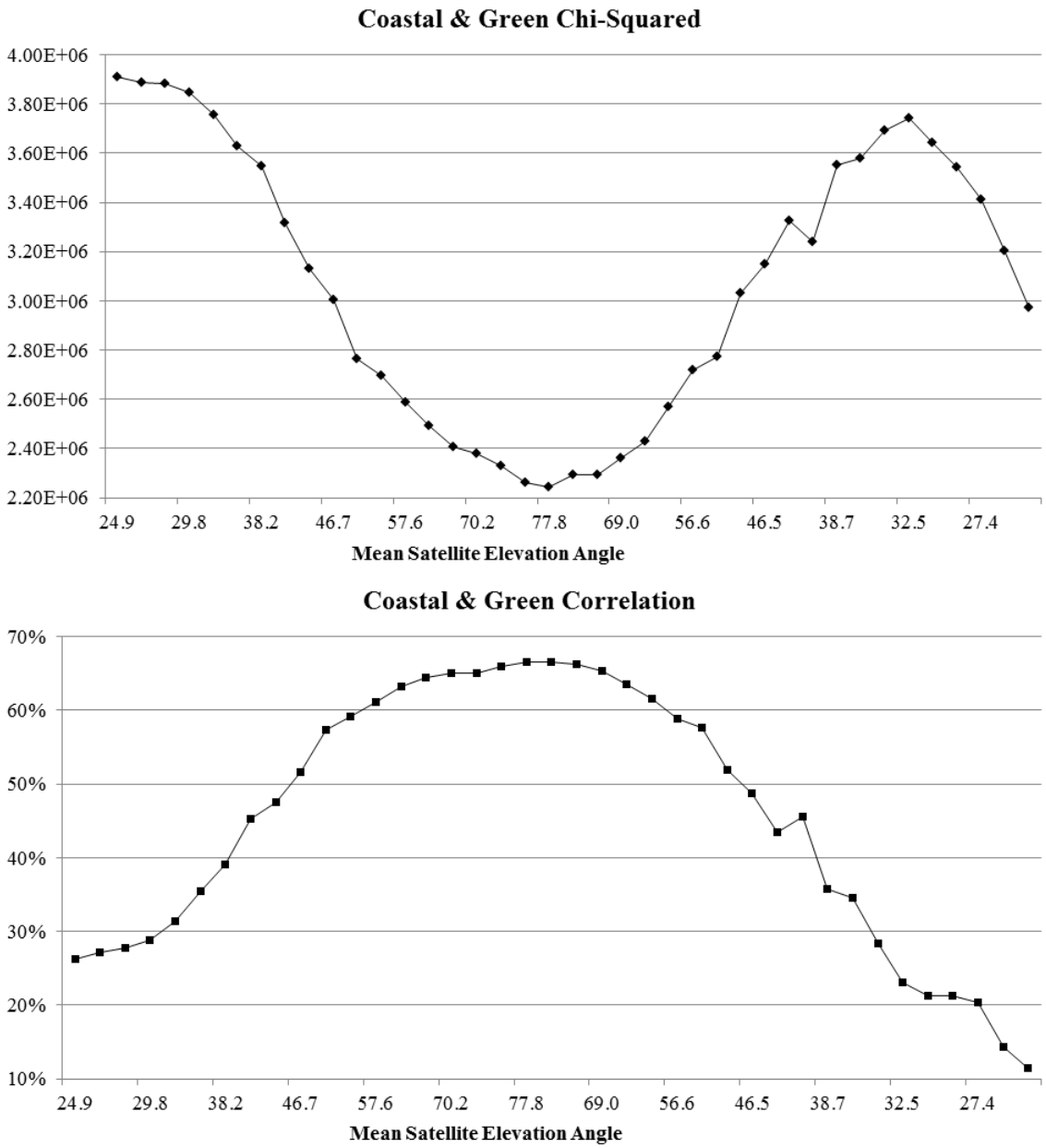

Figure 37. Coastal & Green: Chi-squared (top) and correlation (bottom) values (y-axis) plotted against the mean satellite elevation angle (x-axis) for all 39 WV-2 images

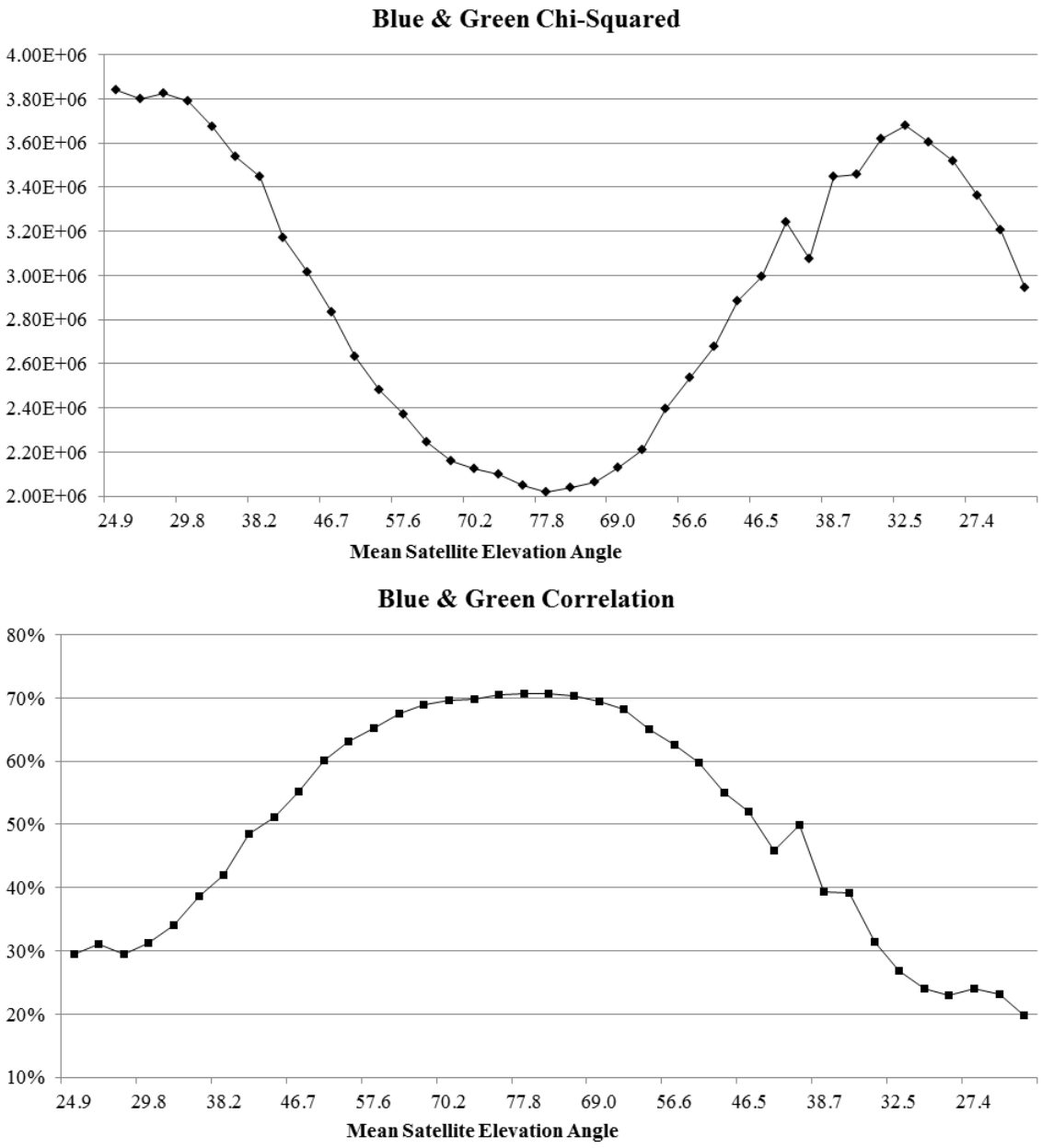

Figure 38. Blue & Green: Chi-squared (top) and correlation (bottom) values (y-axis) plotted against the mean satellite elevation angle (x-axis) for all 39 WV-2 images

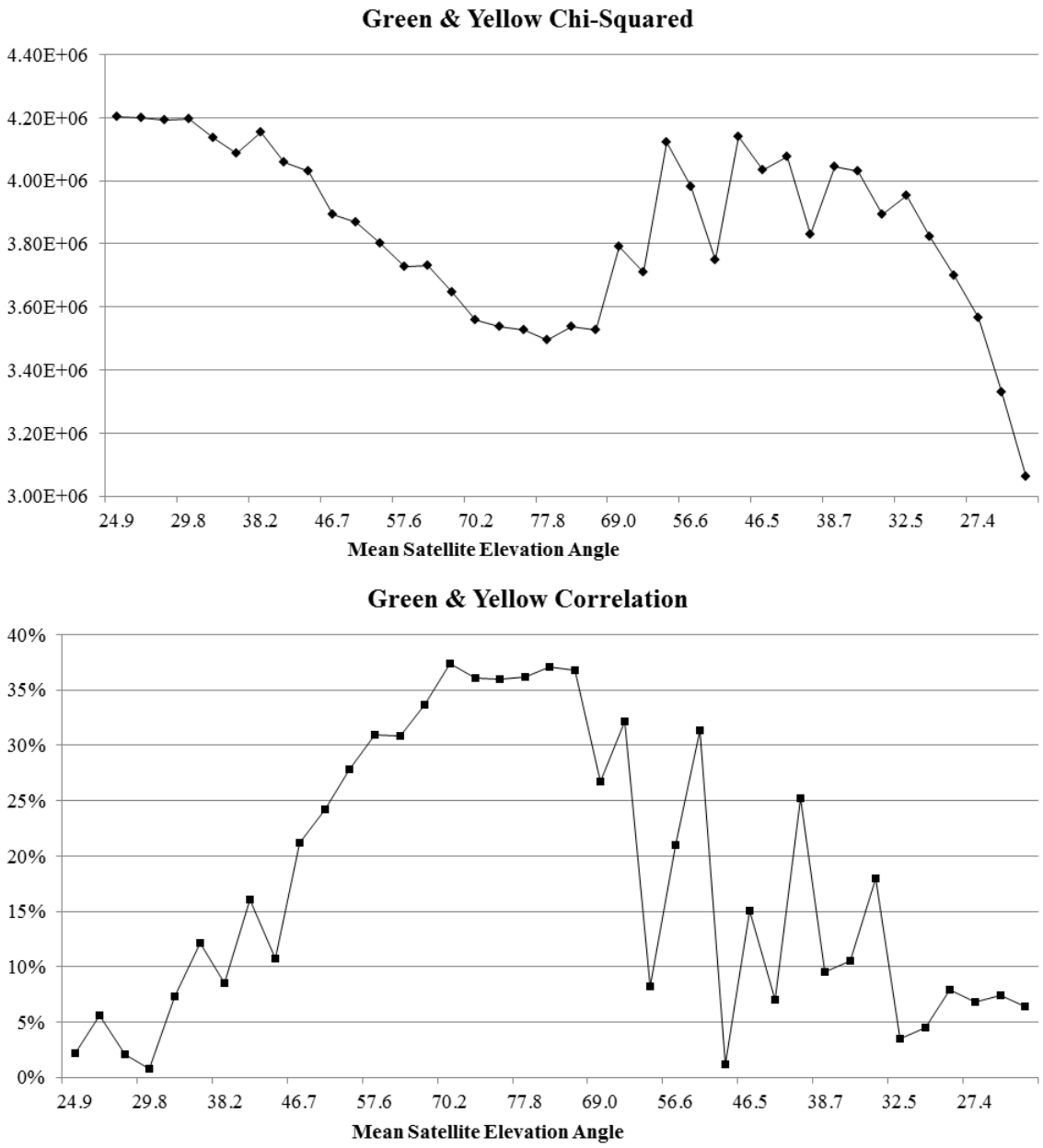

Figure 39. Green & Yellow: Chi-squared (top) and correlation (bottom) values (y-axis) plotted against the mean satellite elevation angle (x-axis) for all 39 WV-2 images

Although exact chi-squared and correlation values depend on the cutoff values used in the 2D scatter plots for each band combination (refer to Figure 23), the trend was the same after multiple runs. For all four band combinations, the images acquired closer to nadir had the lowest chi-squared values and the highest correlations. The optimal

values were found when running the Blue & Green code, with a correlation value around 71%. The most erratic results came from the Green & Yellow code. This may be because the Yellow band did not penetrate as deeply into the water.

Low chi-squared values are also seen from Image IDs 4050 to 4100. This is most likely due to the fact that clouds were entering the scene, being masked and, therefore, leaving very little water from which to collect spectral information for depth derivation.

THIS PAGE INTENTIONALLY LEFT BLANK

V. CONCLUSIONS

A. SUMMARY OF OBSERVATIONS AND ANALYSIS

Thirty-nine WV-2 images collected at multiple angles over a coastal, shallow water environment were used to analyze the effect of varying view angle on bathymetry derivation. Following initial data preparation steps, the entire dataset was analyzed to determine what effect, if any, acquisition angle has on nearshore depth retrieval. The data processing and analysis consisted of steps to remove sun glint, a band ratio method to determine relative depth, and a regression to find derived depth.

Accuracy of depth retrieval did, in fact, demonstrate an association with image acquisition angle. Images acquired at more off-nadir view angles proved to have lower correlation values to the actual "true" bathymetry data. This was shown by the increase in correlation values for more nadir images within the dataset, followed by a decrease as images became more backward-looking. Likewise, chi-squared values decreased as the code approached the nadir-looking images, and increased again after that.

Four band combinations were compared in an effort to determine which WV-2 bands might be best for determining depth in shallow, coastal environments. These included: Coastal & Blue, Coastal & Green, Blue & Green, and Green & Yellow. Of the four, the Blue & Green band combination performed best, with the highest correlation value of approximately 71% between "true" and derived depth.

The results of this research showed that more accurate bathymetric depths will be derived from images that have been acquired closer to nadir viewing geometry. Additionally, when using imagery from the WV-2 sensor, a combination of the Blue and Green bands will penetrate into the water in such a way that a higher accuracy of depth information will be obtained.

B. RECOMMENDATIONS AND FUTURE WORK

There are a number of factors that may have negatively affected the data and analysis. While the scene over Kailua Bay was chosen because it was the least cloudy

beach out of the 39 images in the dataset, it still had cloud cover (especially between Image IDs 4050 and 4100). This led to fewer data points that could be analyzed for those scenes. It would also have been preferable to have used a more recent dataset for "true" bathymetry. This particular collection is thought to have been acquired between 2002 and 2005, and in an environment as dynamic as a coastal shoreline, bathymetry could have changed significantly. In the future, it would be advantageous to find a recent bathymetric dataset, and then acquire WV-2 data over that geographic location.

There are a number of possibilities for improvement and growth in future research related to this particular topic. It would be beneficial to apply the analysis approach to the entire dataset scene, rather than just the image chips. It would also be interesting to use a dataset with a wider range of satellite elevation angles (more off-nadir to more nadir and back). It might also be fascinating to apply this method to nearshore areas with black sand to see whether or not sand color affects the results of the algorithm.

LIST OF REFERENCES

Avery, T. E., G. L. Berlin (1992), *Fundamentals of Remote Sensing and Airphoto Interpretation*, Macmillan Publishing Company, Maxwell Macmillan Canada, Maxwell Macmillan International, New York, Toronto, Oxford, Singapore, Sydney.

Camacho, M. A. (2006), Depth Analysis of Midway Atoll Using QuickBird Multi-Spectral Imaging over Variable Substrates, M.S. thesis, Naval Postgraduate School, Monterey, CA.

Clark, R. E. (2005), Naval Satellite Bathymetry: A Performance Assessment, M.S. thesis, Naval Postgraduate School, Monterey, CA.

Dickey, T. D., G. W. Kattawar, and K. J. Voss (2011), Shedding new light on light in the ocean, *Physics Today* (April), 44.

Eismann, M. T. (2012), *Hyperspectral Remote Sensing*, SPIE Press, Bellingham, WA.

Goodman, J. A., Z. Lee, and S. L. Ustin (2008), Influence of Atmospheric and Sea-Surface Corrections on Retrieval of Bottom Depth and Reflectance Using a Semi-Analytical Model: A Case Study in Kaneohe Bay, Hawaii, *Applied Optics, 47*, F1.

Hedley, J. D., A. R. Harborne, and P. J. Mumby (2005), Simple and robust removal of sun glint for mapping shallow-water benthos, *Int. J. Remote Sens., 26*(10), 2107.

Hochberg, E. J., S. Andrefouet, and M. R. Tyler (2003), Sea Surface Correction of High Spatial Resolution Ikonos Images to Improve Bottom Mapping in Near-Shore Environments, *IEEE Trans. Geosci. Remote Sens., 41*, 1724.

Isoun, E., C. H. Fletcher, N. Frazer, and J. Gradie (2003), Multi-spectral mapping of reef bathymetry and coral cover; Kailua Bay, Hawaii, *Coral Reefs, 22*, 68, doi:10.1007/s00338-003-0287-4.

Jensen, J. R. (2007), *Remote Sensing of the Environment: An Earth Resource Perspective*, vol. 2, Prentice Hall, Upper Saddle River, NJ.

Kay, S., J. D. Hedley, and S. Lavender (2009), Sun Glint Correction of High and Low Spatial Resolution Images of Aquatic Scenes: a Review of Methods for Visible and Near-Infrared Wavelengths, *Remote Sensing, 1*(4), 697.

Longbotham, N., C. Bleiler, C. Chaapel, C. Padwick, W. Emery, and F. Pacifici (2011), Spatial Classification of WorldView-2 Multi-angle Sequence, paper presented at Joint Urban Remote Sensing Event, Munich, Germany.

Longbotham, N., C. Bleiler, C. Chaapel, C. Padwick, W. Emery, and F. Pacifici (2011), Spectral Classification of WorldView-2 Multi-angle Sequence, paper presented at Joint Urban Remote Sensing Event, Munich, Germany.

Longbotham, N., C. Chaapel, L. Bleiler, C. Padwick, W. J. Emery, and F. Pacifici (2011), Very High Resolution Multiangle Urban Classification Analysis, *IEEE TRANSACTIONS ON GEOSCIENCE AND REMOTE SENSING*(99), 1, doi:10.1109/TGRS.2011.2165548.

Loomis, M. J. (2009), Depth Derivation from the WorldView-2 Satellite Using Hyperspectral Imagery, M.S. thesis, Naval Postgraduate School, Monterey, CA.

Lyzenga, D. R. (1978), Passive remote sensing techniques for mapping water depth and bottom features, *Applied Optics, 17*(3), 379, doi:10.1364/AO.17.000379.

Lyzenga, D. R., N. P. Malinas, and F. J. Tanis (2006), Multispectral Bathymetry Using a Simple Physically Based Algorithm, *IEEE Trans. Geosci. Remote Sens., 44*, 2251.

Madden, C. K. (2011), Contributions to Remote Sensing of Shallow Water Depth with the Worldview-2 Yellow Band, M.S. thesis, Naval Postgraduate School, Monterey, CA.

Mancini, S. (2012), Automating Nearshore Bathymetry Extraction from Wave Motion in Satellite Optical Imagery, M.S. thesis, Naval Postgraduate School, Monterey, CA.

Marchisio, G., F. Pacifici, and C. Padwick (2011), Coastal applications of WorldView-2 high resolution multi-spectral imagery, paper presented at American Society for Photogrammetry and Remote Sensing, Milwaukee, WI USA.

Maritorena, S., A. Morel, and B. Gentili (1994), Diffuse reflectance of oceanic shallow waters: Influence of water depth and bottom albedo, *Limnol. Oceanogr., 39*(7), 1689.

Martin, S. (2004), *An Introduction to Ocean Remote Sensing*, Cambridge University Press, Cambridge, UK.

McCarthy, B. L. (2010), Coastal Bathymetry Using 8-Color Multispectral Satellite Observation of Wave Motion, M.S. thesis, Naval Postgraduate School, Monterey, CA.

McConnon, C. L. (2010), High Spatial Resolution Bidirectional Reflectance Retrieval Using Satellite Data, M.S. thesis, Naval Postgraduate School, Monterey, CA.

Mobley, C. D. (1994), *Light and Water: Radiative Transfer in Natural Waters*, Academic Press, San Diego, CA USA.

Myrick, K. B. (2011), Coastal Bathymetry Using Satellite Observation in Support of Intelligence Preparation of the Environment, M.S. thesis, Naval Postgraduate School, Monterey, CA.

Olsen, R. C. (2007), *Remote Sensing from Air and Space*, SPIE Press, Bellingham, Washington.

Pacifici, F., J. Chanussot, and Q. Du, 2011: 2011 GRSS Data Fusion Contest: Exploiting WorldView-2 Multi-Angular Acquisitions.

Pacifici, F., K. Navular, 2011: Very High Spatial Resolution Imagery for Urban Application. [Available online at http://www.earthzine.org/2011/06/27/very-high-spatial-resolution-imagery-for-urban-applications/].

Research Systems, I. (2004), ENVI Tutorials, Boulder, CO: Research Systems, Inc.

Sanford, T. B., K. A. Kelly, and D. M. Farmer (2011), Sensing the ocean, *Physics Today* (February), 24.

Smith, R. C., K. S. Baker (1981), Optical properties of the clearest natural waters, *Applied Optics, 20*(2), 177.

Stumpf, R. P., K. Holderied, and M. Sinclair (2003), Determination of water depth with high-resolution satellite imagery over variable bottom types, *Limnol. Oceanogr., 48*(1, part 2), 547.

Sturm, B. (1981), The atmospheric correction of remotely sensed data and the quantitative determination of suspended matter in marine water surface layers in *Remote Sensing in Meteorology, Oceanography and Hydrology*, edited by A. P. Cracknell, ed. (Ellis Horwood, Chichester, UK, 1980), pp. 163–197.

Thomas, G. E., K. Stamnes (1999), *Radiative Transfer in the Atmosphere and Ocean*, Cambridge University Press, Cambridge, UK.

Updike, T., C. Comp (2010), Radiometric Use of WorldView-2 Imagery, technical note, rev. 1.0, DigitalGlobe, Inc., Longmont, CO.

THIS PAGE INTENTIONALLY LEFT BLANK

APPENDIX: CHARTS AND GRAPHS

A. EXAMPLE WORLDVIEW-2 METADATA FILE (FOR IMAGE 1010)

```
version = "23.6";
generationTime = 2011-08-01T01:59:55.000000Z;
productOrderId = "052564471010_01_P001";
productCatalogId = "202001008362B200";
imageDescriptor = "Basic1B";
bandId = "Multi";
panSharpenAlgorithm = "None";
numRows = 3072;
numColumns = 9216;
productLevel = "LV1B";
productType = "Basic";
numberOfLooks = 1;
radiometricLevel = "Corrected";
bitsPerPixel = 16;
compressionType = "JPEG2000";
jpegProfileName = "nga_npje_pan_nl";
BEGIN_GROUP = BAND_C
      ULLon = -157.86756401;
      ULLat =   21.36508648;
      ULHAE =   275.36;
      URLon = -157.49196245;
      URLat =   21.69660890;
      URHAE =     9.00;
      LRLon = -157.49051787;
      LRLat =   21.56876101;
      LRHAE =    11.00;
      LLLon = -157.87041130;
      LLLat =   21.22582540;
      LLHAE =    15.00;
      absCalFactor = 9.295654e-03;
      effectiveBandwidth = 4.730000e-02;
      TDILevel = 24;
END_GROUP = BAND_C
BEGIN_GROUP = BAND_B
      ULLon = -157.86756401;
      ULLat =   21.36508648;
      ULHAE =   275.36;
      URLon = -157.49196245;
      URLat =   21.69660890;
      URHAE =     9.00;
      LRLon = -157.49051787;
      LRLat =   21.56876101;
      LRHAE =    11.00;
      LLLon = -157.87041130;
      LLLat =   21.22582540;
```

```
      LLHAE =    15.00;
      absCalFactor = 1.783568e-02;
      effectiveBandwidth = 5.430000e-02;
      TDILevel = 10;
END_GROUP = BAND_B
BEGIN_GROUP = BAND_G
      ULLon = -157.86756401;
      ULLat =   21.36508648;
      ULHAE =   275.36;
      URLon = -157.49196245;
      URLat =   21.69660890;
      URHAE =     9.00;
      LRLon = -157.49051787;
      LRLat =   21.56876101;
      LRHAE =    11.00;
      LLLon = -157.87041130;
      LLLat =   21.22582540;
      LLHAE =    15.00;
      absCalFactor = 1.364197e-02;
      effectiveBandwidth = 6.300000e-02;
      TDILevel = 10;
END_GROUP = BAND_G
BEGIN_GROUP = BAND_Y
      ULLon = -157.86756401;
      ULLat =   21.36508648;
      ULHAE =   275.36;
      URLon = -157.49196245;
      URLat =   21.69660890;
      URHAE =     9.00;
      LRLon = -157.49051787;
      LRLat =   21.56876101;
      LRHAE =    11.00;
      LLLon = -157.87041130;
      LLLat =   21.22582540;
      LLHAE =    15.00;
      absCalFactor = 6.810718e-03;
      effectiveBandwidth = 3.740000e-02;
      TDILevel = 18;
END_GROUP = BAND_Y
BEGIN_GROUP = BAND_R
      ULLon = -157.86756401;
      ULLat =   21.36508648;
      ULHAE =   275.36;
      URLon = -157.49196245;
      URLat =   21.69660890;
      URHAE =     9.00;
      LRLon = -157.49051787;
      LRLat =   21.56876101;
      LRHAE =    11.00;
      LLLon = -157.87041130;
```

```
      LLLat =   21.22582540;
      LLHAE =    15.00;
      absCalFactor = 1.851735e-02;
      effectiveBandwidth = 5.740000e-02;
      TDILevel = 6;
END_GROUP = BAND_R
BEGIN_GROUP = BAND_RE
      ULLon = -157.86756401;
      ULLat =   21.36508648;
      ULHAE =   275.36;
      URLon = -157.49196245;
      URLat =   21.69660890;
      URHAE =     9.00;
      LRLon = -157.49051787;
      LRLat =   21.56876101;
      LRHAE =    11.00;
      LLLon = -157.87041130;
      LLLat =   21.22582540;
      LLHAE =    15.00;
      absCalFactor = 6.063145e-03;
      effectiveBandwidth = 3.930000e-02;
      TDILevel = 18;
END_GROUP = BAND_RE
BEGIN_GROUP = BAND_N
      ULLon = -157.86756401;
      ULLat =   21.36508648;
      ULHAE =   275.36;
      URLon = -157.49196245;
      URLat =   21.69660890;
      URHAE =     9.00;
      LRLon = -157.49051787;
      LRLat =   21.56876101;
      LRHAE =    11.00;
      LLLon = -157.87041130;
      LLLat =   21.22582540;
      LLHAE =    15.00;
      absCalFactor = 2.050828e-02;
      effectiveBandwidth = 9.890000e-02;
      TDILevel = 6;
END_GROUP = BAND_N
BEGIN_GROUP = BAND_N2
      ULLon = -157.86756401;
      ULLat =   21.36508648;
      ULHAE =   275.36;
      URLon = -157.49196245;
      URLat =   21.69660890;
      URHAE =     9.00;
      LRLon = -157.49051787;
      LRLat =   21.56876101;
      LRHAE =    11.00;
```

```
      LLLon = -157.87041130;
      LLLat =   21.22582540;
      LLHAE =    15.00;
      absCalFactor = 9.042234e-03;
      effectiveBandwidth = 9.960000e-02;
      TDILevel = 24;
END_GROUP = BAND_N2
outputFormat = "NITF21NCDRD";
BEGIN_GROUP = IMAGE_1
      satId = "WV02";
      mode = "FullSwath";
      scanDirection = "Forward";
      CatId = "103001000DC52200";
      TLCTime = 2011-07-30T21:22:48.765050Z;
      numTLC = 2;
      TLCList = (
      (0,  0.000000),
      (2055,  0.411000)     );
      firstLineTime = 2011-07-30T21:22:48.765050Z;
      avgLineRate = 5000.00;
      exposureDuration = 0.0002;
      minCollectedRowGSD =   7.002;
      maxCollectedRowGSD =   7.136;
      meanCollectedRowGSD =   7.069;
      minCollectedColGSD =   6.088;
      maxCollectedColGSD =   6.168;
      meanCollectedColGSD =   6.128;
      meanCollectedGSD =   6.582;
      meanProductRowGSD =   7.110;
      meanProductColGSD =   6.162;
      meanProductGSD =   6.619;
      rowUncertainty =  294.50;
      colUncertainty =  145.97;
      minSunAz =  96.0;
      maxSunAz =  96.4;
      meanSunAz =  96.2;
      minSunEl =  72.3;
      maxSunEl =  72.3;
      meanSunEl =  72.3;
      minSatAz =  18.8;
      maxSatAz =  18.8;
      meanSatAz =  18.8;
      minSatEl =  24.9;
      maxSatEl =  25.0;
      meanSatEl =  24.9;
      minInTrackViewAngle =  52.7;
      maxInTrackViewAngle =  52.9;
      meanInTrackViewAngle =  52.8;
      minCrossTrackViewAngle =  14.3;
      maxCrossTrackViewAngle =  14.4;
```

```
      meanCrossTrackViewAngle =  14.4;
      minOffNadirViewAngle =  54.1;
      maxOffNadirViewAngle =  54.1;
      meanOffNadirViewAngle =  54.1;
      PNIIRS = 1.3;
      cloudCover = 0.311;
      resamplingKernel = "CC";
      positionKnowledgeSrc = "R";
      attitudeKnowledgeSrc = "R";
      revNumber = 9481;
END_GROUP = IMAGE_1
END;
```

B. INFORMATION ABOUT THE 39 WORLDVIEW-2 IMAGES – IMAGE ID, ACQUISITION TIME, SENSOR ELEVATION, SENSOR AZIMUTH, OFF NADIR VIEW ANGLE, AZIMUTH, AND ZENITH

Image ID	firstLineTime (Z)	meanSatEl	meanSatAz	meanOffNadirViewAngle	Azimuth	Zenith
1010	21:22:49	24.9	18.8	54.1	-161.2	125.9
1020	21:22:58	26.5	19.2	53.1	-160.8	126.9
1030	21:23:07	28.1	19.6	52.0	-160.4	128.0
1040	21:23:16	29.8	20.1	50.8	-159.9	129.2
1050	21:23:25	31.7	20.6	49.5	-159.4	130.5
1060	21:23:34	33.7	21.2	48.0	-158.8	132.0
1080	21:23:53	38.2	22.6	44.6	-157.4	135.4
1090	21:24:02	40.8	23.5	42.6	-156.5	137.4
1100	21:24:12	43.7	24.6	40.3	-155.4	139.7
2010	21:24:21	46.7	26.0	37.8	-154.0	142.2
2020	21:24:31	50.1	27.6	35.1	-152.4	144.9
2030	21:24:41	53.6	29.7	32.1	-150.3	147.9
2040	21:24:51	57.6	32.4	28.7	-147.6	151.3
2050	21:25:01	61.6	36.1	25.2	-143.9	154.8
2060	21:25:12	66.0	41.5	21.4	-138.5	158.6
2070	21:25:22	70.2	49.2	17.4	-130.8	162.3
2080	21:25:32	74.0	61.2	14.3	-118.8	165.7
2090	21:25:42	76.9	80.1	11.7	-99.9	168.3
2100	21:25:52	77.8	105.5	10.9	-74.5	169.1
3010	21:26:02	76.3	129.8	12.1	-50.2	167.9
3020	21:26:12	73.1	146.9	15.0	-33.1	165.0
3030	21:26:23	69.0	157.9	18.6	-22.1	161.4

Image ID	firstLineTime (Z)	meanSatEl	meanSatAz	meanOffNadirViewAngle	Azimuth	Zenith
3040	21:26:33	64.8	164.7	22.2	-15.3	157.8
3050	21:26:43	60.6	169.4	25.9	-10.6	154.1
3060	21:26:53	56.6	172.8	29.2	-7.2	150.8
3070	21:27:02	52.9	175.3	32.4	-4.7	147.6
3080	21:27:12	49.6	177.2	35.2	-2.8	144.8
3090	21:27:21	46.5	178.7	37.8	-1.3	142.2
3100	21:27:30	43.7	179.9	40.0	-0.1	140.0
4010	21:27:39	41.1	180.9	42.2	0.9	137.8
4020	21:27:47	38.7	181.7	44.0	1.7	136.0
4030	21:27:56	36.5	182.5	45.7	2.5	134.3
4040	21:28:04	34.4	183.1	47.3	3.1	132.7
4050	21:28:13	32.5	183.7	48.7	3.7	131.3
4060	21:28:21	30.7	184.2	50.0	4.2	130.0
4070	21:28:29	29.0	184.6	51.2	4.6	128.8
4080	21:28:38	27.4	185.0	52.3	5.0	127.7
4090	21:28:46	25.9	185.4	53.3	5.4	126.7
4100	21:28:54	24.5	185.7	54.2	5.7	125.8

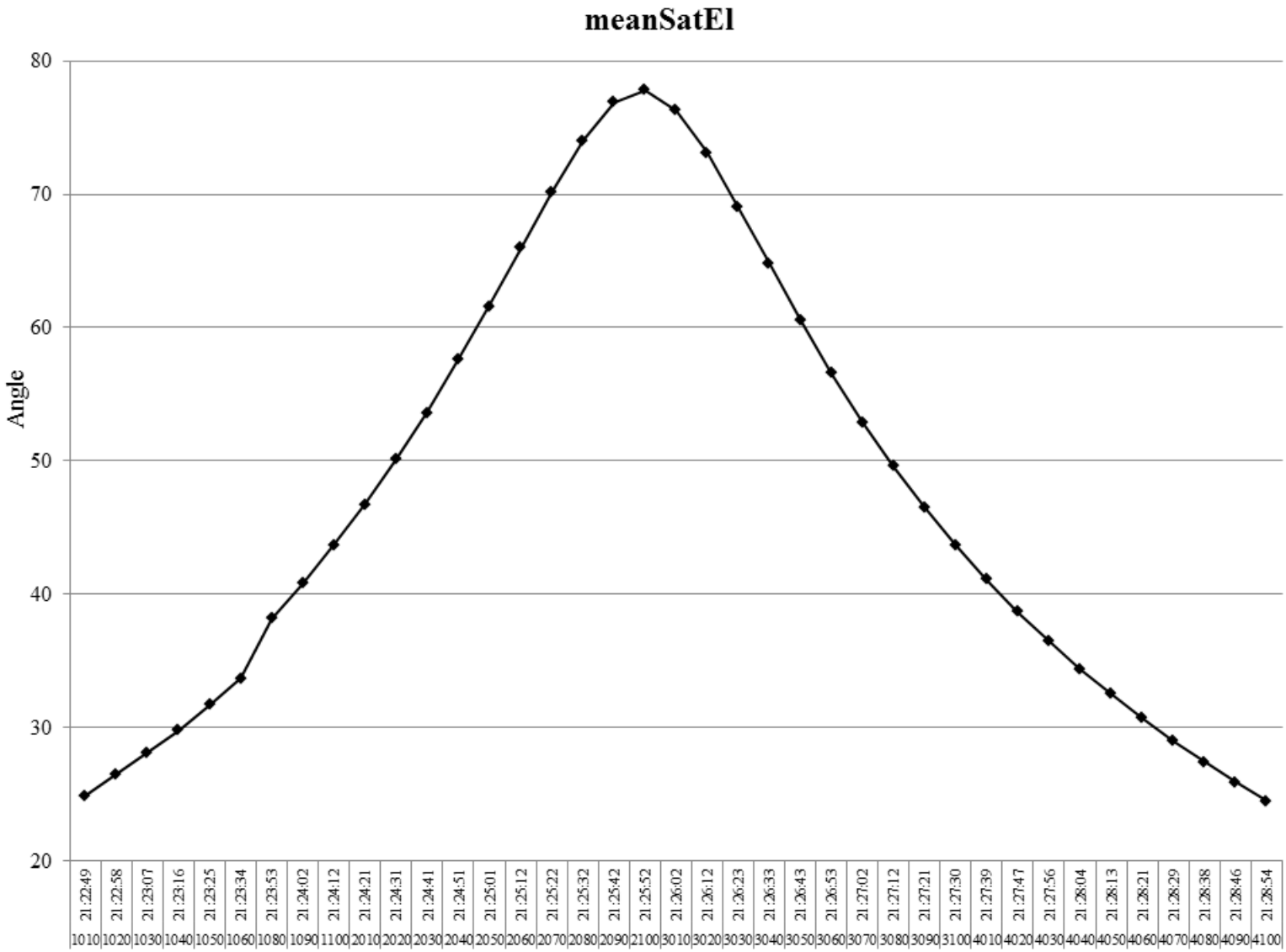
meanSatEl
Angle
80
70
60
50
40
30
20
21:22:49 1010
21:22:58 1020
21:23:07 1030
21:23:16 1040
21:23:25 1050
21:23:34 1060
21:23:53 1080
21:24:02 1090
21:24:12 1100
21:24:21 2010
21:24:31 2020
21:24:41 2030
21:24:51 2040
21:25:01 2050
21:25:12 2060
21:25:22 2070
21:25:32 2080
21:25:42 2090
21:25:52 2100
21:26:02 3010
21:26:12 3020
21:26:23 3030
21:26:33 3040
21:26:43 3050
21:26:53 3060
21:27:02 3070
21:27:12 3080
21:27:21 3090
21:27:30 3100
21:27:39 4010
21:27:47 4020
21:27:56 4030
21:28:04 4040
21:28:13 4050
21:28:21 4060
21:28:29 4070
21:28:38 4080
21:28:46 4090
21:28:54 4100

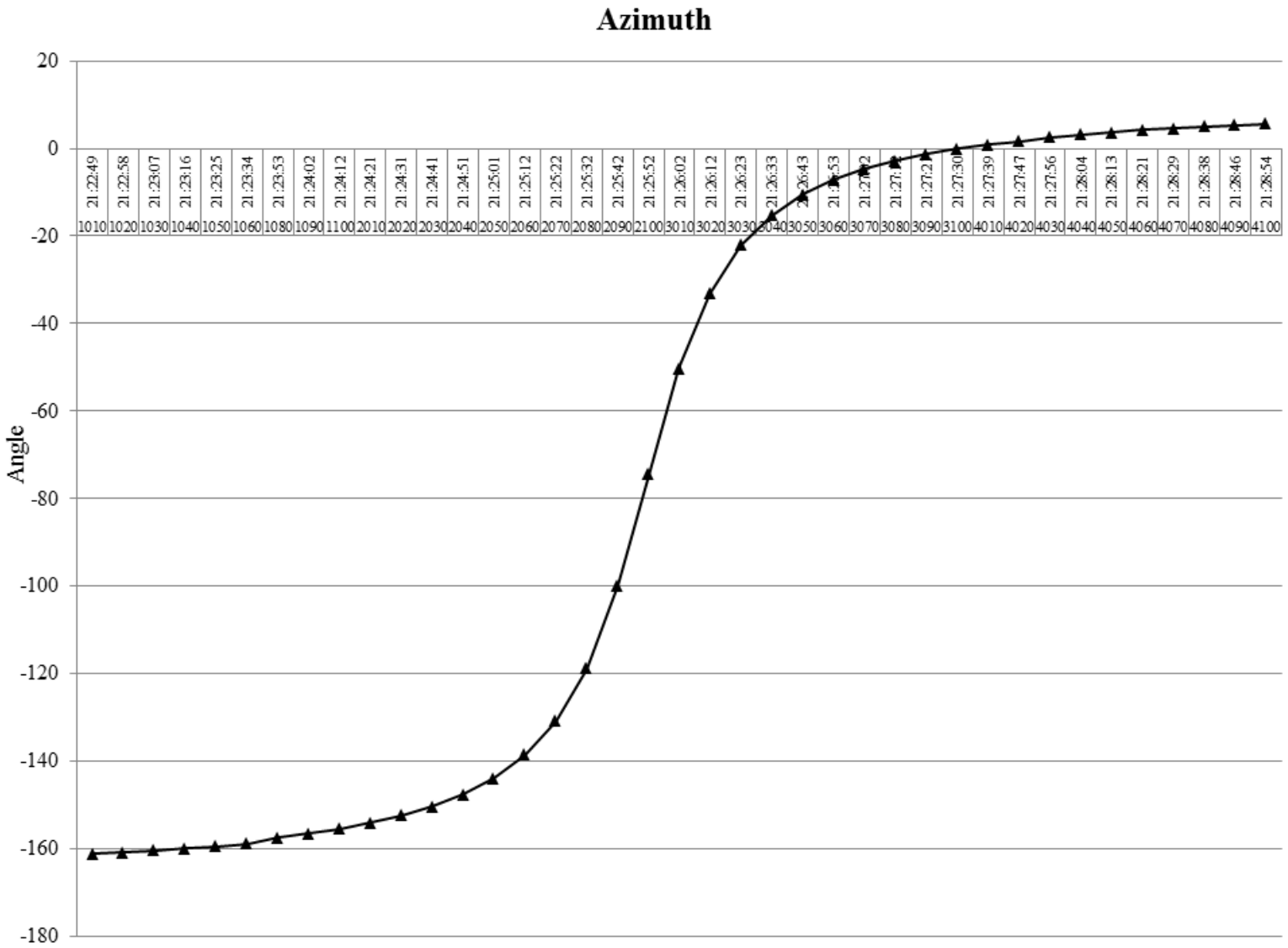
Azimuth
Angle
20
0
-20
-40
-60
-80
-100
-120
-140
-160
-180
21:22:49 1010
21:22:58 1020
21:23:07 1030
21:23:16 1040
21:23:25 1050
21:23:34 1060
21:23:53 1080
21:24:02 1090
21:24:12 1100
21:24:21 2010
21:24:31 2020
21:24:41 2030
21:24:51 2040
21:25:01 2050
21:25:12 2060
21:25:22 2070
21:25:32 2080
21:25:42 2090
21:25:52 2100
21:26:02 3010
21:26:12 3020
21:26:23 3030
21:26:33 3040
21:27:21 3090
21:27:30 3100
21:27:39 4010
21:27:47 4020
21:27:56 4030
21:28:04 4040
21:28:13 4050
21:28:21 4060
21:28:29 4070
21:28:38 4080
21:28:46 4090
21:28:54 4100

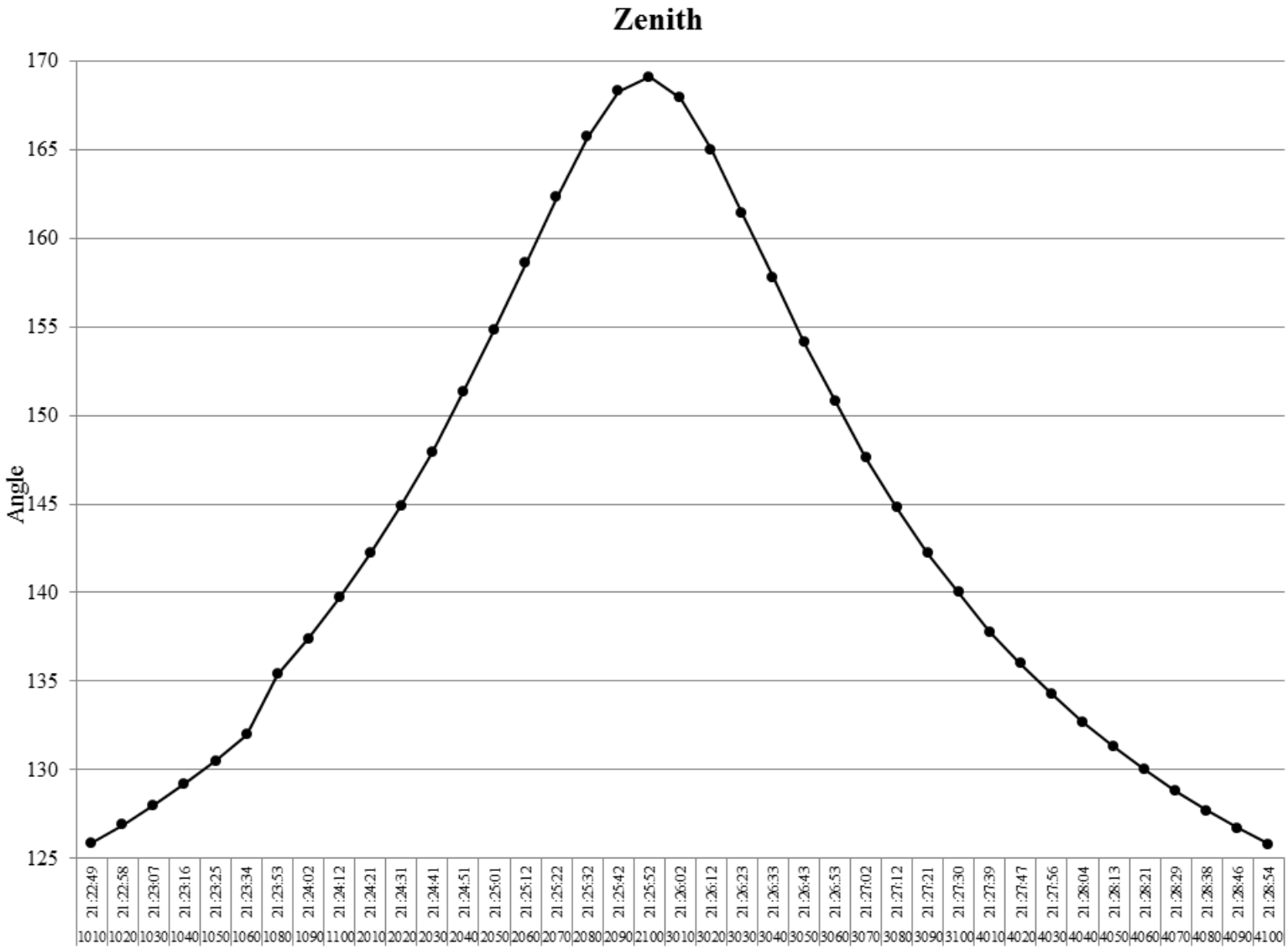
Zenith
Angle
170
165
160
155
150
145
140
135
130
125
21:22:49 1010
21:22:58 1020
21:23:07 1030
21:23:16 1040
21:23:25 1050
21:23:34 1060
21:23:53 1080
21:24:02 1090
21:24:12 1100
21:24:21 2010
21:24:31 2020
21:24:41 2030
21:24:51 2040
21:25:01 2050
21:25:12 2060
21:25:22 2070
21:25:32 2080
21:25:42 2090
21:25:52 2100
21:26:02 3010
21:26:12 3020
21:26:23 3030
21:26:33 3040
21:26:43 3050
21:26:53 3060
21:27:02 3070
21:27:12 3080
21:27:21 3090
21:27:30 3100
21:27:39 4010
21:27:47 4020
21:27:56 4030
21:28:04 4040
21:28:13 4050
21:28:21 4060
21:28:29 4070
21:28:38 4080
21:28:46 4090
21:28:54 4100

C. IDL CODE FOR MOST HIGHLY CORRELATED BAND COMBINATION (BLUE & GREEN)

```
;Final code for Krista Lee's September 2012 thesis
;Code written by: Krista Lee, Angie Kim, Professor Olsen
;
;Blue vs. Green
;
;The purpose of this code is to take 39 image chips over Kailua Bay, Oahu, HI from 30 July 2011 and apply a
deglinting process,
;along with a band ratio method to determine water depth.  The images, acquired at different angles, have
alreaad been calibrated
;for radiance, atmospherically corrected, and registered to the most nadir of the images.  This code will
then apply a simple
;deglinting technique to remove the effects of sun glint, as well as use Stumpf et al.'s band ratio method
for bathymetry derivation.
;These depth values will be compared to actual lidar bathymetry data from the University of Hawaii.

;*******************************************************
;LOAD COLOR TABLE
loadct, 13   ;Loads color table -- Rainbow
  tvlct, r, g, b, /get
  r(255) = 255
  g(255) = 255
  b(255) = 255
  tvlct, r, g, b
  device, decomposed = 0, retain = 1

;*******************************************************
;DEFINE DIRECTORY
dir = 'O:\Krista_Lee\Thesis\IDL\FINAL'
cd, dir

;*******************************************************
;DEFINE FILES
files = FILE_SEARCH('*_mosaic_wgs84_rad_resize*chip.dat')
nfiles = n_elements(files)
print, string(nfiles) + ' files found: '
```

```
print, files

fmask = '2100_mask_b.dat'   ;Created specifically for this image chip in ENVI

;Size of images
samples = 995L
lines = 999L
bands = 8

;FOR LOOP TO REPEAT PROCESS FOR EACH IMAGE
for file_number = 0, nfiles - 1 do begin   ;Loops through each elements in file array

file = files(file_number)
out_dir = 'Image_' + strmid(file, 0, 4)
spawn, 'mkdir ' + out_dir   ;This creates the folder for the WV-2 image
cd, out_dir
spawn, 'mkdir b_g'   ;This creates the next folder down for the band combinations
cd, 'b_g', CURRENT = old_dir
help, old_dir
outdir = old_dir + '\b_g\'

cd, dir    ;Go back to the main directory where all the datafiles are, etc.

;DEFINE OUTPUT FILES
;Use input filename to create output filename
file19 = files(file_number)   ;String containing name of the current file (file19 = current file)
shortfilename = strmid(file19, 0, 4)

band_ratio_vs_true_depth = shortfilename + '_band_ratio_vs_true_depth.tif'
regression_file = shortfilename + '_regression.tif'
final_depth_file = shortfilename + '_final_depth.tif'
der_vs_true_scatter_plot_file = shortfilename + '_der_vs_true_scatter_plot.tif'

;*****************************************************
;OPEN LAND MASK
  mask = bytarr(samples, lines)
  openr, 1, fmask
  forrd, 1, mask
```

```
  close, 1

  land_mask = mask
  mask = reform(mask, samples, lines)
  mask = rebin(mask, samples, lines, bands)

  data1 = fltarr(samples, lines, bands)
  openr, 1, file19
  forrd, 1, data1
  close, 1

;DISPLAY LAND-MASKED IMAGE
  window, 1, xsize = samples, ysize = lines, title = '(1) Water Only (land masked) - '+file19
  data1 = data1 * mask
  tvscl, data1(*,*,[4,2,1]), true = 3, order = 1

;MASK ADDITIONAL PROBLEM PIXELS (GLINT, CLOUDS, ETC.)
;User defines water region
  window, 2, title = '(2) Scatter Plot - Blue vs. NIR-1 - ' + file19

  ti = data1(*,*,1)   ;Blue
  tj = data1(*,*,6)   ;NIR1
  order = sort(ti) & ti = ti(order) & tj = tj(order)   ;Not strictly necessary, makes oplot easier
  nele = n_elements(order) & index = 10* lindgen(nele/10)   ;Plots every 10th point

plot, ti(index), tj(index), psym = 3, title = file, xtitle = 'Blue', ytitle = 'NIR-1'

print, 'Click the upper-right-hand corner of the region that defines water -- for masking purposes'

cursor, x, y, /down, /data
delta = 0.1
xx = [ 0, x, x, 0, 0]   ;For lines that create box when clicked
yy = [ 0, 0, y , y, 0]
plots, xx, yy

glint_clouds_etc = where (data1(*,*,1) gt x or data1(*,*,6) gt y)
gce = glint_clouds_etc
ngce = where(data1(*,*,1) lt x and data1(*,*,6) lt y)   ;ngce: NOT glint, clouds, etc.
```

```
help, gce
data1= reform(data1, samples*lines, bands)
data1(gce, *) = 0
data1 = reform(data1, samples, lines, bands)

gce_mask = bytarr(samples, lines) & gce_mask(*) = 1 & gce_mask(gce) = 0
land_gce_mask = land_mask*gce_mask

window, 3, xsize = samples, ysize = lines, title = '(3) Water Only (land and clouds masked) - ' + file19
  tvscl, data1(*,*,[4,2,1]), true = 3, order = 1

;*******************************************************
;DEGLINT USING HEDLEY APPROACH (UTILIZES SLOPE)
;Shows scatter plot, best fit line, slop, and line along the length of the range
 window, 4, title = '(4) Scatter plot and fit for deglint (NIR-1 vs. Blue) - ' + file19
  ti = data1(*,*,1)    ;Blue
  tj = data1(*,*,6)    ;NIR1
  ;Check for zeroes
  zeroes = where(ti le 0)
  nz = where(ti gt 0)
  ti = ti(nz)
  tj = tj(nz)
  order = sort(ti) & ti =ti(order) & tj = tj(order)    ;Not strictly necessary, makes oplot easier
  nele = n_elements( order) & index = 10 * lindgen( nele/10)    ;Plots every 10th point
    plot, tj(index), ti(index), psym = 3, /ynozero, xrange = [0, 2.0], xtitle = 'NIR-1', ytitle = 'Blue'
    degree= 1
    coeff_b = poly_fit(tj, ti, degree, chisq=chisq1, yfit = yfitb)
  oplot, tj, yfitb
    slope_b = coeff_b(1)
  xyouts, 0.2, .2, string(slope_b), /normal
    water_ir1_min = min(tj)
    water_ir1_max = max(tj)
    xmin = min(ti)
    plots, [water_ir1_min, water_ir1_max], [xmin, xmin]
    data1(*,*,1) = data1(*,*,1) - slope_b * (data1(*,*,6) - water_ir1_min)  ;Blue and NIR-1 bands

   window, 5, title = '(5) Scatter plot and fit for deglint (NIR-1 vs. Green) - ' + file19
  ti = data1(*,*,2)    ;Green
```

```
  tj = data1(*,*,6)    ;NIR1
    ;Check for zeroes
  zeroes  = where(ti le 0)
  nz = where(ti gt 0)
  ti = ti(nz)
  tj = tj(nz)
  order = sort(ti) & ti = ti(order) & tj = tj(order)    ;Not strictly necessary, makes oplot easier
  nele = n_elements( order) & index = 10 * lindgen(nele/10)    ;Plots every 10th point
    plot, tj(index), ti(index), psym = 3, /ynozero, xrange = [0, 2.0], xtitle = 'NIR-1', ytitle = 'Green'
    degree = 1
    coeff_g = poly_fit( tj, ti, degree, chisq=chisq1, yfit = yfitg)
  oplot, tj, yfitg
    slope_g = coeff_g(1)
  xyouts, 0.2, .2, string(slope_g), /normal
    water_ir1_min = min(tj)
    water_ir1_max = max(tj)
    xmin = min(ti)
    plots, [water_ir1_min, water_ir1_max], [xmin, xmin]
    data1(*,*,2) = data1(*,*,2) - slope_g * (data1(*,*,6) - water_ir1_min)   ;Green and NIR-1 bands

;*****************************************************
;DEGLINT IMAGERY BY SUBTRACTING IR WAVELENGTH REFLECTANCE
  im1b = data1

;*****************************************************
;OBTAIN RELATIVE BATHYMETRY BY RATIO OF BANDS METHOD
;Use expression: ln(1000*b1)/ln(1000*b2), where b1 = Blue band, b2 = Green band
  index1 = where(im1b lt 1) & im1b(index1) = 1
  nfac  = 100.     ;Camacho used 1000.
  reldepth = alog(nfac*im1b(*,*,1))/alog(nfac*im1b(*,*,2))
  window, 6, xsize = samples, ysize = lines, title = '(6) Blue/Green Band Ratio - Bathymetry - ' + file19
  r1 = -1.1   ;min(truedepth)
  r2 = -1.0   ;max(truedepth)
tv, bytscl(reldepth*land_gce_mask*(-1), min=r1, max=r2), order = 1

  bar = bindgen(256)
  bar = reform(bar, 1, 256)
  bar = rebin(bar, 40, 256)
```

```
  x0 = 65   ;x0, y0: define location of color bar within the image
  y0 = 30
  x1 = x0 + 40; + 1   ;x1, y1: define location of white box drawn around color bar
  y1 = y0 + 255; + 1
  tv, bar, x0, y0

  ;Displays color bar on the image
   plot, bar, /nodata, /noerase, color = 0, xrange = [0, 1], yrange = [r1, r2] * (-1), $
    xticks = 1, yticks = 4, yminor = 1, charsize = 1.0, xstyle = 1, ystyle = 1, /device, $
    pos = [x0-1, y0-1, x1, y1], xtickname = [' ',' '], yticklen = -0.05
    xyouts, x1+25, y0+128, 'Blue/Green Band Ratio', orient = 90, size = 1.0, color = 0, /device, align =
0.5

    ;Close unnecessary windows
    wdelete, 1   ;Closes Water Only (land masked) window
   ; wdelete, 4   ;Closes NIR-1 vs. Green scatter plot
   ; wdelete, 5   ;Closes NIR-2 vs. Yellow scatter plot

;*****************************************************
;OPEN GROUNDTRUTHED WATER DEPTH IMAGE
  truedepth_file = 'KailuaRaster_DepthMeters_resize_WGS84_2mpixels_995x999.dat'

  truedepth = dblarr(samples, lines)
  openr, 1, truedepth_file
  forrd, 1, truedepth
  close, 1
  truedepth = truedepth * (-1.0)   ;Make depth values positive to match reldepth

  r1 = -18   ;min(truedepth)
  r2 = 0   ;max(truedepth)

  bad = where(truedepth gt r1 * (-1))   ;Gets rid of values deeper than -20 m (r1) -- assume these are bad
data
  nodata_mask = bytarr(samples, lines) & nodata_mask(*) = 1 & nodata_mask(bad) = 0
  land_gce_mask = land_gce_mask * nodata_mask

  ;Place all masks on truedepth
```

```
  truedepth_masked = truedepth * land_gce_mask * (-1)
  truedepth = truedepth_masked

  goto, skipgt   ;Skip ground truth image -- comment out this line if you want a window
  window, 7, xsize = samples, ysize = lines, title = '(7) True Bathymetry - ' + truedepth_file
  tv, bytscl(truedepth, min = r1, max = r2), order = 1

  bar = bindgen(256) & bar = reform(bar, 1, 256) & bar = rebin(bar, 40, 256)

  x0 = 65   ;x0, y0: define location of color bar within the image
  y0 = 30
  x1 = x0 + 40; + 1   ;x1, y1: define location of white box drawn around color bar
  y1 = y0 + 255; + 1
  tv, bar, x0, y0

  ;Displays color bar on the image
   plot, bar, /nodata, /noerase, color = 0, xrange = [0, 1], yrange = [r1, r2]*(-1), $
    xticks = 1, yticks = 3, yminor = 1, charsize = 1.0, xstyle = 1, ystyle = 1, /device, $
    pos = [x0-1, y0-1, x1, y1], xtickname = [' ',' '], yticklen = -0.05
    xyouts,  x1+25, y0+128, 'Depth (meters)', orient = 90, size = 1.0, color = 0, /device, align = 0.5

    skipgt: print, 'skipping plot'
;*******************************************************
;COMPARE RELATIVE BATHYMETRY MEASURE TO GROUND TRUTH BY TAKING RATIO OF RELATIVE DEPTH TO TRUE DEPTH
;Ignore areas where trudepth = 0 (truedepth data don't exist at those points)

  truedepth(bad) = 0
  good = where(truedepth ne 0) & help, good
  depth_ratio = fltarr(samples, lines)
  depth_ratio = reldepth/truedepth
  depth_ratio(bad) = 0

  r1 = -0.5   ;min(depth_ratio(good))
  r2 =  1.0   ;max(depth_ratio(good))

  goto, skip_rat   ;Not really useful
  window, 8, xsize = samples, ysize = lines, title = '(8) Blue/Green Band Ratio vs. True Bathymetry - ' +
file19
```

```
  im =  bytscl(-1 * depth_ratio, min = r1, max = r2)
  index = where(land_gce_mask eq 0)
  im(index) = 255
  tv, im, order = 1

  bar = bindgen(256)
  bar = reform(bar, 1, 256)
  bar = rebin(bar, 40, 256)
  x0 = 65   ;x0, y0: define location of color bar within the image
  y0 = 30
  x1 = x0 + 40; + 1   ;x1, y1: define location of white box drawn around color bar
  y1 = y0 + 255; + 1
  tv, bar, x0, y0

  ;Display color bar on the image
   plot, bar, /nodata, /noerase, color = 0, xrange = [0, 1], yrange = [r1, r2], $
    xticks = 1, yticks = 2, yminor = 1, charsize = 1.0, xstyle = 1, ystyle = 1, /device, $
    pos = [x0-1, y0-1, x1, y1], xtickname = [' ',' '], yticklen = -0.05
    xyouts,  x1+25, y0+128, ' B/G Band Ratio vs. Depth (m)', orient = 90, size = 1.0, color = 0, /device,
align = 0.5

  im = tvrd(true = 1)
  im = reverse(im,1)
  im = reverse(im,3)
  im = reverse(im,1)
  write_tiff, outdir + band_ratio_vs_true_depth, im

skip_rat: print, 'Skipping ratio'

;*****************************************************
;REGRESS RELDEPTH VS TRUEDEPTH TO FIND ABSOLUTE (DERIVED) DEPTH VALUE

  x = reldepth(good)
  y = truedepth(good)
  result = regress(x, y, SIGMA = sigma1, CONST = const, CHISQ = chisq, yfit = yfit, corr = corr)
  print, 'Equation of regression line (reldepth vs. truedepth): '
  print, 'Regress Result: ' + string(result) + 'Regress Constant: ' + string(const)
  print, 'Chi-squared: ', chisq, ' Correlation: ', corr
```

```
  print, 'Valid regression?'

  degree = 1
  Result2 = POLY_FIT(x, y, degree, CHISQ = chisq2, SIGMA = polysig, YFIT = yfit2 )
  print, 'Equation of regression line (reldepth vs. truedepth): '
  print, 'Polyfit result: ' + string(result2)
  print, 'Chi-squared: ', chisq2
  print, 'Valid regression?'
  help, polysig, yfit, yfit2

  ;Uncomment to see the scatter plot and best-fit regression line - works, just slowly.
  window, 9, xsize = 900, ysize = 900, title = '(9) Blue/Green Band Ratio vs. True Depth - ' + file19
  x = reldepth(good)
  y = truedepth(good)

  good2 = where(y gt -12)
  xx = x(good2)
  yy = y(good2)

  nele = n_elements(xx)
  index = indgen(nele/10, /long)

  plot, xx(index), yy(index), psym = 3, xtitle = 'Blue/Green Band Ratio', ytitle='True Depth (m)', title =
file, $
   yrange = [-15, 0], xrange = [1.0, 1.2], ymargin = [5, 4]
  oplot, x(index), yfit(index)

  slope = result2(1)
  intercept = result2(0)
  xyouts, 1.02, -0.5, 'Chi-squared: ' + string(chisq)
  xyouts, 1.02, -1.0, 'Correlation: ' + string(corr, format = "(f8.3)")
  xyouts, 1.02, -1.5, 'Slope: ' + string(slope, format = "(f8.1)")
  xyouts, 1.02, -2.0, 'Intercept: ' + string(intercept, format = "(f8.1)")

im = tvrd()
im = 255b - im
tv, im
```

```
  im = tvrd(true = 1)
  im = reverse(im,1)
  im = reverse(im,3)
  im = reverse(im,1)
  write_tiff, outdir + regression_file, im

;*******************************************************
;USE REGRESSION RESULTS TO CORRECT RELDEPTH AND CREATE DERIVED DEPTH
  absdepth = reldepth * result(0) + const
  r1 = -18.0   ;0.0
  r2 = 0.0  ;(-1.0)*min(absdepth);0.0 ;2.0
  window, 10, xsize = samples, ysize = lines, title = '(10) Derived Bathymetry - ' + file19   ;ABSOLUTE IS
THE INCORRECT TERM -- DERIVED IS CORRECT

  im = bytscl(absdepth, min = r1, max = r2)
  index = where(land_gce_mask eq 0)
  im(index) = 255

  tv, im, order = 1
  bar = bindgen(256)
  bar = reform(bar, 1, 256)
  bar = rebin(bar, 40, 256)
  x0 = 65 + 50   ;x0, y0: define location of color bar within the image
  y0 = 30
  x1 = x0 + 40   ;+ 1   ;x1, y1: define location of white box drawn around color bar
  y1 = y0 + 255   ;6; + 1
  tv, bar, x0, y0

  ;Display color bar on the image
   plot, bar, /nodata, /noerase, color = 0, xrange = [0, 1], yrange = [r1, r2], $
    xticks = 1, yticks = 3, yminor = 1, charsize = 1.0, xstyle = 1, ystyle = 1, /device, $
    pos = [x0-1, y0-1, x1, y1], xtickname = [' ',' '], yticklen = -0.05, $
    ytitle = 'Blue/Green'
    xyouts,  x1+25, y0+128, 'Derived Depth (meters)', orient = 90, size = 1.0, color = 0, /device, align =
0.5

  im = tvrd(true = 1)
  im = reverse(im,1)
```

```
  im = reverse(im,3)
  im = reverse(im,1)
  write_tiff, outdir + final_depth_file, im
;*****************************************************

  x = absdepth(good)
  y = truedepth(good)
  result = regress(x, y, SIGMA = sigma1, CONST = const, CHISQ = chisq, yfit = yfit, corr = corr)
  print, 'Equation of regression line (absdepth vs. truedepth): '
  print, 'Regress Result: ' + string(result) + 'Regress Constant: ' + string(const)
  print, 'Chi-squared: ', chisq, 'Correlation: ', corr
  print, 'Valid regression?'

  degree = 1
  Result2 = POLY_FIT( x, y, degree, CHISQ = chisq2,  SIGMA = polysig , YFIT = yfit2)
  print, 'Equation of regression line (absdepth vs. truedepth): '
  print, 'Polyfit result: ' + string(result2)
  print, 'Chi-squared: ', chisq2
  print, 'Valid regression?'
   help, polysig, yfit, yfit2

  ;Uncomment to see the scatter plot and best-fit regression line - works, just slowly.
  window, 11, xsize = 900, ysize = 900, title = '(11) Derived Bathymetry vs. True Bathymetry'
  x = absdepth(good)
  y = truedepth(good)
  nele = n_elements(x)
  index = indgen(nele/10, /long)

  plot, x(index), y(index), psym = 3, xtitle = 'Derived Bathymetry (m)', ytitle='True Depth (m)', title =
file, $
   yrange = [-15, 0], xrange =[-15, 0], ymargin = [5, 4]
  oplot, x(index), yfit(index)

  slope = result2(1)
  intercept = result2(0)
  xyouts, -14, -1.0, 'Chi-squared: ' + string(chisq)
  xyouts, -14, -2, 'Correlation: ' + string(corr, format = "(f8.3)")
```

```
im = tvrd()
im = 255b - im
tv, im

  im = tvrd(true = 1)
  im = reverse(im,1)
  im = reverse(im,3)
  im = reverse(im,1)
  write_tiff, outdir + der_vs_true_scatter_plot_file, im

stop
endfor

end
```

D. DERIVED DEPTH VS. TRUE DEPTH PLOTS AND LINES OF BEST FIT

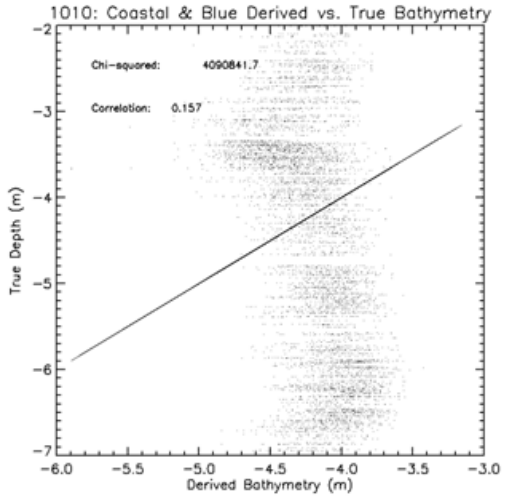

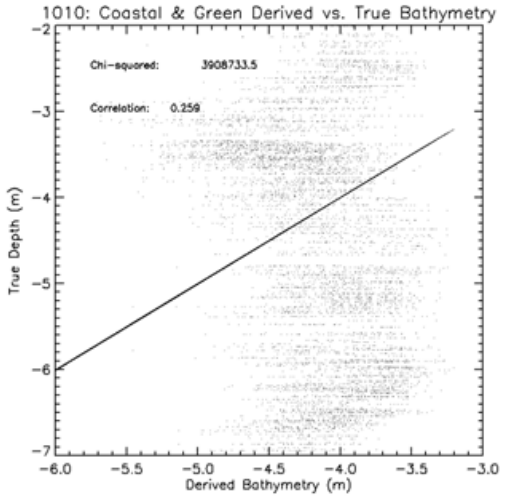

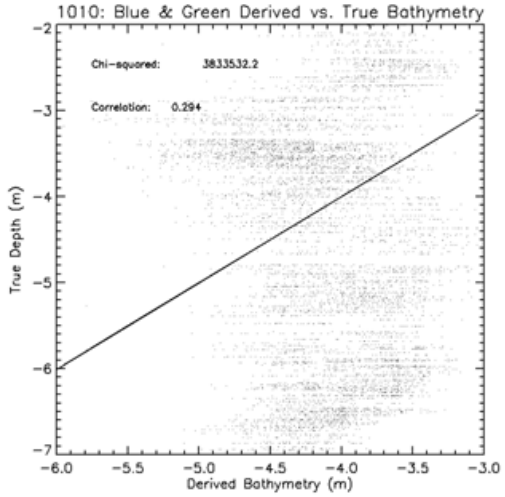

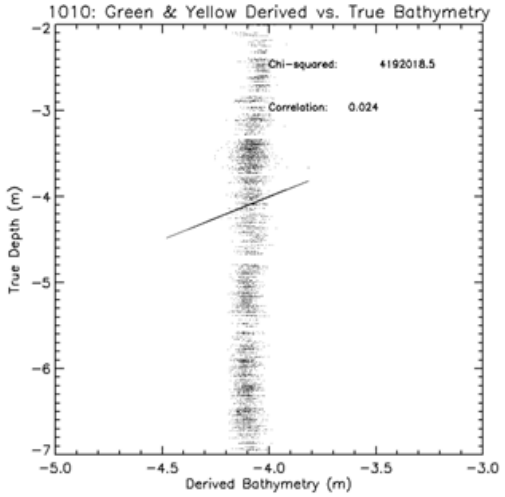

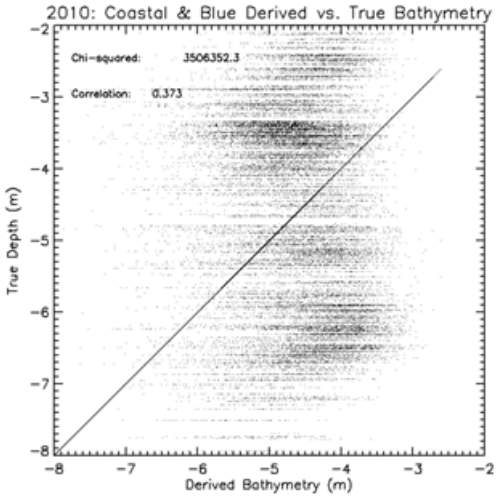
2010: Coastal & Blue Derived vs. True Bathymetry
Chi-squared: 3506352.3
Correlation: 0.373
True Depth (m)
Derived Bathymetry (m)

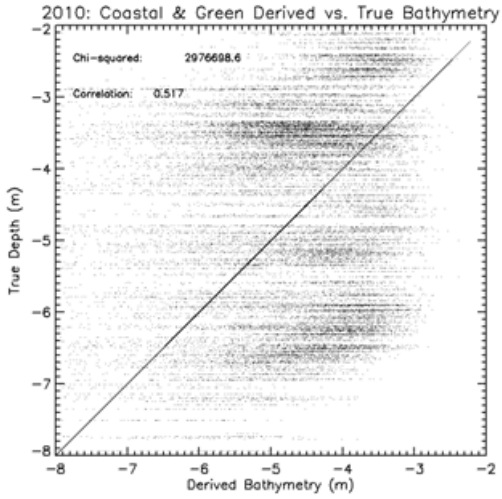
2010: Coastal & Green Derived vs. True Bathymetry
Chi-squared: 2976698.6
Correlation: 0.517
True Depth (m)
Derived Bathymetry (m)

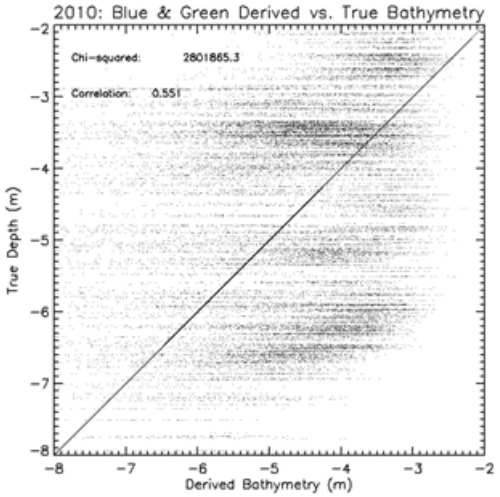
2010: Blue & Green Derived vs. True Bathymetry
Chi-squared: 2801865.3
Correlation: 0.551
True Depth (m)
Derived Bathymetry (m)

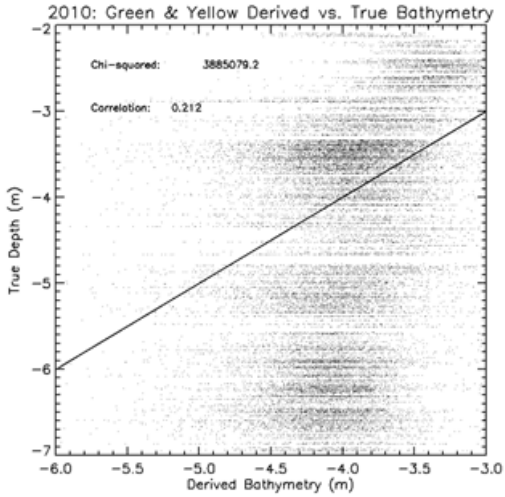
2010: Green & Yellow Derived vs. True Bathymetry
Chi-squared: 3885079.2
Correlation: 0.212
True Depth (m)
Derived Bathymetry (m)

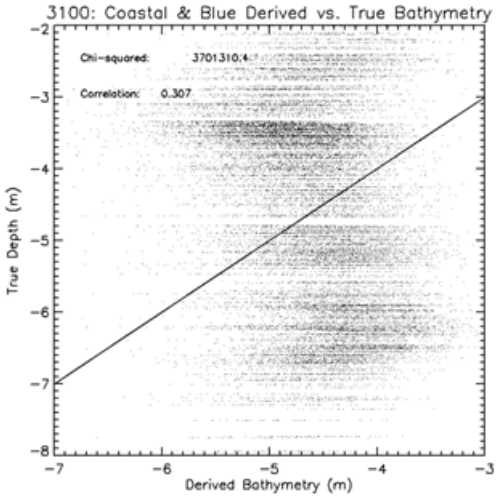
3100: Coastal & Blue Derived vs. True Bathymetry
Chi-squared: 3701310.4
Correlation: 0.307
True Depth (m)
Derived Bathymetry (m)

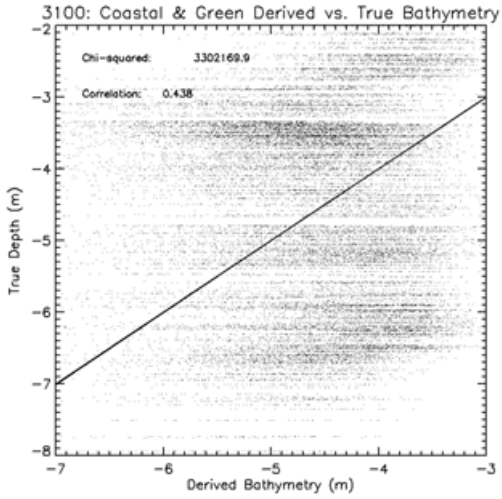
3100: Coastal & Green Derived vs. True Bathymetry
Chi-squared: 3302169.9
Correlation: 0.438
True Depth (m)
Derived Bathymetry (m)

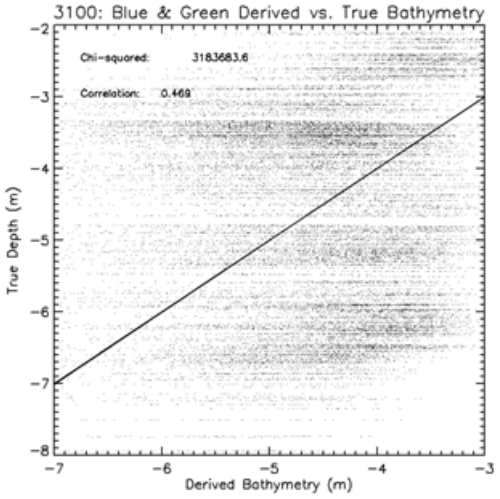
3100: Blue & Green Derived vs. True Bathymetry
Chi-squared: 3183683.6
Correlation: 0.469
True Depth (m)
Derived Bathymetry (m)

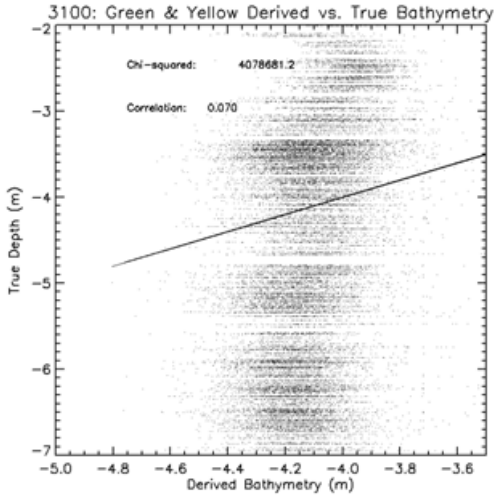
3100: Green & Yellow Derived vs. True Bathymetry
Chi-squared: 4078681.2
Correlation: 0.070
True Depth (m)
Derived Bathymetry (m)

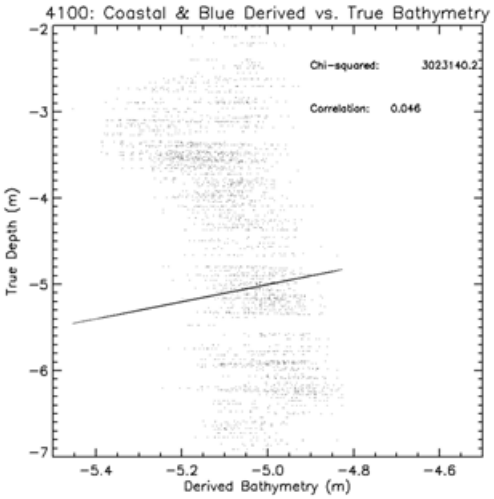
4100: Coastal & Blue Derived vs. True Bathymetry
Chi-squared: 3023140.2
Correlation: 0.046
True Depth (m)
Derived Bathymetry (m)

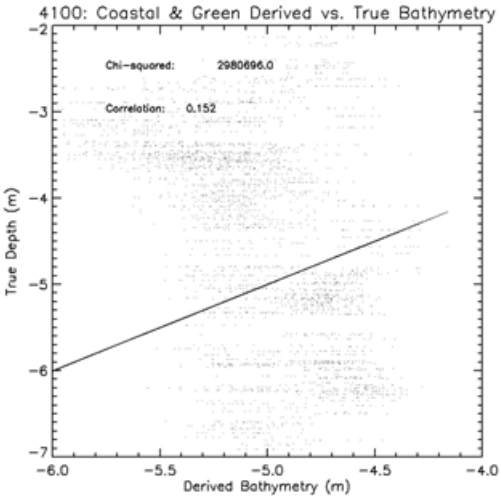
4100: Coastal & Green Derived vs. True Bathymetry
Chi-squared: 2980696.0
Correlation: 0.152
True Depth (m)
Derived Bathymetry (m)

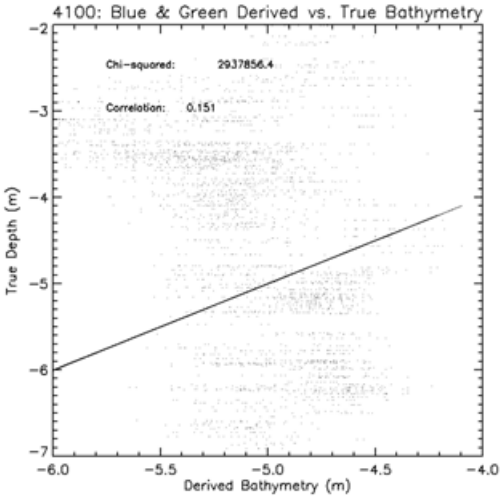
4100: Blue & Green Derived vs. True Bathymetry
Chi-squared: 2937856.4
Correlation: 0.151
True Depth (m)
Derived Bathymetry (m)

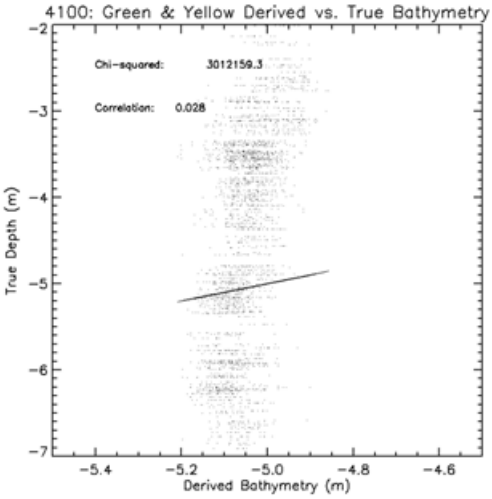
4100: Green & Yellow Derived vs. True Bathymetry
Chi-squared: 3012159.3
Correlation: 0.028
True Depth (m)
Derived Bathymetry (m)

E. TABLES OF EXAMPLE CHI-SQUARED AND CORRELATION VALUES FOR EACH BAND COMBINATION

1. Coastal & Blue (with best fits highlighted)

IMAGE ID	meanSatEl	Chi-Squared	Correlation
1010	24.9	4092798.6	0.163
1020	26.5	4081785.6	0.169
1030	28.1	4059720.3	0.173
1040	29.8	4043658.7	0.19
1050	31.7	3975405.5	0.212
1060	33.7	3878340.7	0.254
1080	38.2	3874253.7	0.273
1090	40.8	3740692.8	0.319
1100	43.7	3598962.8	0.337
2010	46.7	3520323.3	0.372
2020	50.1	3353757.3	0.433
2030	53.6	3377771.5	0.425
2040	57.6	3248184.9	0.462
2050	61.6	3216444	0.472
2060	66.0	3170698.1	0.475
2070	70.2	3187990.2	0.48
2080	74.0	3097967.8	0.467
2090	76.9	3107493.1	0.483
2100	77.8	3082345.9	0.488
3010	76.3	3105183.7	0.489
3020	73.1	3096221.6	0.496
3030	69.0	3119432.1	0.493
3040	64.8	3179182.1	0.483
3050	60.6	3215832.1	0.475
3060	56.6	3334628	0.445
3070	52.9	3375361	0.434
3080	49.6	3523816.2	0.385
3090	46.5	3585509.4	0.359
3100	43.7	3700396.6	0.311
4010	41.1	3768118.2	0.28
4020	38.7	3858040.5	0.233
4030	36.5	3893903	0.212
4040	34.4	3917829.2	0.16
4050	32.5	3875953.7	0.139

4060	30.7	3757712.1	0.127
4070	29.0	3647051.5	0.133
4080	27.4	3520708.9	0.113
4090	25.9	3355284.3	0.093
4100	24.5	3020893	0.038

2. Coastal & Green (with best fits highlighted)

IMAGE ID	meanSatEl	Chi-Squared	Correlation
1010	24.9	3911460	0.262
1020	26.5	3888263.3	0.271
1030	28.1	3882215.3	0.277
1040	29.8	3847912.4	0.288
1050	31.7	3755520.8	0.313
1060	33.7	3628560.2	0.354
1080	38.2	3546724.9	0.39
1090	40.8	3317653.4	0.452
1100	43.7	3132645.7	0.475
2010	46.7	3004689.7	0.516
2020	50.1	2762942.9	0.573
2030	53.6	2698408.7	0.591
2040	57.6	2585662.4	0.611
2050	61.6	2493514.7	0.632
2060	66.0	2406520.2	0.644
2070	70.2	2380175.1	0.65
2080	74.0	2331197.5	0.651
2090	76.9	2262424.3	0.66
2100	77.8	2242532.2	0.665
3010	76.3	2294378.5	0.665
3020	73.1	2291861.7	0.663
3030	69.0	2360830.5	0.653
3040	64.8	2429096	0.636
3050	60.6	2569034.7	0.615
3060	56.6	2718923.5	0.588
3070	52.9	2771285.8	0.577
3080	49.6	3030260.5	0.519
3090	46.5	3148438	0.487
3100	43.7	3326883.7	0.434
4010	41.1	3239760.9	0.455

4020	38.7	3554008.1	0.357
4030	36.5	3580085.4	0.345
4040	34.4	3690842.1	0.284
4050	32.5	3740913	0.23
4060	30.7	3641605.2	0.213
4070	29.0	3543715.8	0.212
4080	27.4	3412602.3	0.203
4090	25.9	3204708.3	0.143
4100	24.5	2973309	0.115

3. Blue & Green (with best fits highlighted)

IMAGE ID	meanSatEl	Chi-Squared	Correlation
1010	24.9	3837181.9	0.294
1020	26.5	3799491.4	0.31
1030	28.1	3826809.8	0.295
1040	29.8	3788817	0.312
1050	31.7	3674079.4	0.34
1060	33.7	3539442.7	0.386
1080	38.2	3449363.9	0.419
1090	40.8	3170962	0.485
1100	43.7	3013485.2	0.512
2010	46.7	2834575.7	0.552
2020	50.1	2629851	0.601
2030	53.6	2483369.3	0.632
2040	57.6	2372775.6	0.652
2050	61.6	2245770.1	0.675
2060	66.0	2157476.7	0.689
2070	70.2	2122878.3	0.696
2080	74.0	2099771.8	0.698
2090	76.9	2047377.9	0.705
2100	77.8	2019917.5	0.707
3010	76.3	2040766.2	0.706
3020	73.1	2064788.8	0.703
3030	69.0	2128616.8	0.695
3040	64.8	2209021	0.682
3050	60.6	2394974.9	0.65
3060	56.6	2537364.6	0.626
3070	52.9	2676606.9	0.597

3080	49.6	2883049.7	0.551
3090	46.5	2994151.5	0.521
3100	43.7	3242079.3	0.458
4010	41.1	3074725.8	0.499
4020	38.7	3446563.2	0.393
4030	36.5	3455884.2	0.391
4040	34.4	3618164.1	0.315
4050	32.5	3676137.1	0.268
4060	30.7	3603561.2	0.241
4070	29.0	3515796.4	0.23
4080	27.4	3360508.4	0.24
4090	25.9	3203685.6	0.232
4100	24.5	2942699.1	0.198

4. Green & Yellow (with best fits highlighted)

IMAGE ID	meanSatEl	Chi-Squared	Correlation
1010	24.9	4204121.8	0.022
1020	26.5	4199128.1	0.056
1030	28.1	4193524.9	0.021
1040	29.8	4195615.6	0.008
1050	31.7	4137792	0.073
1060	33.7	4088413.4	0.121
1080	38.2	4154217.8	0.085
1090	40.8	4059838.4	0.161
1100	43.7	4029843	0.107
2010	46.7	3892704	0.212
2020	50.1	3869278.8	0.242
2030	53.6	3803366.4	0.278
2040	57.6	3726302.1	0.31
2050	61.6	3732941.5	0.309
2060	66.0	3647327.9	0.337
2070	70.2	3558505.7	0.374
2080	74.0	3538108.6	0.361
2090	76.9	3526190.9	0.36
2100	77.8	3496716.8	0.362
3010	76.3	3537665.1	0.371
3020	73.1	3527937.5	0.368
3030	69.0	3792433.1	0.267

3040	64.8	3710290.4	0.322
3050	60.6	4123412.3	0.082
3060	56.6	3981819.9	0.21
3070	52.9	3747042.4	0.314
3080	49.6	4140895	0.012
3090	46.5	4033670.6	0.151
3100	43.7	4077367.7	0.07
4010	41.1	3828814.7	0.252
4020	38.7	4043303	0.095
4030	36.5	4030102.2	0.105
4040	34.4	3891947.4	0.18
4050	32.5	3954476.1	0.035
4060	30.7	3821397.1	0.045
4070	29.0	3701158.5	0.079
4080	27.4	3565573	0.068
4090	25.9	3328975.3	0.074
4100	24.5	3061447.5	0.064

THIS PAGE INTENTIONALLY LEFT BLANK

INITIAL DISTRIBUTION LIST

1. Defense Technical Information Center
   Ft. Belvoir, Virginia

2. Dudley Knox Library
   Naval Postgraduate School
   Monterey, California

3. Dr. Richard C. Olsen
   Naval Postgraduate School, Remote Sensing Center
   Monterey, California

4. Dr. Fred A. Kruse
   Naval Postgraduate School, Remote Sensing Center
   Monterey, California

5. Dr. Dan C. Boger
   Naval Postgraduate School, Remote Sensing Center
   Monterey, California